RSC Advances

REVIEW

View Article Online
View Journal | View Issue

Open Access Article. Published on 02 September 2025. Downloaded on 11/10/2025 5:56:01 AM.
This article is licensed under a Creative Commons Attribution-NonCommercial 3.0 Unported Licence.

Check for updates

Cite this: *RSC Adv.*, 2025, **15**, 31313

Advanced photocatalytic degradation of POPs and other contaminants: a comprehensive review on nanocomposites and heterojunctions

Ruhit Kumar Paul and Md. Ahmaruzzaman *

Received 18th June 2025
Accepted 18th August 2025

DOI: 10.1039/d5ra04336k

rsc.li/rsc-advances

The environmental persistence and toxicity of pollutants such as persistent organic pollutants (POPs), synthetic dyes, and pharmaceutical residues necessitate the development of effective and sustainable remediation strategies. This review underscores the urgent need for advanced approaches to eliminate these contaminants, with a particular focus on metal oxide-based photocatalysts, such as TiO_2, ZnO, WO_3, CuO, and others. We have explored their photocatalytic mechanisms, inherent limitations, and recent advancements, such as elemental doping and heterojunction engineering, to enhance their activity under visible light. Nanocomposite systems, especially those incorporating heterojunctions, have demonstrated significant improvements in photocatalytic efficiency by facilitating charge separation and

Department of Chemistry, National Institute of Technology Silchar, Assam, 788010, India. E-mail: mda2002@gmail.com

Ruhit Kumar Paul

Ruhit Kumar Paul is a research scholar currently pursuing his PhD in Material Science at the National Institute of Technology (NIT) Silchar, Assam, India, under the guidance of Prof. Md. Ahmaruzzaman. He is in the third semester of his PhD program, focusing on the synthesis and application of semiconductor-based nanomaterials for environmental and energy-related challenges. He completed his MSc in Chemistry from Assam University in 2022 and earned his undergraduate degree in 2020 from the same university.

Md. Ahmaruzzaman

Md. Ahmaruzzaman is a distinguished full-time professor in the Department of Chemistry at National Institute of Technology (NIT), Silchar, India. He earned his MSc in Chemistry from North Bengal University, where he also completed his undergraduate studies. Additionally, he pursued a postgraduate MTech in Energy Science and Technology at Jadavpur University and later obtained his PhD from the Indian Institute of Technology (IIT) Delhi. His area of research is nanoscience and technology, energy and environment, electrochemistry, metal–organic frameworks, and development of low-cost adsorbents for water treatment, etc. With extensive experience in academic research, he has supervised numerous postgraduate projects and has an impressive publication record, contributing over 350 research articles to esteemed international journals and conferences. His scholarly work has garnered over 18 300+ citations in reputed international journals. Prof. Ahmaruzzaman serves as a reviewer for several high-impact peer-reviewed journals and holds editorial positions in multiple esteemed publications. He is the Associate Editor of the International Journal of Environmental Analytical Chemistry, Section Editor of Current Materials Science, and Editorial Board Member of Scientific Reports and Discover Materials.

© 2025 The Author(s). Published by the Royal Society of Chemistry

Open Access Article. Published on 02 September 2025. Downloaded on 11/10/2025 5:56:01 AM.
This article is licensed under a Creative Commons Attribution-NonCommercial 3.0 Unported Licence.

promoting the generation of reactive species. This review provides an in-depth examination of the mechanisms and practical applications of these materials in the degradation of POPs, dyes, and pharmaceutical pollutants. Furthermore, it outlines current challenges and identifies promising directions for future research aimed at developing high-performance photocatalysts for environmental remediation.

1. Introduction

In the present day, the Earth's ecosystem is experiencing ongoing contamination from various pollutants, which vary in type and location. Certain pollutants persist in the environment that are resistant to degradation (chemical, biological, and photolytic reactions) and remain in the environment for extended periods.[1–4]

These pollutants are organic compounds of natural or anthropogenic origin are called persistent organic pollutants (POPs). POPs pose a significant global concern due to their persistence, ability to travel long distances, and tendency to bioaccumulate in fat-rich tissues such as adipose tissue, liver, brain, and breast tissue.[5–7] Even at low concentrations, they exhibit high toxicity. Once inside the body, POPs are transported *via* the lymphatic system and bloodstream, primarily accumulating in adipocyte lipid droplets within adipose tissue. The liver also serves as a major storage site, especially for compounds like dioxins, particularly at higher exposure levels.[8] Various POPs, particularly organochlorine insecticides, polychlorinated biphenyls (PCBs), polychlorinated dibenzodioxins (PCDDs), polychlorinated dibenzofurans (PCDFs), and polybrominated diphenyl ethers (PBDEs), among others, primarily originate from human activities and have been extensively employed in a variety of products.[9] For instance, organochlorine pesticides have been widely used in agriculture to manage diverse plant pests such as insects, mites, nematodes, fungi, and bacteria. In addition to their agricultural application, these compounds have played a significant role in public health initiatives targeting disease vectors like mosquitoes, which transmit pathogens including bacteria, viruses, and parasites. Furthermore, certain organochlorines have also been incorporated into household disinfectants.[10] PBDEs, on the other hand, have been broadly utilized as flame retardants in numerous consumer products, including polyurethane foams used in furniture, mattresses, carpet underlays, and automobile seats, as well as in styrene-based plastics found in electronic devices like televisions and computers, and in flame-retardant textiles.[11]

The concern about POPs arises from their ability to bioaccumulate and magnify within the food chain, particularly affecting top predator species, including humans. The most extensively documented and evident effects have been observed in birds and marine mammals. Numerous studies have reviewed how organochlorines (OCs), particularly DDE-a metabolic byproduct of DDT can impact eggshell thickness in birds of prey.[12–14] For instance, Haegele and Hudson[15] reported that exposure to 40 ppm of *p,p′*-DDE for 96 days caused significant eggshell thinning in mallard hens (*Anas platyrhynchos*) by 15–20% during and shortly after treatment, and by 7.4% even 11 months later, demonstrating its long lasting impact.[15]

POPs harm living organisms and human health, notably by disrupting immune system function and decreasing the body's ability to resist viruses.[16,17] In the current era of environmental pollution, POPs are widespread in almost every individual. Exposure to these pollutants poses significant health risks, including hormone disruption, cancer, cardiovascular diseases, obesity, reproductive and neurological disorders, learning disabilities, and diabetes. Moreover, these pollutants can also induce defects in female embryos.[1] Persistent organic pollutants are also known for their semi-volatile nature, allowing them to exist in either vapor or adsorbed forms on atmospheric particles, facilitating long-distance transport through the atmosphere. This unique persistence, coupled with characteristics like semi-volatility, has led to the global distribution of compounds such as PCBs, even in regions where they have never been utilized.[18]

Water, on the other hand, is thought to be the most essential natural resource for life and is, therefore, the most vital of all. Almost 80% of the world's population currently faces issues with water supply and security as a result of fast industrialization, urbanization, and a lack of awareness among people that water is a vital resource.[19] Additionally, drinking water resources are getting increasingly polluted as a result of human and industrial/governmental ignorance, and freshwater resources are thus becoming increasingly inaccessible.[20] Consequently, there has been a significant increase in the focus on water contamination as a matter of concern in recent times. The majority of aqueous contamination is caused by waste water tainted with dyes. Dye-contaminated wastewater is the result of various industries releasing their dye-contaminated effluents into the environment, including textile dyeing, paper manufacturing, food processing, paints, and cosmetics.[21,22] Discharged dyes pose serious health risks to aquatic life, including carcinogenesis and xenobiotoxicity. The presence of dyes in wastewater has a negative impact on aquatic ecosystems because the dyes make water appear very colored, which blocks sunlight from reaching the water's core.[23,24] Pharmaceutical residues are another cause of water contamination. Almost all aquatic matrices on every continent have shown evidence of pharmaceutical residues in recent decades.[25]

Therefore, removing POPs and other pollutants, such as dyes and pharmaceutical residues, are crucial because of their toxicity and harmful effects on human health and the environment. By removing these pollutants, we can mitigate these risks and safeguard the health of both present and future generations.

At present, a range of techniques, including physical, chemical, biological, or hybrid methods, are proposed for the decomposition and mineralization of the aforementioned pollutants. The conventional methods used for the removal of such contaminants are surface adsorption,[26,27] biological

 © 2025 The Author(s). Published by the Royal Society of Chemistry

Open Access Article. Published on 02 September 2025. Downloaded on 11/10/2025 5:56:01 AM.
This article is licensed under a Creative Commons Attribution-NonCommercial 3.0 Unported Licence.

degradation,[28] and membrane filtration.[29] Alternative technologies such as adsorption and coagulation merely concentrate pollutants by transferring them between phases without achieving complete "elimination" or "degradation" of the contaminants.[30] For example, adsorption employing activated carbon, resins, carbon nanotubes, or similar materials enriches and separates pollutants from water or gas phases without degrading them. However, if the desorbed contaminants from the saturated adsorbent are not effectively treated, there is a significant risk of secondary pollution.[16,31] In another approach, chemical oxidation and biotechnology techniques also face many disadvantages, including high costs with large chemical consumption, incomplete destruction, and prolonged overall treatment time.[32] Among all the approaches, photocatalysis is promising and essential because of its high efficiency, energy-saving properties, mild reaction conditions, and minimal secondary pollution. This has led to a growing interest from scientific researchers.[33–36] This review offers a comprehensive and integrated analysis of the photocatalytic degradation of the POPs, dyes, and pharmaceutical pollutants-three major organic pollutants, bringing together these diverse pollutants within a unified framework. While many existing reviews tends to focus on a single class of pollutants, this work covers a broader approach. The study includes degradation mechanisms, photocatalyst's performance data along with their performance enhancement strategies across different classes of pollutant. Special focus is given to advanced strategies such as doping, heterojunction formation, and Z-scheme systems to highlight how these can address present limitations. Overall, this review not only highlights recent progress but also point out gaps in current research and suggests practical directions for future work aimed at more effective remediation of pollutants.

2. Types of POPs and other pollutants

2.1. Types of POPs

Since the 1970s, the use of POPs has been restricted, and the release of these compounds has been prohibited in Europe and the USA. During the Stockholm Convention in 2001, delegates from 92 nations agreed to ratify the treaty to reduce or eliminate the release of the "dirty dozen" – the original 12 POP substances. These include aldrin, chlordane, dichlorodiphenyl trichloroethane (DDT), dieldrin, endrin, heptachlor, hexachlorobenzene, mirex, toxaphene, polychlorinated biphenyls (PCBs), polychlorinated dibenzo-*p*-dioxins, polychlorinated dibenzofurans.[37] Although additional contaminants have been identified, the primary focus remains on these original 12, which include 10 intentionally produced chemicals such as aldrin, DDT, and PCBs, as well as two unintentionally produced substances, PCDDs and PCDFs.[38,39] Polycyclic aromatic hydrocarbons (PAHs), formed unintentionally through the combustion and burning of organic compounds, are classified as persistent organic pollutants. Their prevalence is particularly pronounced in densely industrialized regions, with river sediment contamination being a significant concern. Fig. 1 shows different classes and examples of POPs.[40]

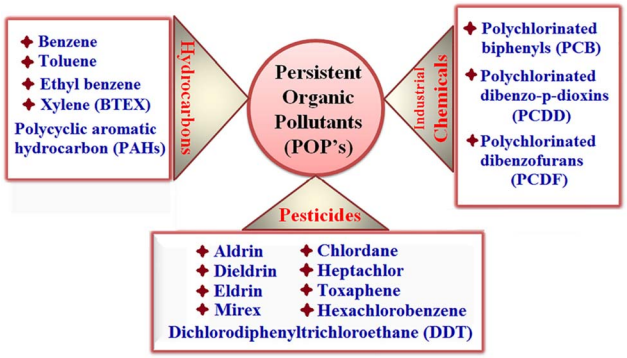

Fig. 1 Classification of POPs.[40] "Reproduced from ref. 40 with permission from [Elsevier], copyright [2022]."

2.1.1. Intentional POPs. Different chemical reactions involving chlorine will generate these compounds as desired products. They belong to the class of organic molecules linked with chlorine atoms, exhibiting high lipophilicity and often high neurotoxicity, and are known as organochlorine compounds (OCs). Examples include chlorinated insecticides like dichlorodiphenyltrichloroethane (DDT) and PCBs. These compounds can be categorized into industrial chemicals and organochlorine pesticides.[38,41,42]

2.1.1.1. Organochlorine pesticides (OCPs). One significant class of POPs posing significant risks to plants, animals, and humans is Organochlorine Pesticides (OCPs), characterized by many chlorine atoms. These highly stable chemicals can persist in various environmental compartments for years, leading to ongoing contamination and hazards.[43] However, applications of these compounds have been restricted in many countries since 1970, but residues of OCP are still found in agricultural fields,[44] food products,[45] water surfaces, and sediments.[46] Mirex, hexachlorocyclohexanes (HCHs), heptachlor, endosulfan, DDT, endrin, dieldrin, and aldrin are among the various examples of OCPs.

2.1.1.2. Industrial chemicals. Some perfluorooctanoic acid and its derivatives, PCBs, polychlorinated naphthalenes, short-chain chlorinated paraffins, and perfluorooctane sulfonic acid and its derivatives are among the substances in this group. POPs in this category are widely utilized in industrial production processes. For instance, PCBs were chemicals in industrial lubricants and coolants for manufacturing transformers, capacitors, and other electrical goods.[9] Perfluorooctanoic acid has been used to produce numerous consumer goods known for their resistance to heat, grease, oil, stains, and water. The discharge of these POPs has been identified as environmental contamination in water, soil, and air, as documented in numerous previous studies.[47,48]

2.1.2. Unintentional POPs. These chemicals were generated as undesired by-products of combustion or chemical processes involving chlorine compounds. This group includes well-known compounds such as PCBs, PCDDs, and PCDFs. Other designated compounds in this group include HCB, hexachlorobutadiene, pentachlorobenzene, and polychlorinated naphthalene.[9] These substances are often classified

Open Access Article. Published on 02 September 2025. Downloaded on 11/10/2025 5:56:01 AM.
This article is licensed under a Creative Commons Attribution-NonCommercial 3.0 Unported Licence.

Table 1 Occurrence of PAHs

PAH	Occurrence	Ref.
Benzo[*a*]pyrene	It has been reportedly found in the air, surface water, soil, and sediments. It is present in cigarette smoke as well as in food products, especially when smoked and grilled	52
Benzo[*a*]anthracene	It is more likely to be found mixed with other PAHs in coal tar, bitumen and asphalt. It is primarily found in gasoline and diesel exhaust, tobacco and cigeratte smoke	53
Benzo[*b*] fluoranthene	Benzo(*b*)fluoranthene is present as a component of polycyclic aromatic hydrocarbons (PAH) content in the environment usually resulting from the incomplete combustion or pyrolysis of organic matters, especially fossil fuels and tobacco	54
Indeno[1,2,3-*cd*] pyrene	Typical products of motor vehicle exhausts	55
Benzo[*ghi*]perylene	Typical products of motor vehicle exhausts, street dust	
Phenanthrene	Diesel exhausts, street dust	
Chrysene	Diesel exhausts, coal combustion	
Naphthalene	Gasoline combustion, vascular land plants or termite activity	
Dibenzothiophenes	Abundant in coal emission condensates and industrial coal emissions	
Benzo[*e*]pyrene	Commercial waxes, petrolatum, creosote, coal tar, crude oil from S. Louisiana, Kuwait, and Qatar	56

into polycyclic aromatic hydrocarbons (PAHs), dioxin, and furan compounds.[38]

2.1.2.1. Polycyclic aromatic hydrocarbons (PAHs). PAHs, characterized by two or more fused benzene rings arranged linearly, angularly, or in clusters, are composed solely of carbon and hydrogen atoms, with a stable central molecular structure bound by carbon–carbon bonds.[38] PAHs, acknowledged as potent carcinogens or mutagens, are designated priority pollutants by the United States Environmental Protection Agency (USEPA) and the European Commission (EC). They enter aquatic and terrestrial systems through a combination of natural phenomena such as forest fires and volcanic eruptions, as well as anthropogenic sources, including incomplete combustion of fuels, cigarette smoke, vehicular traffic emissions, industrial wastewater releases, oil spillage, and tyre wear and abrasion.[49,50] Table 1 shows the occurrence of various types of PAHs. Fig. 2 represents the structure of some PAHs recognized by European Commission.[51]

2.1.2.2. Dioxins and dibenzofurans. For decades, chlorinated dibenzo-*p*-dioxins (dioxins) have raised concerns due to their toxic properties, detailed below. Similarly structured, chlorinated dibenzofurans (furans) exhibit comparable chemical properties and harmful consequences, often analyzed alongside dioxins. Recently, attention has turned to a particular subgroup of PCBs known as dioxin-like PCBs (DLPCBs). It's widely acknowledged that human activities and man-made sources significantly outweigh natural processes in contributing to the environmental presence of PCDDs and PCDFs, particularly since the 1930s, coinciding with the widespread production and usage of chlorinated chemicals.[38,57,58] Human-made sources of PCDDs and PCDFs can be categorized into three primary groups: chemical processes, combustion processes, and secondary sources. The primary sources of PCDDs and PCDFs in Hong Kong include municipal garbage incinerators, coal-burning, chemical waste incineration plants, clinical waste incinerators, landfill gas combustion, crematoria, animal carcass incinerators, and cement manufacturing.[59,60]

2.2. Types of other pollutants

Water pollutants, like textile dyes, are one of the major water pollutants, possess complex chemical structures, and are often carcinogenic. Their presence in water demands immediate attention, as they pose serious threats to aquatic ecosystems. Dyes are broadly categorized into two types: natural and synthetic.[61] Another common method of classification is based

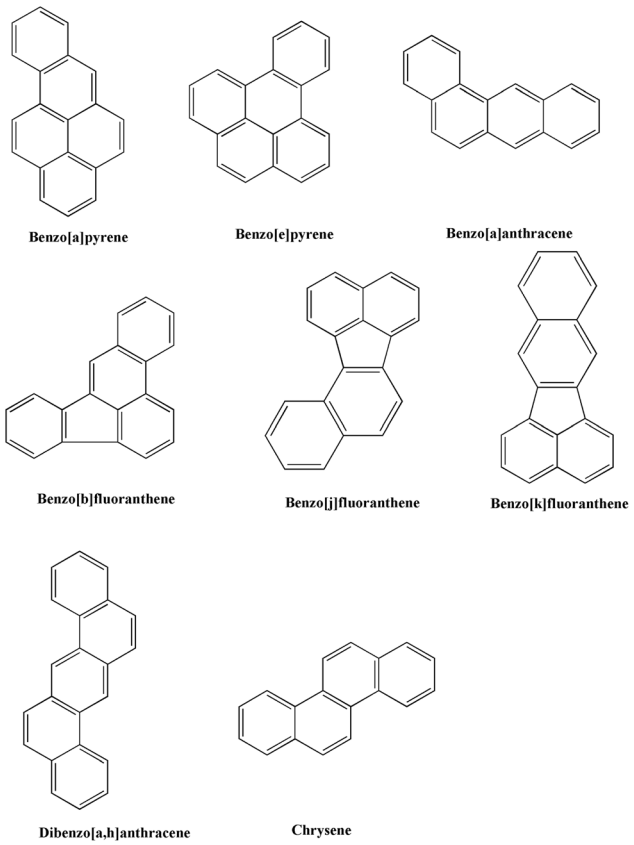

Fig. 2 Structure of PAHs recognized by European Commission.[51]

 © 2025 The Author(s). Published by the Royal Society of Chemistry

Open Access Article. Published on 02 September 2025. Downloaded on 11/10/2025 5:56:01 AM.
This article is licensed under a Creative Commons Attribution-NonCommercial 3.0 Unported Licence.

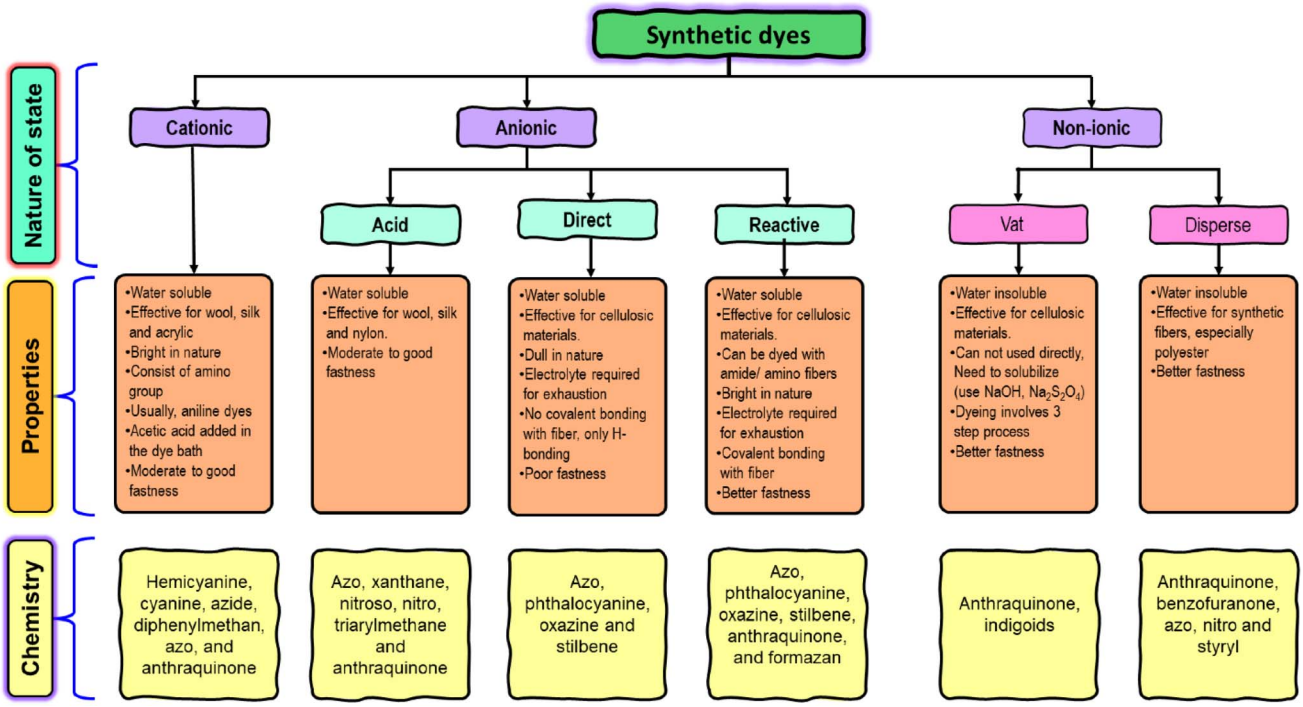

Fig. 3 Classification of dyes commonly employed in the textile industry.[62]

on the ionic nature they exhibit in aqueous solutions, dividing them into anionic, cationic, and non-ionic dyes.

Dyes can also be classified as acidic or basic, depending on the functional groups that influence their colour properties. Acid dyes are anionic in nature and typically contain acid groups such as sulphonate ($-SO_3^-$) or carboxylate ($-COO^-$) within their molecular structure. In contrast, basic dyes are cationic and are characterized by the presence of quaternary amine groups ($-NH_4^+$).[62] Additionally, based on their chemical structure, dyes encompass a wide range of functional groups, including azo, diazo, xanthene, indigoid, anthraquinone, nitro *etc.*[62] Fig. 3 shows the classification of dyes commonly employed in the textile industry.[62] Table 2 shows structure and types of various dyes.

3. Sources of POPs

POPs arise from applying pesticides in the environment, industrial waste, and the byproducts of industrial processes. They are emitted into the atmosphere from various industrial sources, including power stations, heating stations, incinerating plants, household furnaces, transportation, agricultural sprays, and evaporation from water, soil, and landfills. Additionally, unintentional production contributes to POPs through incineration, chemical processes, combustion, bushfires, and waste-containing PCBs. These sources are widespread, arising from activities such as obsolete oil use, equipment maintenance, building demolition, cement manufacturing, animal carcass incineration, coal combustion, landfill leaching, recycling operations, municipal and hazardous waste incineration, sewage sludge treatment, chlor-alkali and aluminum secondary plants, organochlorine pesticide production, and waste storage facilities for pesticides.[63,64] The following section elaborates on the global and regional sources of POPs and illustrates specific case studies from countries like India, Poland, and regions in Africa to highlight the diverse pathways of POP release and contamination.

3.1. Industrial emissions and waste management

Industries like textile dyeing, petrochemicals, pharmaceuticals, iron foundries, glassworks, oil refineries, and thermal power plants release inadequately treated wastewater into rivers and streams, spreading POPs. Additionally, electronic waste, which includes nearly 60 million tons produced globally, contains harmful brominated flame retardants (BFRs) such as bromodiphenyl ethers, tetrabromobisphenol A (TBBPA), hexabromocyclododecane (HBCD), and PCBs.[65]

3.2. Agricultural practices and pesticide use in India

Agricultural runoff is another significant source of POP contamination in-ground, surface, and drinking water, mainly consisting of pesticides and chemical fertilizers.[37] In India, the narrow genetic base of high-yielding crop varieties, monocropping, and tropical climate have made crops more vulnerable to pests and diseases. To manage these threats, farmers increasingly relied on pesticides, leading to resistance and overdependence on chemical control. As a result, pesticide use surged from 154 metric tons in 1954 to around 88 000 metric tons by 2000, a 570% increase. Although stricter regulations

Open Access Article. Published on 02 September 2025. Downloaded on 11/10/2025 5:56:01 AM.
This article is licensed under a Creative Commons Attribution-NonCommercial 3.0 Unported Licence.

Table 2 Structure and types of dyes

Structure	Name of the dye	Types
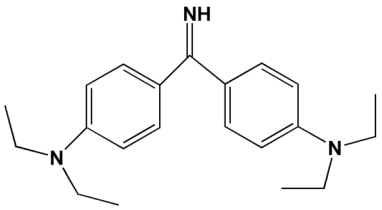	Basic yellow 37 (BY37)	Cationic dye
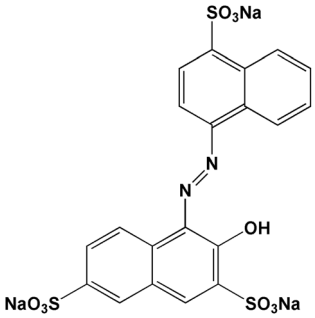	Red acid 27 (AR27)	Acid dye
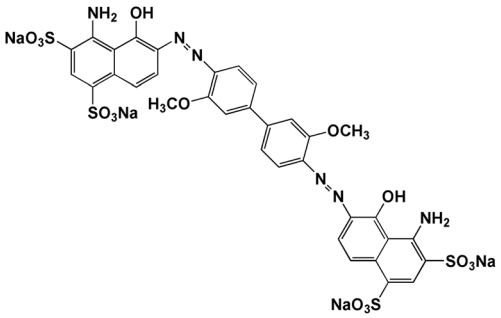	Direct blue 1 (BD1)	Direct dye
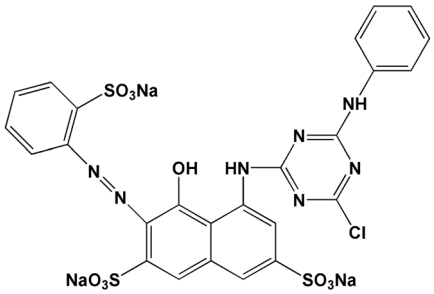	Reactive red 198 (RR 198)	Reactive dye
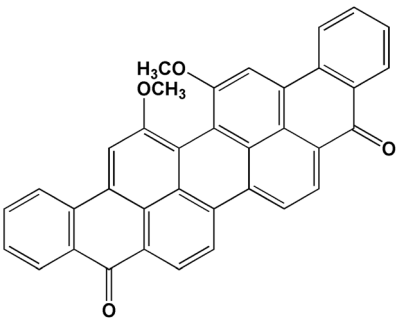	Vat green 1	Vat dye

 © 2025 The Author(s). Published by the Royal Society of Chemistry

Open Access Article. Published on 02 September 2025. Downloaded on 11/10/2025 5:56:01 AM.
This article is licensed under a Creative Commons Attribution-NonCommercial 3.0 Unported Licence.

Table 2 (*Contd.*)

Structure	Name of the dye	Types
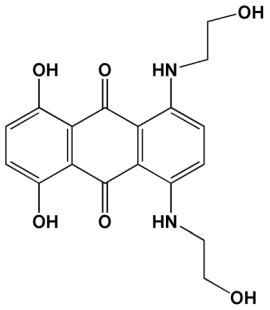	Blue disperse 7 (BD7)	Disperse dye

brought usage down to about 58 634 metric tons by 2015–16, recent data show a rise again to 62 193 metric tons in 2020–21 (Fig. 4), posing serious environmental and health concerns.[66] Despite laws such as Hudson's Pesticide Bylaw (Canada 1991) and The Insecticides Act (India 1968) aimed at restricting pesticide use, both consumption and pollution have continued to increase.[67] These pesticides might have contaminated the groundwater system as a non-point source of pollution from agricultural activities. In India, insecticides are the most commonly used pesticides.[68] West Bengal, an agriculturally dominant state in eastern India with one of the world's highest population densities, about 8% of India's population uses substantial amounts of pesticides for various livelihood activities.[69] The region's heavy agricultural practices result in extensive use of POPs, which can leach into ground and surface water used for drinking.

3.3. Natural and anthropogenic sources

POPs such as dioxins and dibenzofurans can be generated by natural activities such as volcanic activity and vegetation fires, with some volcanoes located in central Africa. Specifically, attention is drawn to sources and applications distinctive to southern and South Africa, encompassing natural fires, accidental incidents, and controlled vegetation burning.[70–72]

3.4. Environmental monitoring and case study

Poland lacks comprehensive investigations on dioxin-related environmental contamination, and available public data are

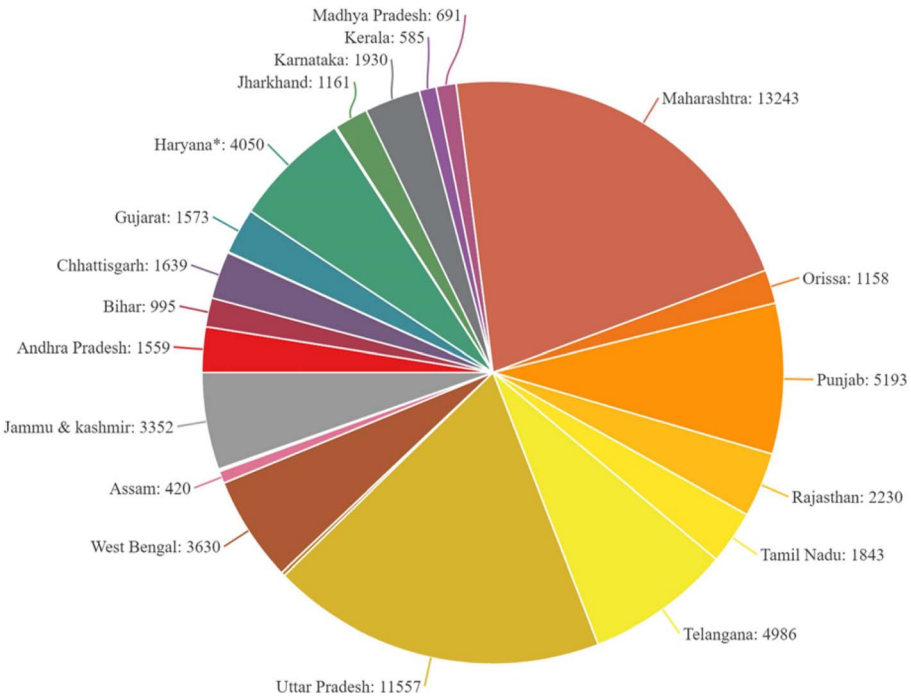

Fig. 4 Usage of pesticides in India inbetween 2020–2021.[66]

Open Access Article. Published on 02 September 2025. Downloaded on 11/10/2025 5:56:01 AM.
This article is licensed under a Creative Commons Attribution-NonCommercial 3.0 Unported Licence.

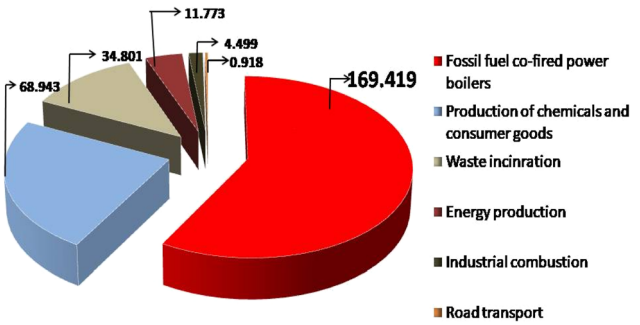

Fig. 5 Poland's primary sources of dioxin emissions.[38] "Reproduced from ref. 38 with permission from [Elsevier], copyright [2010]."

Table 3 Allowable amounts (pg-TEQ g^{-1}) of PCBs, DDT, and gamma-HCH

Substance	The acceptable amount of fat, pg-TEQ g^{-1}
PCBs	2.8
DDT	4.2
Gamma-HCH	13.3

limited and relies on faulty estimations. According to the Institute for Environmental Protection, as per information provided to the Central Statistical Office, estimates dioxin and furan emissions in 1998 at 290.353 grams TEQ in Poland. As identified by the Institute, the significant contributors to dioxin emissions in Poland are illustrated in Fig. 5.[38]

The Ministry of Environment of Poland, which manages environmental protection and climate related work, has recently taken important steps to measure the actual amounts of dioxin and furan emissions. For this, 118 geological samples were collected from different parts of Poland, including both urbanized areas and areas likely free from dioxin pollution. Analyzing these samples will help identify the natural background level of dioxins in the environment. In addition, Ludwicki *et al.* have presented a reference source for tracking these molecules in nursing mothers' breast milk and discussing the presence of other persistent organic pollutants.[73] The study included 462 women from Warsaw and several other areas under investigation. Table 3 summarizes the allowable concentrations (pg-TEQ g^{-1}) of PCBs, DDT, and gamma-HCH. Higher levels of persistent organic pollutants were primarily detected in women aged 30 and older and those who had given birth to more than four children.

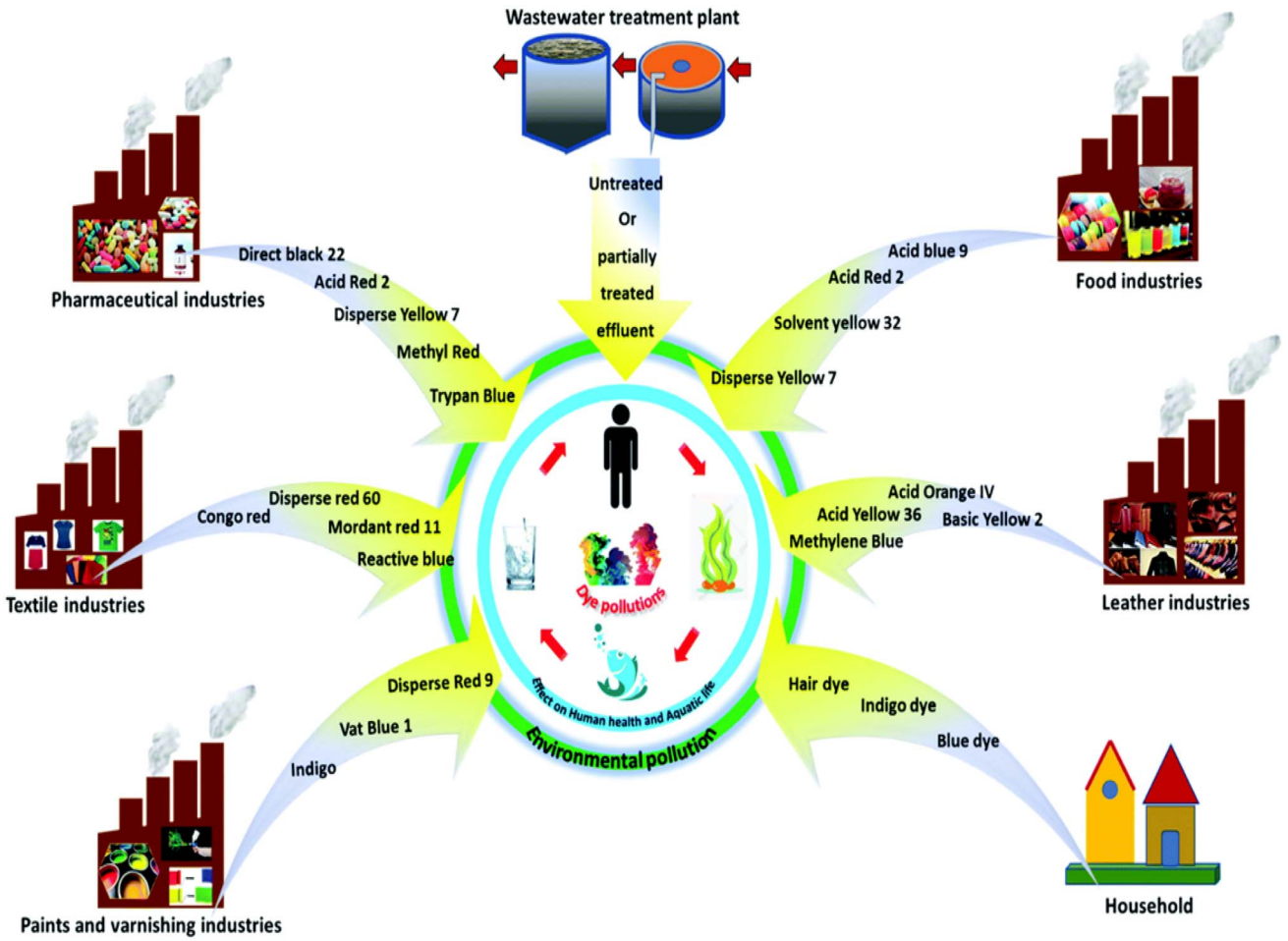

Fig. 6 Sources and routes by which dyes enter the environment.[76]

 © 2025 The Author(s). Published by the Royal Society of Chemistry

Open Access Article. Published on 02 September 2025. Downloaded on 11/10/2025 5:56:01 AM.
This article is licensed under a Creative Commons Attribution-NonCommercial 3.0 Unported Licence.

3.5. Other emerging contaminants of concern

Other pollutants responsible for water pollution, such as dyes and pharmaceutical compounds, are released into the environment from various sources, such as textile industries, household dyes, pharma companies, *etc.* Natural and anthropogenic sources are the two main sources of dyes. In contrast to synthetic colours, which are created by humans using a variety of organic compounds, natural sources include things like minerals, insects, and plants.[74,75] However, because dyes are used in so many different aspects of daily life, they are sometimes released from industrial effluents along with other hazardous organic and inorganic compounds, which has a negative impact on the environment.[75] Pollutants in the environment can originate from a variety of places, including factories, wastewater treatment plants, and even from households, as shown in Fig. 6.[76] Additionally, India's pharmaceutical, chemical, paint, and other industries are growing quickly and dumping their waste water into streams either directly or after some treatment. Pharmaceuticals have been found in drinking water sources and wastewater treatment plants. A small amount of drugs in drinking water for a long time could be very bad for people's health and aquatic life.[77,78]

4. Transportation and distribution of pollutants

As POPs degrade slowly, they remain in the environment for an extended period. Their transportation in fresh and marine waters occurs at low environmental concentrations.[38] One notable feature of persistent organic pollutants is their semi-volatility, allowing for sufficient atmospheric mobility. This facilitates the entry of considerable amounts into the atmosphere and their transportation over long distances.[79] This results in the widespread dispersion of POPs worldwide, reaching regions where they have never been utilized, contributing to their extensive global distribution.[80] The unexpectedly high POPs found in Alaska's Arctic region surprise many, especially considering the bans on some of these pollutants in the United States and Canada for many years. POPs tend to migrate towards colder areas like Alaska, where they settle due to the low temperatures, persisting for extended periods without easy degradation. This persistence allows them to transition from the air and water to the soil, plants, animals, and eventually humans. The revelation of persistent contaminants in the Arctic from distant sources emerged in the late 1970s when pesticides were discovered in polar bear fat tissue, revealing the far-reaching impact of atmospheric POPs on wildlife and human health.[81] During atmospheric transport, POPs undergo various processes such as degradation, deposition onto soils, vegetation, or water bodies, revolatilization, sedimentation, and bioaccumulation. These processes, illustrated in Fig. 7,[82] play a crucial role in determining the fate of POPs in the global environment. Specifically, the study by Fernández and Grimalt (2003) highlights that the polycyclic aromatic hydrocarbons (PAHs) are predominantly transported through the atmosphere *via* their association with particulate matter, with wet and dry deposition being the key mechanisms responsible for their atmospheric removal.[83] Organochlorine compounds (OCs) infiltrate land and water systems predominantly through atmospheric gas-phase interactions. Their low volatility, coupled with temperature-dependent behavior, leads to selective accumulation in colder, high-altitude zones-where cooler climates act as environmental traps for these persistent pollutants. Together, these mechanisms drive the global distillation effect, enabling the gradual migration of POPs from warmer latitudes to colder climates. This underscores the necessity of understanding these transport mechanisms to evaluate the broader environmental consequences of these pollutants.[83]

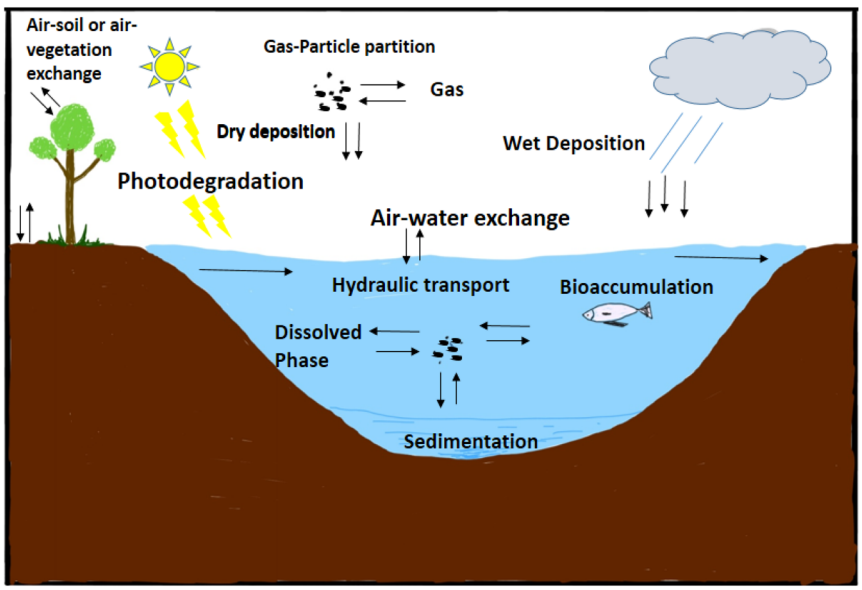

Fig. 7 Environmental processes occur when POPs are transported across vast distances through the atmosphere.[82]

Open Access Article. Published on 02 September 2025. Downloaded on 11/10/2025 5:56:01 AM.
This article is licensed under a Creative Commons Attribution-NonCommercial 3.0 Unported Licence.

Given that numerous physicochemical properties influencing the environmental fate of POPs are temperature-dependent, the theory of the Global Distillation Effect predicts the migration of gas phase contaminants from warmer regions of the planet, such as tropical or temperate source areas, to colder, higher latitude regions (as shown in Fig. 8).[82] This decrease in temperature affects the vapor pressure and Henry's law constant of these compounds, increasing their propensity to condense and accumulate on surfaces like atmospheric particles, soils, vegetation, and aquatic ecosystems, from which they can infiltrate food chains. Depending on their volatility, different POPs will condense at varying ambient temperatures, producing a fractionation of these chemicals within the Earth.[82,84,85] The movement of compounds from low to high latitudes occurs through condensation and volatilization steps, known as the grasshopper effect. These steps involve the exchange of compounds between the air and terrestrial surfaces, driven by seasonal temperature changes at mid-latitudes. Eventually, most POPs would accumulate in polar regions, where the low ambient temperature traps them-an effect referred to as the cold finger or cold trap.[84]

In the last ten years, several studies have shown global POP concentration patterns that align with this distribution mechanism. For instance, there's been a noticeable increase in hexachlorobenzene (HCB) levels in tree bark as one moves from the equator toward northern regions.[86,87] Latitudinal patterns have also been documented for PCBs, particularly the more volatile congeners, HCHs, and HCB, across various environmental compartments like air,[88] sediments,[89,90] and soil.[91,92] Recently, PBDE, employed as flame retardants and not listed as POPs, has been discovered in significant amounts in Arctic ringed seals.[93]

5. Health effects

Hydrophobic POPs possess considerable fat solubility, contributing to their advantageous bioaccumulation and extended persistence, which enhances their toxicity.[94,95] In general, POPs move from one organism to another, accumulating in high concentrations, a process referred to as biomagnification. Recently, there has been growing public concern regarding POP contamination, primarily due to the identification of several compounds as hormone disruptors. These substances can potentially interfere with the normal functioning of the endocrine and reproductive systems in both humans and wildlife. Their presence in the environment poses numerous risks without benefitting the Earth. Once released, these pollutants can persist for decades, leading to various adverse effects such as cancer, congenital disabilities, learning disabilities, and immunological, behavioral, neurological, and reproductive disorders in humans and other animal species.[96] Evidence suggests that a significant number of people globally may have accumulated sufficient levels of POPs in their body fat, leading to severe health consequences such as illness and death (Fig. 9).[97] Studies conducted in both laboratory settings and natural environments have linked POPs to a range of health issues, including endocrine disruption, reproductive and immune dysfunction, neurobehavioral disorders, and cancer.[98,99] Recently, particular POPs have been linked to decreased immunity in infants and children, leading to a simultaneous rise in infections, as well as developmental abnormalities, neurobehavioral impairment, and the initiation or promotion of cancer and tumors. Additionally, some researchers are exploring the potential role of certain POPs as significant risk factors in the development of human breast

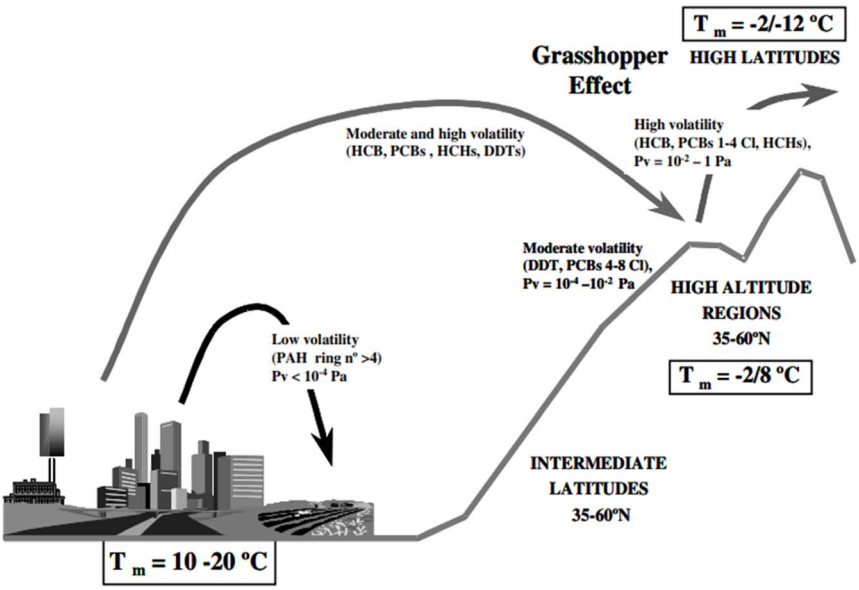

Fig. 8 Diagram illustrating the Global Distillation Effect *via* the grasshopper mechanism in temperate regions, with P_v indicating the vapor pressure and T_m representing the mean air temperature in each area.[82]

 © 2025 The Author(s). Published by the Royal Society of Chemistry

Open Access Article. Published on 02 September 2025. Downloaded on 11/10/2025 5:56:01 AM.
This article is licensed under a Creative Commons Attribution-NonCommercial 3.0 Unported Licence.

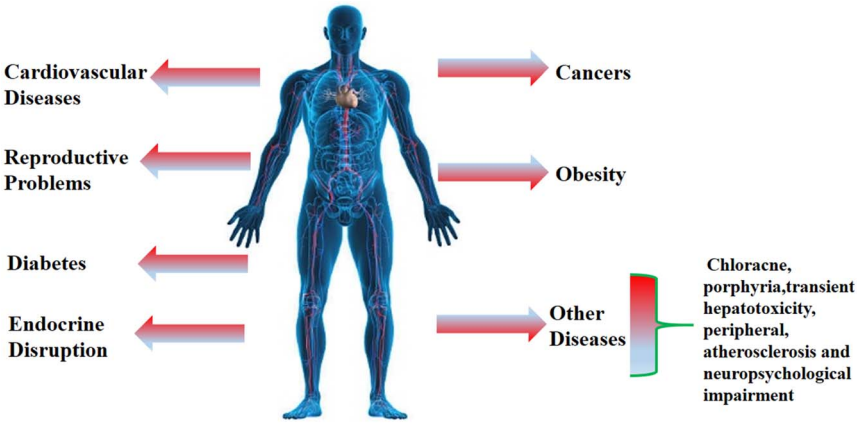

Fig. 9 Various health problems are due to exposure to POPs.[97]

cancer.[38,100] Below are outlined several prominent health issues linked to POPs.

5.1. Endocrine disruption

Disruption of the endocrine system leads to various diseases and health issues. Endocrine disrupting compounds interfere with hormonal regulations, leading to detrimental effect on neurophysiological function, immune system and reproductive health across both human and animal populations. All members of the "dirty dozen" group of POPs have been identified as endocrine disruptors that impair hormone functions. Research suggests that the effects of POPs during fetal development persist throughout an individual's lifespan.[101] Most pesticides that disrupt the endocrine system are belongs to the organochlorine class, including DDT, dieldrin, toxaphene, chlordane, mirex, endosulfan, and others. These substances mimic estrogen and cause changes to the reproductive organs.[102] Children displaying heightened startle responses, decreased motor reflexes, neuromuscular functions, and diminished responsiveness showed neuro-behavioral deficits. These included hypoactive reflexes, impaired visual recognition, and short-term memory impairments observed around the age of 7 months. By 4 years of age, issues such as reduced weight progression, decreased responsiveness, and impaired visual recognition were noticeable.[103,104]

Langer *et al.*[105] documented extensive industrial contamination of PCBs in the Michalovce region of East Slovakia from 1955 to 1984. Despite the passage of time, residual contamination persists, with affected residents displaying abnormal thyroid function, elevated urinary iodine levels, and increased serum concentration of 15 distinct PCB congeners-pointing to continued endocrine disruption.

5.2. Reproductive problems

Reproductive issues and diseases encompass dysfunctions in both male and female reproductive systems, leading to conditions such as congenital disabilities, preterm birth, developmental disorders, low birth weight, impotence, reduced fertility, and menstrual disorders.[1] Numerous studies have revealed the detrimental effects of POPs on human health. According to a review by Gao and Wu, different cells in the testes, including testicular germ, Leydig, and Sertoli cells, exhibited varied responses to PCB pollutants.[106] In 2002, Damstra elucidated the effects of POPs on the reproductive system, indicating that exposure to these pollutants led to diminished sperm quality and quantity. Furthermore, they were associated with disruptions in sex ratios and the onset of early puberty.[101] Vizcaino *et al.* conducted a fascinating study exploring the transmission of POPs from mothers to their offspring. Their research revealed that Spanish mothers transferred 14 organochlorine pesticides, 7 polychlorinated biphenyls, and 14 PBDEs to their unborn fetuses. These POP concentrations were notably higher in the mothers' serum than in the samples from the umbilical cord and 50 placentas examined. The authors provided insights into the active transport of POPs across the placenta.[107] Giwercman *et al.* detailed the impact of PCBs and *p*,*p*′-DDE exposures on the alteration of sperm Y : X chromosome ratio in the Faroe Islands. Additionally, they observed a diminished Y : X ratio in men from this region.[108]

5.3. Cancer

Cancer is a severe illness where cells grow and spread uncontrollably. It's dangerous because it's hard to predict and treat. Normal cells become cancer cells for many different reasons, both inside and outside the body.[109] Increased levels of POPs within low-density lipoproteins contribute to the developing of several types of cancer.[110] Several reviews discuss the cancers induced by POPs.[111,112] The International Agency for Research on Cancer has categorized 2,3,7,8-tetrachlorodibenzo-*p*-dioxin (2,3,7,8-TCDD) as a Group 1 carcinogen, indicating it poses a significant risk to human health.[113] Different experts are also exploring the potential impact of certain POPs as substantial risk factors in the development of human breast cancer.[100] Yu *et al.* studied the relationship between seafood intake and cancer susceptibility by analyzing global concentrations of various contaminants in marine products, including OCPs, PBDEs, PCDDs, PCDFs, as well as both dioxin-like and non-dioxin-like PCBs. The researchers found that populations in

Open Access Article. Published on 02 September 2025. Downloaded on 11/10/2025 5:56:01 AM.
This article is licensed under a Creative Commons Attribution-NonCommercial 3.0 Unported Licence.

Europe experienced the highest dietary exposure to PCDD/Fs and DL-PCBs, followed by those in North America and Asia.[114] In a comprehensive study conducted in Spain in 2003, Arrebola *et al.* assessed the bioaccumulation of POPs in human adipose tissue from 368 participants. Utilizing Cox-regression analysis, they demonstrated a positive correlation between PCB levels and cancer risk, highlighting the potential oncogenic effects of long-term PCB exposure.[115,116] Meanwhile, Mathur *et al.* performed an epidemiological study in Jaipur, India, focusing on the etiological role of organochlorine pesticide exposure-namely DDT, its primary metabolite DDE, dieldrin, heptachlor, and various isomers of HCH (α, β, γ)-in the incidence of breast cancer among women. They found that high levels of these POPs were associated with elevated breast cancer risks.[117] However, the study did not mention the specific period during which the investigation was conducted.

5.4. Cardiovascular problems

Globally, cardiovascular disorders represent the foremost contributors to death, comprising a broad spectrum of ailments including hypertension, angina pectoris, cardiac arrhythmias, and more.[118] POPs contribute to the developing of these health issues. It's widely acknowledged that POPs, being mostly lipophilic, tend to bioaccumulate in high-density lipoproteins, thereby contributing to a range of cardiovascular problems and diseases.[110] Lee *et al.* documented a significant association between cardiovascular dysfunction and the accumulation of POPs in the serum of 90 individuals. Among the culprits, organochlorine pesticides, polychlorinated biphenyls, and polybrominated biphenyl were pinpointed as key contributors to these cardiovascular abnormalities.[119] Valera *et al.* conducted a comprehensive investigation into the association between hypertension and the exposure to PCBs and organochlorine (OC) pesticides among Arctic populations. The study encompassed a cohort of 1614 adults from 9 towns and 13 villages in Greenland, with concentrations of these POPs quantified and analyzed. Utilizing logistic regression models where POPs were treated as continuous variables, the authors identified a significant positive correlation between higher POP concentrations and the prevalence of hypertension.[120]

5.5. Other health problems

Moreover, beyond the above-mentioned health effects and diseases, POP pollution is associated with other health issues such as chloracne, transient hepatotoxicity, porphyria, neuropsychological impairment, and peripheral atherosclerosis.[121] Other sources in the literature also discuss various health issues associated with the contamination of POPs.[122–133] Apart from POPs, many diseases that affect both humans and animals have been connected to textile dyes, which are extremely hazardous and may even cause cancer.[134] Fig. 10 shows the range of illnesses that textile dyes can induce.[135] These include

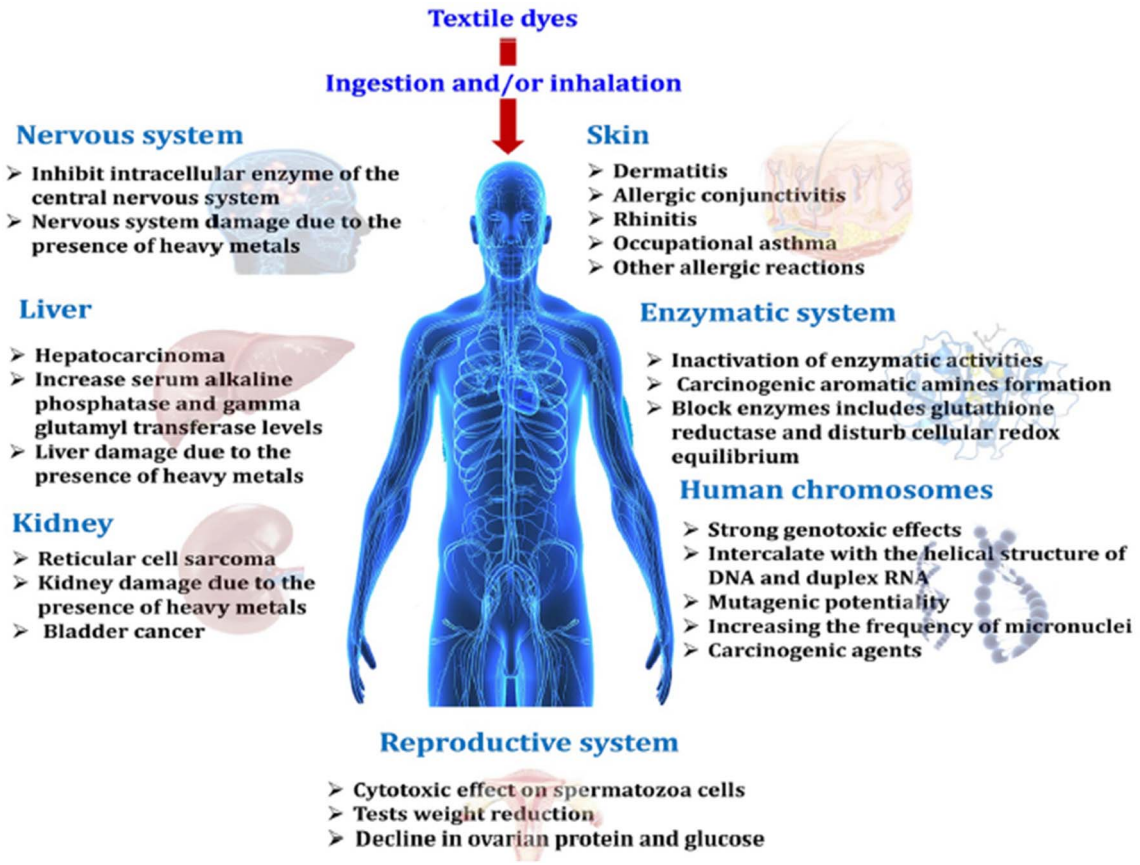

Fig. 10 Health risks associated with textile dyes.[135] "Reproduced from ref. 135 with permission from [Elsevier], copyright [2022]."

 © 2025 The Author(s). Published by the Royal Society of Chemistry

Open Access Article. Published on 02 September 2025. Downloaded on 11/10/2025 5:56:01 AM.
This article is licensed under a Creative Commons Attribution-NonCommercial 3.0 Unported Licence.

dermatitis, central nervous system issues, and more. One possible explanation for these issues is that enzymes become inactive due to the replacement of their cofactors.[136]

6. Photocatalytic degradation of POPs and other pollutants

Photocatalysis involves catalyzing a photoreaction to accelerate its speed.[137] Photocatalysis operates straightforwardly: when a photon with energy equal to or greater than the bandgap energy strikes, it generates a pair of charge carriers. This energy transformation initiates the formation of electrons and holes.[138] These electrons and holes, induced by light, interact with O_2, H_2O, and –OH group, producing active ROS like $^{\bullet}OH$ and $O_2^{\bullet-}$ with potent oxidation capabilities.[139] After fluorine, these hydroxyl radicals hold the second-strongest oxidation potential (2.8 eV).[140] These radicals are highly reactive, quickly interacting with organic molecules at rate constants typically ranging from 10^6 to 10^9 mol L^{-1} s^{-1}.[141] These radicals initiate sequential reactions with contaminants on the photocatalyst's surface, leading to the degradation of organic pollutants.[142]

Despite certain drawbacks, such as the inability to function in solar radiation, challenges in reactor design, limitations in catalyst reusability and recovery, lower quantum efficiency, and occasional production of toxic metabolites, it's essential to address these issues in photocatalysis research before practical application. Some catalysts like CdS and PbS may also exhibit toxicity.[143] Another limitation in photocatalysis arises from the swift recombination of electron–hole pairs, which can impede reaction progress. Doping the catalyst with metal oxide nanomaterials offers a solution by hindering this recombination. This approach extends the lifespan of electron–hole pairs, facilitating redox reactions on the catalyst's surface.[144]

6.1. Principle of heterogeneous photocatalysis

The term "heterogeneous" denotes a system where the catalyst is in the solid phase while contaminants exist in the aqueous phase. This setup uses multiple phases alongside a light source (UV/solar radiation) with the catalyst present. Semiconductors such as TiO_2, ZnO, ZnS, *etc.*, are commonly employed as catalysts in these heterogeneous processes. The photocatalyst becomes activated upon exposure to UV radiation, initiating a redox environment within the reaction medium.[145,146] The central aspect of the entire process centers around the production of hydroxyl radicals, which are crucial for converting a range of toxic or non-biodegradable pollutants into harmless end products like CO_2, H_2O, and other environmentally beneficial compounds.[147]

When a semiconductor absorbs a photon with energy equal to its bandgap energy, an electron transitions from the valence band to the conduction band, leaving behind a hole (h_{vb}^+) in the valence band (VB). This process is known as generating an "electron–hole (e^-/h^+) pair." The holes in the valence band act as potent oxidizing agents (+1.0 to +3.5 V *vs.* the normal hydrogen electrode, depending on pH and material), while the electrons in the conduction band serve as powerful reducing agents (+0.5 to −1.5 V *vs.* the normal hydrogen electrode, depending on pH and material).[148] To prevent recombination with the trapped hole, it's crucial for the electron in the conduction band (CB) to be captured by an electron acceptor. On the catalyst's surface, the electron and hole unite for the redox reaction, where the photo-generated electron reacts with oxygen to form superoxide anion radicals. Meanwhile, the hole (h_{vb}^+) directly oxidizes the pollutant, generating hydroxyl radicals $^{\bullet}OH$. Additionally, the electron (e_{cb}^-) efficiently reduces the oxygen adsorbed by the catalyst.[147,149–151] To ensure effective photocatalytic degradation, the reduction of oxygen must coincide with the oxidation of contaminants. This prevents the accumulation of electrons in the CB, which would otherwise reduce the rate of electron and hole recombination, thereby impeding the degradation reaction.[152,153]

6.2. Mechanism of photocatalysis

The mechanism and theory behind semiconductor-based photocatalysis have been extensively explored in various literature.[154] As per Herrmann,[155] heterogeneous photocatalytic processes consist of five steps, namely:

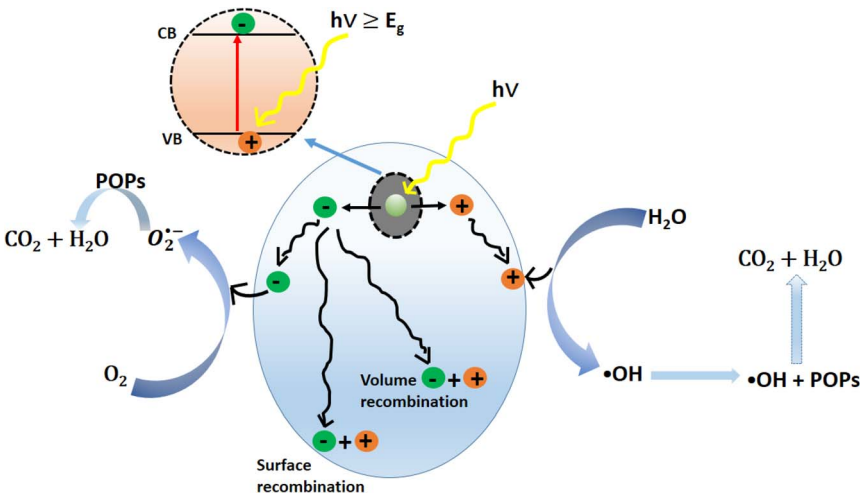

Fig. 11 The typical process for eliminating POPs through photocatalysis.

Open Access Article. Published on 02 September 2025. Downloaded on 11/10/2025 5:56:01 AM. This article is licensed under a Creative Commons Attribution-NonCommercial 3.0 Unported Licence.

(1) Surface transfer of reactants, (2) at least one of the reactants being adsorbed, (3) adsorbed phase reaction of the reactants, (4) product's desorption, and (5) product's diffusion from the surface.

In the context of utilizing MX (here M: Ti, Zn *etc.* and X: O, S *etc.*) as the photocatalyst, the way that heterogeneous photocatalysis work is outlined as follows:

$$\text{Photocatalyst (MX)} + h\nu\ (\lambda < 380\ \text{nm}) \rightarrow \text{MX}\ (e_{\text{conduction band}}^{-} + h_{\text{valence band}}^{+}) \quad (1)$$

Here, $e_{\text{conduction band}}^{-}$ and $h_{\text{valence band}}^{+}$ acting as reducing and oxidizing agents, respectively. The oxidation and reduction of POPs are as follows:

6.2.1. Oxidative reaction.

$$\text{Organic pollutant} + h_{\text{valence band}}^{+} \rightarrow \text{oxidation products MX}\ (h_{\text{valence band}}^{+}) + H_2O \rightarrow \text{MX} + H^{-} + {}^{\bullet}\text{OH} \quad (2)$$

This reaction follows OH^{-} ion neutralization into $^{\bullet}OH$ by the h^{+}:

$$\text{MX}\ (h_{\text{valence band}}^{+}) + OH^{-} \rightarrow \text{MX} + {}^{\bullet}\text{OH} \quad (3)$$

$$h^{+} + \text{organic pollutant} \rightarrow \text{metabolites} \rightarrow CO_2 + H_2O \quad (4)$$

6.2.2. Reductive reaction.

$$\text{Organic pollutant} + e_{\text{conduction band}}^{-} \rightarrow \text{reduction products}$$

Here, $O_2^{\bullet-}$ formed by the electron as follows:

$$\text{MX}\ (e_{\text{conduction band}}^{-}) + O_2 \rightarrow \text{MX} + O_2^{\bullet-} \quad (5)$$

$$O_2^{\bullet-} + H^{+} \rightarrow HO_2^{\bullet} \quad (6)$$

$$HO_2^{\bullet} + H^{+} + \text{MX}(e_{\text{conduction band}}^{-}) \rightarrow H_2O_2 + \text{MX} \quad (7)$$

$$^{\bullet}\text{OH} + \text{organic pollutant} \rightarrow \text{metabolites} \rightarrow CO_2 + H_2O \quad (8)$$

In the steps outlined above, generating radical $^{\bullet}OH$ and superoxide anion radical ($O_2^{\bullet-}$) are crucial for driving the photocatalytic oxidation reaction.[30,147] Fig. 11 represents the typical process for eliminating POPs through photocatalysis.

7. Metal oxides as a photocatalyst

To date, oxides of various metals/semiconductor-based nanomaterials, including TiO_2, SnO_2, ZnO, Fe_2O_3, ZrO_2, WO_3, CuO, Cu_2O, CdS, *etc.*, have been researched for their ability to break down photocatalytically organic pollutants into harmless gaseous products.[156,157] This section reviews the latest developments in applying different metal oxide nanoparticles and composites of these oxides for the photocatalytic degradation of organic contaminants.

7.1. Titanium dioxide

TiO_2 was the first photocatalyst to be reported. It is regarded as a promising and viable choice because of its affordable price, extensive occurrence, inertness in both chemical and biological systems, photocatalytic stability, and minimal environmental impact.[158–160] TiO_2 has five distinct forms: anatase, rutile, brookite, monoclinic, and orthorhombic. The photocatalytic performance of these is highest in anatase and then in rutile. TiO_2 has a large band gap energy (3.2 eV for anatase and 3.03 eV for rutile), permitting photons in the near-UV range to be absorbed (λ < 387 nm).[161] Under sunlight exposure, electrons in the valence band jump to the conduction band, forming electron–hole pairs. Under alkaline conditions, the holes (h^{+}) in the valence band transform hydroxyl groups and water molecules into hydroxyl radicals. Meanwhile, photoinduced electrons in the conduction band reduce dioxygen, which interacts with H_2O to form H_2O_2, which is a strong oxidizer. These potent oxidizers then react with the target pollutants near the photocatalysts, slowly decomposing them into harmless and non-toxic compounds, such as CO_2 and H_2O.[162] An extensive spectrum of organic dyes, including orange G, malachite green, amido black 10B, Safranine O'azure II, rhodamine 6G, alizarin green, Sudan III, indigo carmine, solvent red 23, and others, were degraded upon UV light exposure in the presence of TiO_2 as a photocatalyst.[163] Bandala *et al.* found in 2002 that aldrin could be degraded into dieldrin, chlordane, and 12-hydroxy dieldrin by employing TiO_2.[164] According to Bin *et al.*, dicofol can be fully degraded in under 2 hours when exposed to UV radiation and TiO_2.[165] In another experiment, Thomas *et al.* found that endosulfan could be nearly completely broken down utilizing photocatalytically active solar TiO_2.[166]

The anatase and rutile phases of TiO_2, defined by their wide bandgap (3.0–3.2 eV), demonstrate photocatalytic activity when exposed to near-ultraviolet radiation, which accounts for only 4% of the electromagnetic spectrum.[167] Hence, substantial attempts have been made to modify and introduce dopants into nanostructures based on TiO_2 to enable them to function as active photocatalysts under visible light.

7.2. Zinc oxide

Zinc oxide nanomaterials exhibit significant promise as photocatalysts due to their high quantum effectiveness, excellent stability, affordability, and eco-friendly characteristics.[168,169] Zinc oxide, with a band gap of 3.25 eV, is comparable to TiO_2 (3–3.25 eV) and is commonly used to degrade water contaminants such as organic pollutants under light exposure.[170] Zinc oxide has a photocatalytic degradation mechanism closely similar to TiO_2; thus, ZnO nanomaterials are also being explored as a substitute for titania in water detoxification processes.[171] In the study of semiconductors, ZnO demonstrated superior photocatalytic performance compared to other materials, attributed to its enhanced ability to absorb a more significant portion of the electromagnetic spectrum. Furthermore, researchers investigated the fluorescence emission properties of ZnO nanoparticles for their potential application in the photocatalytic degradation of various organic hazards.[172] The

 © 2025 The Author(s). Published by the Royal Society of Chemistry

Open Access Article. Published on 02 September 2025. Downloaded on 11/10/2025 5:56:01 AM.
This article is licensed under a Creative Commons Attribution-NonCommercial 3.0 Unported Licence.

fluorescence intensity observed in the emission spectra of ZnO is linked to the recombination mechanism of electrons and holes. The photoinduced holes are effectively scavenged by organic compounds on ZnO's surface, which competes with the charge recombination process that produces ZnO fluorescence emission. Consequently, the intensity of fluorescence emission spectra diminishes due to the photo-reaction between ZnO nanomaterials and organic pollutants. Therefore, ZnO nanoparticles demonstrate effective detection and photocatalytic degradation of organic contaminants in aqueous systems.[172] According to Reddy *et al.*, dicofol can be degraded by 88.4% using ZnO nanoparticles in 1.6 h at 450 °C in a slightly alkaline solution.[173]

Furthermore, pure ZnO nanoparticles exhibit absorption only in the UV band of the electromagnetic spectrum, which accounts for approximately 4% of the total electromagnetic spectrum. Therefore, enhancing the response to visible light is crucial, as it encompasses about 43% of the electromagnetic spectrum, significantly larger than the UV range.[174] Moreover, ZnO's wide bandgap allows the photoinduced electrons and holes to recombine easily, limiting the material's photocatalysis capacity.[175] Various methods have been developed to enhance the visible light response and mitigate the speed at which photoinduced electron–hole pairs in ZnO nanoparticles recombine. One well-known method is doping with metal ions and metals, which reduces electron–hole recombination and broadens its response to the visible range of the spectrum. For example, Lu *et al.* synthesized cobalt-doped ZnO (ZnO : x% Co, where $x = 0.5$, 1, and 1.5) *via* a simple hydrothermal method and evaluated its photocatalytic efficiency against alizarin red dye under visible light irradiation.[176] The Co-doped ZnO samples exhibited a broader light absorption range compared to pure ZnO, with the 1% Co-doped sample achieving approximately 93% degradation of the dye within 60 minutes.[176] This enhanced performance was attributed to strong electronic interactions between Co and ZnO, which facilitated improved charge separation and transfer while suppressing the recombination of photogenerated electron–hole pairs, thereby enhancing visible-light-driven photocatalytic activity.[176] Similarly, Ahmad *et al.* prepared nickel-doped ZnO photocatalysts ($Zn_{1-x}Ni_xO$, where $x = 0.0$–0.5) using a wet chemical method and assessed their activity against methylene blue (MB) under visible light.[177] While pure ZnO exhibited relatively low degradation efficiency, the Ni-doped variants showed significantly improved photocatalytic performance. This enhancement was ascribed to the role of Ni in promoting charge carrier separation by trapping electrons, thereby reducing electron–hole recombination, which is a key factor limiting photocatalytic efficiency.[177]

7.3. Tin dioxide

Being n-type semiconductor it finds diverse applications across catalysts, gas sensing, transistors, batteries, and transparent electrodes.[178–180] The better photocatalytic propensity of SnO_2 is predicted by the elevated surface-to-volume ratio of the nanoparticles, which increases active sites. Pure SnO_2 is seldom studied because the photocatalytic process leads to the simultaneous formation of Sn^{2+} and Sn^0. Consequently, the catalyst may be presented as SnO_2, SnO, or Sn. SnO_2, with its large E_g of 3.6 eV, like TiO_2, is also an ultraviolet-sensitive metal oxide semiconductor.[181] Although doped SnO_2 is commonly used in the organic contaminant's photodegradation process, there are examples where the undoped material demonstrates effectiveness in the photocatalytic process. However, due to the considerable bandgap energy of pure SnO_2, UV light is necessary for triggering the metal oxide, as visible light lacks the energy required to efficiently generate e^-–h^+ pairs. SnO_2 nanocrystals prepared from amino acid-chelated tin salts were used in detoxification studies of rhodamine B. This approach led to a nearly 100% reduction in rhodamine B concentration after 150 minutes of irradiation.[182,183] Comparable results were achieved with nanocrystalline SnO_2 particles synthesized from tin oxalate *via* a membrane of eggshell in rhodamine B degradation studies. Following one hour of exposure to UV light, the author observed an astounding 95% decrease in dye concentration.[184] Undoped SnO_2 nanoparticles were also effectively utilized in the oxidative breakdown of methylene blue, eosin Y,[185] congo red,[186] and violet 4 dyes.[182]

7.4. Iron oxide

Iron oxide, an n-type semiconductor, is widely accessible and demonstrates photocatalytic activity for degrading organic contaminants.[187] The activation of Fe_2O_3 under visible light is due to its reduced energy band gap (2.2 eV).[188] Iron oxide powder was used to photo-degrade azo dyes, producing substituted benzene and naphthalene, which were then oxidized and mineralized into CO_2 and H_2O.[189] Nanoparticles of Fe_2O_3 with crystal sizes of 35 nm, 100 nm, and 150 nm were used to degrade Congo red. Notably, the 35 nm Fe_2O_3 nanoparticles completely degraded Congo red both with and without exposure to visible light, suggesting no significant impact of light on the catalytic process.[190] This activity in the absence of light may be attributed to a Fenton-like mechanism, where Fe^{3+}/Fe^{2+} redox cycling facilitates the generation of $^{\bullet}OH$ radicals from H_2O_2, leading to oxidative degradation of the tested pollutant.[191,192] However, the apparent rate constant for Congo red decomposition was higher in light than in dark conditions.[190]

However, the application of pure Fe_2O_3 in photocatalysis is limited by several shortcomings, such as low movement of non-dominant charge carriers, slow surface kinetics, short diffusion lengths of photoinduced carriers, and fast recombination dynamics.[193] Doping various metals or metal oxides into iron oxide nanostructures, alongside the design of iron oxide-based nanocomposites, can effectively control charge carrier recombination events, enhancing overall activity. Among them, transition metal doping has proven particularly effective in boosting the degradation rate of organic pollutants.[194] Nanostructured metal additives serve as light-harvesting centers, enhancing solar energy utilization at the catalyst surface.[195] This not only shifts the optical response by narrowing the band gap but also extends absorption into the visible region.[196] In particular,

Open Access Article. Published on 02 September 2025. Downloaded on 11/10/2025 5:56:01 AM.
This article is licensed under a Creative Commons Attribution-NonCommercial 3.0 Unported Licence.

doping Fe_2O_3 with transition metals improves its efficiency, durability, and recyclability, making it a compelling material for advanced wastewater treatment applications.[197] For example, Cheema *et al.* synthesized Nb-doped Fe_2O_3 with varying doping concentrations (2, 4, and 6 mmol) using a hydrothermal method.[198] Nb doping led to a significant reduction in particle size (from 93.74 nm to 56.01 nm) and improved stability, as indicated by the zeta potential shifting from −13.04 mV to −37.31 mV.[198] Optical studies revealed a red shift in the band gap energy from 3.08 eV to 2.28 eV, attributed to the introduction of Nb-induced energy levels. Among the samples, 6 mmol Nb-doped Fe_2O_3 exhibited the highest photocatalytic activity, achieving 87% degradation of 10 ppm methylene blue under sunlight within 2 hours. The enhanced performance was ascribed to suppressed electron–hole recombination and increased generation of reactive radicals. Upon light exposure, electrons in Fe_2O_3 are excited from the valence band to the conduction band, forming electron–hole pairs. These charges migrate to the surface and drive redox reactions. Holes (h^+) directly oxidize methylene blue, while electrons react with oxygen to form superoxide ($O_2^{\bullet-}$), which converts into hydroxyl radicals ($^{\bullet}OH$), enhancing degradation. The proposed mechanism under UV and sunlight is shown in Fig. 12.[198]

7.5. Tungsten oxide

The first documented research regarding the photocatalysis of tungsten oxide (WO_3) dates back to 1976.[199] WO_3 is recognized because of its remarkable light-harvesting capability due to a narrow E_g (2.5–2.8 eV), tunable composition, widespread natural availability, strong h^+-driven oxidation potential, and excellent environmental durability.[200] Among the studied morphologies of WO_3 are nanoparticles, nanoflakes, nanowires, and nanofibers.[201] The synthesis of tungsten oxide *via* the solvothermal method, having a hierarchical structure with a hollow pattern, has garnered interest as a reusable adsorbent for the degradation of organic contaminants.[201]

However, due to the rapid recombination of photoinduced charge carriers and a low level of conduction band above the reduction potential of O_2/O^{2-}, the photocatalytic efficiency of WO_3 has been constrained, leading to a diminished rate of O_2 molecule reduction.[202] Various approaches, including doping, bandgap manipulation, and structural adjustments, have been used for the better photocatalytic performance of WO_3.[203] For instance, Gokila *et al.* synthesized Y^{3+}-doped WO_3 nanoparticles (2%, 4%, and 6%) using a co-precipitation method.[204] Pure WO_3 showed densely packed particles with rough surfaces and low porosity. With 2% and 4% Y doping, the particles became more loosely packed, slightly increasing porosity and reactive sites. At 6% Y doping, the particles formed a flower-like structure with petal shapes, greatly increasing surface area and active sites, ideal for photocatalysis. Band gap analysis showed a gradual decrease from 2.82 eV (pure WO_3) to 2.67 eV (6% Y-doped), which improves charge transfer and enhances photocatalytic activity. They further evaluated the photocatalytic efficiency of undoped and Y-doped WO_3 nanoparticles for the degradation of malachite green (MG) dye under visible light. Pure WO_3 nanoparticles degraded 68% of the dye within 180 minutes, while 6 wt% Y-doped WO_3 exhibited the highest efficiency, degrading

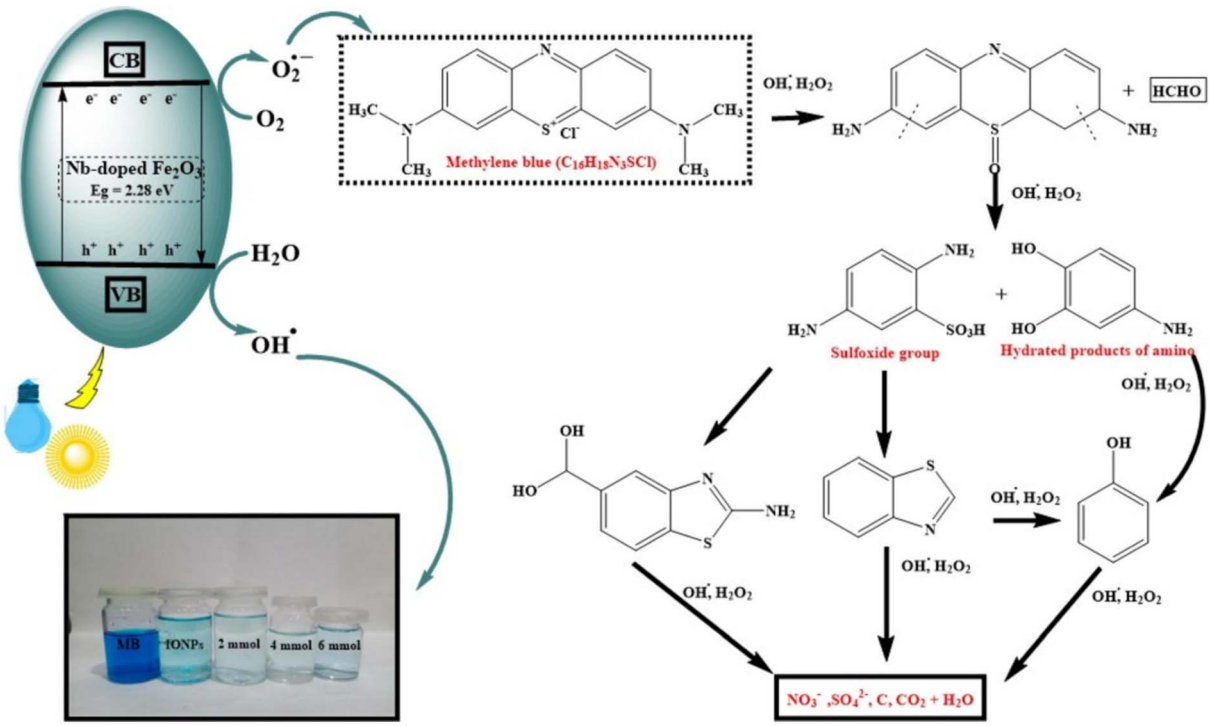

Fig. 12 Mechanism of photodegradation using Nb-doped Fe_2O_3.[198] "Reproduced from ref. 198 with permission from [Elsevier], copyright [2025]."

 © 2025 The Author(s). Published by the Royal Society of Chemistry

Open Access Article. Published on 02 September 2025. Downloaded on 11/10/2025 5:56:01 AM. This article is licensed under a Creative Commons Attribution-NonCommercial 3.0 Unported Licence.

90% of MG dye in the same duration. The degradation rate increased with Y doping concentration up to 6 wt%, but declined at higher levels. The enhanced performance is attributed to the generation of electron–hole pairs under visible light, with Y doping introducing intermediate energy levels within the band gap of WO_3.[204] These states extend light absorption into the visible region and promote better charge separation, thereby improving the photocatalytic activity. Under visible light irradiation, electrons are excited to the conduction band of WO_3, where Y^{3+} ions serve as electron traps, capturing the electrons and being reduced to Y^{2+}. This trapping effect minimizes electron–hole recombination and prolongs the lifetime of charge carriers. The captured electrons then react with adsorbed O_2 molecules to produce superoxide radicals ($O_2^{\bullet-}$), while the holes remaining in the valence band oxidize water molecules or hydroxide ions to generate hydroxyl radicals ($^{\bullet}OH$). These reactive oxygen species ($^{\bullet}OH$ and $O_2^{\bullet-}$) play a key role in attacking and decomposing MG dye molecules into less toxic products.[204]

7.6. Copper oxide

Copper oxide nanoparticles exhibit excellent optical absorption characteristics and an ideal optical bandgap. Their cost-effective production is facilitated by the abundance of precursor materials in the earth's crust.[205,206] Copper nanoparticles are applicable in catalyzing the reduction of CO_2 and its conversion into specific products. Additionally, they have been employed as plasmonic photocatalysts, which enable chemical transformations and the breakdown of toxic organic pollutants into simpler, non-toxic compounds such as water and CO_2.[207] It comprises two semiconductor phases: cupric oxide (CuO) having a lower optical band gap (1.6 eV) than the other phase, cuprous oxide (Cu_2O), with a higher optical bandgap of approximately 2.4 eV. Cu_2O, characterized by a 2.4 eV bandgap, is a p-type-based metal oxide semiconductor.[208] Because of its optimal bandgap for photocatalysis, visible light is preferred for such activities. Muthukumaran *et al.* utilized the sonochemical method to synthesize cuprous oxide (Cu_2O) nanoparticles as a photocatalyst for degrading malachite green under visible light.[205] Following 45 minutes of exposure, the fabricated nanoparticles achieved a degradation rate of 91.89%.[205] Kerour *et al.* employed a green method utilizing aloevera leaf extracts to synthesize Cu_2O nanoparticles for degrading methylene blue dye.[209] Remarkably, they found that the dye completely degraded after 10 minutes of exposure to visible light.[209] Despite these benefits, Cu_2O faces several challenges as a photocatalyst due to its narrow bandgap and short minority-carrier diffusion length, which lead to a high recombination rate of photoinduced electrons and holes. Additionally, stability issues caused by self-reduction from photogenerated electrons and self-oxidation from holes result in severe photocorrosion. This photocorrosion is believed to hinder its photocatalytic activity by blocking light from reaching the surface and degrading the structural integrity of the material, thereby limiting its practical applications in photocatalysis.[210] However, numerous efforts have been made to implement effective strategies for enhancing the photostability and photocatalytic performance of Cu_2O. In general, most research focuses on improving charge transfer from Cu_2O to reactants or co-catalysts to prevent charge accumulation within the particles. Common approaches include morphology control, particle size tuning, optimization of reaction conditions, and the formation of composites with other materials.

On the other hand, CuO nanoparticles have attracted substantial attention in areas such as photocatalysis, supercapacitors, solar cells, electrocatalysis, biodiesel production, and water pollution remediation.[211,212] However, the photocatalytic performance of CuO has been found to be superior to that of Cu_2O.[213] Similar to Cu_2O, CuO is also limited by rapid photoinduced recombination and photocorrosion. Therefore, to mitigate these problems, several innovative approaches have been developed by researchers.[214] Among them, integrating CuO with carbon-based materials has garnered considerable attention due to enhanced electron transport and surface area.[215] Additionally, coupling CuO with other metal oxide semiconductors has proven effective in boosting its photocatalytic activity. For example, Sakib *et al.* synthesized a CuO/ZnO composite, which demonstrated a remarkable 98% degradation of methylene blue (MB) dye within 120 minutes under sunlight.[216] The formation of p–n junction heterostructures not only broadens the light absorption range but also suppresses the rapid recombination of photogenerated electron–hole pairs.[217] Furthermore, metal doping has emerged as a promising approach to further enhance the photocatalytic performance of CuO nanoparticles.[218] Despite the improvement of photocatalytic performance of CuO by these methods, fabrication of CuO with carbon-based materials, heterojunction formation, and metal doping in a single material could further enhance light absorption, promote charge separation, and improve overall stability simultaneously.

7.7. Bismuth oxide

Bismuth oxide (Bi_2O_3) can be found in a variety of crystal forms, including triclinic, orthorhombic, face-centered cubic, body-centered cubic, monoclinic, tetragonal, and hexagonal structures.[219] Bi_2O_3 demonstrates outstanding photocatalytic performance in wastewater treatment, CO_2 reduction, and water splitting when exposed to visible light. However, its photocatalytic efficiency is significantly diminished by the high recombination rate of electron–hole pairs, which impairs its ability to degrade organic pollutants.[220] To enhance the overall photocatalytic efficiency of Bi_2O_3, several approaches have been developed, including modifying its surface structure, morphology, shape, and microstructure, implementing interface engineering, combining other materials, creating oxygen vacancies, and doping with metals and nonmetals.

7.8. Other oxides

Apart from the above-mentioned metal oxides, other oxides such as CeO_2, ZrO_2, MgO, *etc.*, and spinel-type oxides such as Co_3O_4, $NiWO_4$, *etc.*, also exhibit limited efficiency in pollutant degradation. In light of these constraints, spinal ferrites

Open Access Article. Published on 02 September 2025. Downloaded on 11/10/2025 5:56:01 AM.
This article is licensed under a Creative Commons Attribution-NonCommercial 3.0 Unported Licence.

(MFe_2O_4, where M is a divalent metal ion) have emerged as compelling alternatives. These materials not only exhibit excellent thermal and chemical stability,[221–223] but also features a spinel crystal structure that provides additional catalytic sites, thereby enhancing their photocatalytic performance.[224] Additionally, their narrow band gap (typically ≤2 eV), enables strong absorption in the visible light region, making them promising candidates for visible-light driven photocatalytic applications. It is also noteworthy that ferrites possess smaller band gaps compared to other commonly used visible-light photocatalysts such as WO_3 (2.8 eV) or $AgVO_3$ (2.2 eV). This narrower band gap enhances their ability to absorb visible light more effectively, offering a potential advantage over photocatalysts with wider band gaps that cover both UV and visible regions but may exhibit lower overall efficiency under visible-light irradiation.[225] The application of ferrites in the photocatalytic degradation of organic pollutants holds great promise for environmental remediation. Few materials can efficiently facilitate both photo-oxidation and photo-reduction processes essential for the complete breakdown of hazardous organic compounds, while also exhibiting strong visible light absorption. To overcome these limitations, composite photocatalysts comprising two or more components have been widely investigated, often resulting in significantly enhanced photocatalytic activity.[226] Another notable advantage of ferrites lies in their inherent magnetic properties. Due to the high magnetism of iron(III) oxides, ferrite-based photocatalysts, either used alone or in composites, can be easily separated from reaction mixtures using an external magnetic field.[227] Moreover, spinel ferrites and their nanocomposites, especially those integrated with carbon-based materials, exhibit excellent photocatalytic activity for contaminant degradation. These systems effectively generate reactive radicals under both visible and UV light, presenting a cost-effective and efficient approach for water purification.[228] Despite their advantages, ferrites with narrow band gaps often suffer from rapid recombination of photogenerated charge carriers, which limits their overall photocatalytic efficiency. However, strategies such as metal doping and the formation of composites with other materials have proven effective in enhancing their performance.[228] For example, Cao *et al.* synthesized Ag-doped $ZnFe_2O_4$ *via* a reflux method and evaluated its photocatalytic activity against Rhodamine B (RhB) dye.[229] They observed that the degradation efficiency of the undoped $ZnFe_2O_4$ was significantly lower than that of its Ag-doped counterpart. The enhanced activity was attributed to improved charge separation and more efficient charge transfer to the reactant molecules.[229]

8. Enhancement of photocatalytic activity

The effectiveness of a photocatalyst's photocatalytic activity heavily relies on its light absorption capability, crystal quality, morphology, surface composition, and electronic attributes. Despite this, its widespread application in environmental micro-scale systems is hindered by persistent barriers such as the high expense of semiconductor materials, inefficient harnessing of solar energy, and rapid recombination of charge carriers.[230] Additional challenges include stability, photocorrosion, and availability.[210] The primary challenge for photocatalytic performance is linked to the properties of metal oxide, such as insufficient overlap between their band gap with available light of the electromagnetic spectrum, structural degradation, and ineffective charge separation and mobility.[214] The bandgap of a photocatalyst determines its incident photon absorption efficiency, and most known photocatalysts have a wide bandgap, limiting their activity to the UV region of the electromagnetic spectrum. Therefore, tailoring the bandgap is a crucial challenge to overcome. Furthermore, the recombination of photoinduced electron–hole pairs is a major challenge that affecting the photocatalytic performance of catalyst.[231] To address these shortcomings, extensive research has been conducted to enhance solar energy utilization efficiency. Several approaches have recently been proposed to improve adsorption capacity and photocatalytic activity.[232] Fig. 13 represents the different strategies that have been applied to enhance the photocatalytic activity of a semiconductor photocatalyst under visible/solar illumination.

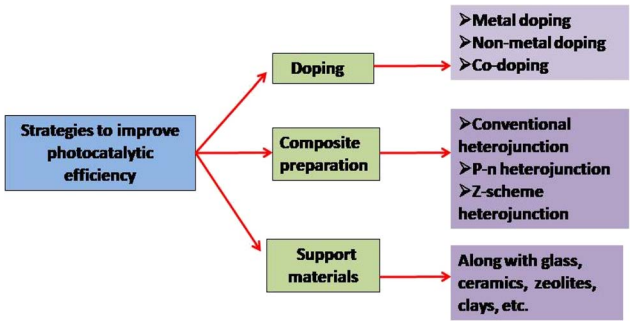

Fig. 13 Schematic representation showing several approaches to enhance the effectiveness of metal-oxide photocatalysts.

8.1. Doping with metals and non-metals

The use of metal-doped photocatalysts to degrade various organic contaminants under visible light irradiation has been thoroughly investigated.[233,234] Metal-oxide particles can be substitutable or interstitially doped with various cations. However, the literature contains numerous inconsistent findings because the doping process (*e.g.*, impregnation, co-precipitation, and sol–gel methods) leads to photocatalysts with varying morphological and crystalline characteristics.[235,236] This method has several drawbacks, including the thermal instability of doped metal oxides, high costs, and the need for expensive ion-implantation equipment.[32] Non-metal dopants like C, N, S, B, P, F, and I may be more effective for enhancing photocatalytic activity in the visible range because their impurity states are close to the valence band edge. However, they do not serve as charge carriers and may have a reduced ability to act as recombination centers.[237] Metal-ion-doped TiO_2 is extensively investigated to expand its absorption spectrum into visible light. This is beneficial as visible light is readily available

 © 2025 The Author(s). Published by the Royal Society of Chemistry

Open Access Article. Published on 02 September 2025. Downloaded on 11/10/2025 5:56:01 AM.
This article is licensed under a Creative Commons Attribution-NonCommercial 3.0 Unported Licence.

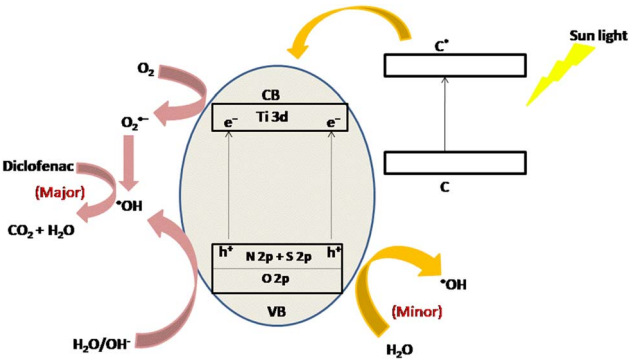

Fig. 14 Diagram showing how C–S–N-tri doped TiO_2 photocatalyst increases photoactivity.[246] "Reproduced from ref. 246 with permission from [Elsevier], copyright [2017]."

in the solar spectrum. For instance, to boost UV-driven photocatalytic degradation of ATP, Sakaguchi *et al.* employed the sol–gel technique to incorporate lutetium(III) ions into TiO_2.[238] Their results demonstrated that the doped TiO_2 showed higher reactivity than the undoped counterparts, primarily due to the presence of labile Ti^{3+} spots on the surface, which were formed by doping Lu^{3+} ions into the TiO_2 structure. In other words, the Lu^{3+} ions played a key role in generating different types of Ti^{3+} sites on the powder's surface, which led to an increased recombination time of the electron–hole pairs compared to pure TiO_2.[238] Similarly, Ndabankulu *et al.* explored TiO_2 doped with different lanthanides (Ce, Dy, Lu, and Sm) *via* the sol–gel method.[239] They examined the photocatalytic activity and efficacy of these lanthanide-doped TiO_2 samples for degrading caffeine under visible light irradiation.[239] Sood *et al.* incorporated Fe^{3+} in TiO_2 through a hydrothermal synthesis route and evaluated their photocatalytic potential under visible light using *para*-nitrophenol as a representative contaminant.[240] With just 0.05 mol% Fe^{3+}, the system achieved up to 92% degradation in 5 hours. The improved activity was credited to enhanced crystallinity, reduced particle dimensions, better charge carrier dynamics, suppressed electron–hole recombination, and increased sensitivity to visible light introduced by Fe^{3+} incorporation.[240] Nonmetal components were also introduced into TiO_2 photocatalysts to enhance the light absorption of metal oxides into the visible range.[32,241] In visible light, nitrogen-doped TiO_2 exhibited a remarkable degradation of lindane into benzene of up to 100%.[242,243] Under visible-light irradiation, N- and C-doped TiO_2 nanomaterials have demonstrated superior photocatalytic activity. The dual doping of two different atoms into metal oxides has attracted significant attention.[244] Yang and colleagues found that co-doping of monocrystalline TiO_2 with Eu^{3+} and Fe^{3+} yields a synergistic effect, significantly increasing the photocatalytic degradation of chloroform in solution.[245] Research teams have explored nonmetal co- and triple-doped TiO_2 to enhance its photocatalytic activity. For instance, Ramandi *et al.* utilized the sonochemical method to synthesize anatase phase TiO_2 doped with carbon, nitrogen, and sulfur.[246] They then investigated the photocatalytic efficiency of the catalyst against diclofenac as a representative contaminant and sunlight as the light source.[246] The mechanism of photocatalytic degradation for the C–N–S triple-doped TiO_2 is depicted in Fig. 14.[246] Each nonmetal doping plays a critical role in boosting the photocatalytic performance of TiO_2 by introducing additional impurity states such as N 2p, S 2p, and C 1s. Carbon doping, in particular, acts as a photosensitizer that facilitates the injection of electrons into the CB when exposed to sunlight. In contrast, N and S doping alters the electronic band structure of TiO_2 by mixing the O 2p orbitals of TiO_2 with N 2p and S 2p orbitals, leading to a narrower bandgap for TiO_2. The report suggests that both electrons in the CB and trapped electrons participate in activating O_2 adsorbed on the surface, producing reactive $O_2^{\bullet-}$. Among the generated species, electrons and $^{\bullet}OH$ radicals are identified as the dominant oxidants responsible for degrading diclofenac, whereas photo-induced holes contribute minimally. $O_2^{\bullet-}$ has a significant

Table 4 Overview of TiO_2-based photocatalysts used in the photo breakdown of organic contaminants

Catalysts	Procedure for synthesis	Prototype pollutant	Light	Time (min)	Degradation efficiency (%)	Ref.
TiO_2	*In situ* complexation hydrolysis	MB	Ultraviolet	40	~100	247
TiO_2	Hydrothermal	Ofloxacin	Visible light	60	98	248
Pd-TiO_2	Photodeposition	BDE-15	Ultraviolet	20	100	249
Pd-TiO_2	Photodeposition	BDE-209	Ultraviolet	<60	100	249
Ag-TiO_2	UV-assisted photocatalytic reduction	BDE-47	Ultraviolet	13	100	250
Pt-TiO_2	Photocatalytic reduction method	BDE-47	Ultraviolet	40	>90	251
Cu-TiO_2	Photocatalytic reduction method	BDE-47	Ultraviolet	30	>90	251
Fe^{3+}-doped TiO_2	Hydrothermal	*Para*-nitrophenol	Visible light	300	92	240
Se^{4+}-doped TiO_2	Sol–gel	RhB	Visible light	30	91.3	252
Zn-doped TiO_2	Sol–gel	MB	Visible light	60	99.64	253
Mo- and W-doped TiO_2	Sol–gel	RhB	Visible light	60	96	254
Ce-doped TiO_2	Sol–gel	Caffeine	Visible light	120	—	239
Iodine-doped TiO_2	Combustion process	Direct blue 199	Visible light	—	—	255
C–S–N-tri doped TiO_2	Sonochemical process	Diclofenac	Solar light	180	100	246

Open Access Article. Published on 02 September 2025. Downloaded on 11/10/2025 5:56:01 AM.
This article is licensed under a Creative Commons Attribution-NonCommercial 3.0 Unported Licence.

impact on diclofenac degradation.[246] The ˙OH radicals can be generated in two distinct ways:

$$O_2 + e^- \rightarrow O_2^{\cdot -} \quad (9)$$

$$O_2^{\cdot -} + 2H_2O \rightarrow 2^{\cdot}OH + 2OH^- + O_2 \quad (10)$$

$$h^+ + H_2O \rightarrow {}^{\cdot}OH \quad (11)$$

Eqn (9) demonstrates the reaction between molecular O_2 and electrons (e^-) in the CB, resulting in the production of $O_2^{\cdot -}$. Subsequently, in eqn (10), $O_2^{\cdot -}$ reacts with the molecules of H_2O to generate the species ˙OH radical. Conversely, eqn (11) illustrates that h^+ and H_2O can react on the photocatalyst surface to produce ˙OH radicals. Table 4 summarizes the degradation performance of organic pollutants using doped TiO_2-based nanomaterials.

Ji *et al.* synthesized ZnO doped individually with Fe^{3+}, Sn^{4+}, and codoped with both ions using a low-temperature solution based technique.[256] The photocatalytic efficiency of the resulting materials was assessed through the degradation of MB. Incorporating Fe^{3+} and Sn^{4+} into ZnO created an impurity level adjacent to the conduction band, enabling electrons in the valence band to transition with smaller energy, as illustrated in Fig. 15.[256] As a result, there was an increase in the concentrations of photoinduced electrons and holes, enhancing the photocatalytic performance of doped ZnO nanoparticles. Alam *et al.* synthesized ZnO nanoparticles doped with metals from the lanthanide series (La, Nd, Sm, and Dy) using the sol–gel technique and tested the photocatalytic degradation of MB and RhB.[257] The improved performance of the photocatalyst was attributed to the doping with these heavy metals.[257] Nonmetal-doped ZnO photocatalysts have also been reported enhanced photocatalytic activity under visible light irradiation. Mirzaeifard *et al.* utilized the hydrothermal method for the synthesis of sulfur-doped ZnO. RhB was used to evaluate the photodegradation efficiency of the synthesized photocatalyst under visible light irradiation.[258] They determined the optimal catalyst dosage for maximizing the degradation of rhodamine B.[258] Out of those, the photocatalyst with 0.10 g and 0.5 wt% of sulfur achieved a 100% degradation rate of RhB (5 ppm) at pH = 5 within 90 minutes. Table 5 summarizes the degradation performance of organic pollutants using doped ZnO-based nanomaterials.

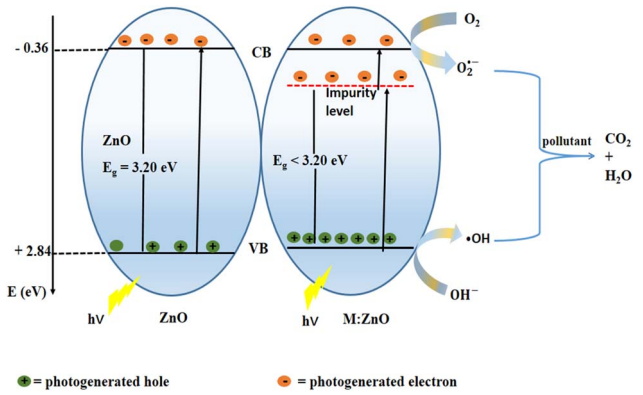

Fig. 15 Diagram showing the introduction of impurities in ZnO photocatalysis.[256] "Reproduced from ref. 256 with permission from [John Wiley and Sons], copyright [2019]."

Similarly, metal doping can reduce the band gap and impede rapid charge recombination in WO_3 photocatalysts. Ramkumar and Rajarajan fabricated WO_3 thin films incorporated with Ni *via* the chemical bath deposition technique and examined their photocatalytic activity through the degradation of MO, MB, and phenol.[261] The addition of Ni to WO_3 greatly enhanced its photocatalytic activity. Desseigne *et al.* fabricated 5 wt% Au-loaded WO_3 *via* a room temperature impregnation–reduction method.[262] The introduction of Au significantly narrowed the band gap of WO_3 to 2.54 eV. The photocatalytic performance of Au/WO_3 was assessed under simulated solar irradiation against RhB, MB, and MO. Complete degradation of RhB was achieved in 90 minutes in the presence of Au/WO_3, while pristine WO_3 showed only 5% degradation. For MO, Au/WO_3 achieved 50% degradation after 180 minutes, whereas WO_3 showed negligible activity. In the case of MB, Au/WO_3 90% degradation compared to 80% with WO_3 after the same duration.[262] Han *et al.* fabricated S-doped WO_3 nanowires through a hydrothermal synthesis followed by thermal treatment at 300 °C, effectively tuning the electronic structure to reduce the band gap to 2.52 eV.[263] The presence of S not only broadened visible light absorption but also facilitated efficient charge carrier separation. As a result, S-WO_3 nanowires achieved an impressive 97% degradation of MO under 3 h of visible light exposure. This pronounced photocatalytic response was primarily driven by the synergistic effects of S doping on optical and electronic properties.[263] Table 6 summarizes the degradation performance of organic pollutants using doped WO_3-based nanomaterials.

Table 5 Overview of ZnO-based photocatalysts used in the photo breakdown of organic contaminants

Catalysts	Procedure for synthesis	Morphology	Prototype pollutant	Light	Time (min)	Degradation efficiency (%)	Ref.
ZnO	Precipitation	NP	Phenol	UV	120	100	259
$Sn_{0.05}ZnO$	Low-temperature solution	NP	MB	UV	120	99.61	256
Nd-doped ZnO	Sol–gel	NP	MB	UV	25	98	257
Cu-doped ZnO	Solvothermal	NP	MB	Simulated sunlight	120	81	260
Sulfur-doped ZnO	Hydrothermal	NP	RhB	Visible light	90	100	258

 © 2025 The Author(s). Published by the Royal Society of Chemistry

Open Access Article. Published on 02 September 2025. Downloaded on 11/10/2025 5:56:01 AM.
This article is licensed under a Creative Commons Attribution-NonCommercial 3.0 Unported Licence.

Table 6 Overview of WO_3-based photocatalysts used in the photo breakdown of organic contaminants

Catalysts	Procedure for synthesis	Morphology	Prototype pollutant	Light	Time (min)	Degradation efficiency (%)	Ref.
Au-doped WO_3	Impregnation–reduction method	Platelet	RhB	Simulated solar light	180	100	262
Au-doped WO_3	Impregnation–reduction method	Platelet	MB	Simulated solar light	180	90	262
Au-doped WO_3	Impregnation–reduction method	Platelet	MO	Simulated solar light	180	50	262
S-doped WO_3	Hydrothermal	Nanowire	MO	Visible light	180	97	263
Pt-doped WO_3	Photochemical impregnation	NP	MO	230 W tungsten-halogen lamp	180	80	264
Pt-doped WO_3	Spray deposition method	Pillar structure	MB	Sunlight	360	97	265
Ni-doped WO_3	Chemical bath deposition	Thin film	MO	Visible light	150	88	261
Ni-doped WO_3	Chemical bath deposition	Thin film	MB	Visible light	150	85	261

Table 7 Overview of CuO-based photocatalysts used in the photo breakdown of organic contaminants

Catalysts	Procedure for synthesis	Morphology	Prototype pollutant	Light	Time (min)	Degradation efficiency (%)	Ref.
Ce-doped CuO	Solution combustion method	NPs	RhB	Sunlight	40	95.39	267
Ce-doped CuO	Solution combustion method	NPs	MB	Sunlight	40	87.72	267
Tb-doped CuO	Solution combustion method	NPs	MB	Visible light	120	94	268
Co-doped CuO	One-pot green synthetic route	Spherical dopants on rod-like morphology	MB	UV-vis light irradiation	100	88	269
Mn-doped CuO	Hydrothermal method	Nanosheet	MB	UV-vis light	200	87	270
Cd, Ba-codoped CuO	Co-precipitation	Platelet-like aggregates	CR	Visible light	180	98	271

Li *et al.* produced Fe_2O_3 nanoparticles doped with various metals, starting from fabric filter dust, to degrade methyl orange.[193] These metal-doped variants exhibited an 82.99% degradation rate under visible light, compared to only 38.94% for undoped Fe_2O_3.[193] Saikala *et al.* synthesized Ce-doped CuO photocatalyst using a straightforward precipitation followed by thermal decomposition approach.[266] The photocatalytic efficiency of the material was evaluated against azo dyes like MO and Trypan Blue (TB) under UV light irradiation. Remarkably, Ce/CuO exhibited nearly complete degradation of both dyes within 300 minutes. The Ce/CuO photocatalyst exhibited superior dye degradation efficiency under UV illumination compared to both bare and commercial CuO. This enhanced performance was attributed to the presence of Ce atoms, which acted as electron traps in the CB, thereby promoting effective separation of photogenerated e^-/h^+ pairs and suppressing recombination.[266] Table 7 summarizes the degradation performance of organic pollutants using doped CuO-based nanomaterials.

8.2. Formation of heterojunctions

A heterojunction is the boundary where semiconductors with different band structures meet, resulting in various possible band alignments.[272,273] There are three fundamental types of semiconductor-based heterojunctions: conventional heterojunction photocatalysts, p–n, and Z-scheme heterojunction photocatalysts.

8.2.1. Conventional heterojunction photocatalysts. Heterojunction photocatalysts of these classes are mainly divided into- type-I, type-II, and type-III, as shown in Fig. 16.[274] For a type-I heterojunction photocatalyst (see Fig. 16a), semiconductor A has a higher CB, while VB is lower compared to semiconductor B.[275] Hence, under light exposure, electrons and holes gather at the CB and VB levels of semiconductor B, respectively. Because both charge carriers are concentrated in the same semiconductor, the separation of electron–hole pairs is effectively impeded in the type-I heterojunction photocatalyst. Additionally, a redox reaction occurs predominantly on the semiconductor having lower redox potential, drastically reducing the net redox capability of the heterojunction photocatalyst.[276] In type-II heterojunction photocatalyst (depicted in Fig. 16b), semiconductor A has higher CB and VB levels than semiconductor B. As a result, photoinduced electrons will migrate to semiconductor B, while photoinduced holes will move to semiconductor A upon exposure to light, thereby achieving spatial separation of electron–hole pairs.[277,278] Similar to type-I heterojunction, the redox capability of the type-II heterojunction photocatalyst will also diminish, as the reduction and oxidation reactions occur on semiconductor B, having lower reduction potential, and semiconductor A, having lower oxidation potential, respectively. The configuration of the type-III heterojunction photocatalyst depicted in Fig. 16c closely resembles that of the type-II heterojunction. However, it features an intensified staggered gap, ensuring no overlap

Open Access Article. Published on 02 September 2025. Downloaded on 11/10/2025 5:56:01 AM.
This article is licensed under a Creative Commons Attribution-NonCommercial 3.0 Unported Licence.

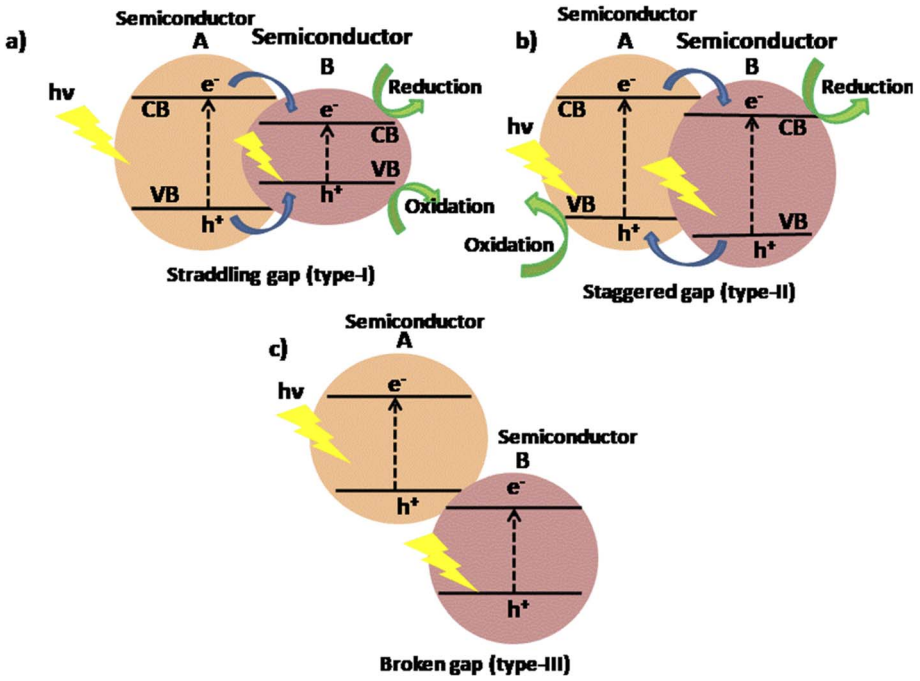

Fig. 16 Diagram showing the separation of electron–hole pair in three types of conventional heterojunction photocatalysts: (a) type-I, (b) type-II, and (c) type-III.[274]

between the bandgaps.[279,280] This hindered electron–hole migration and separation between the two semiconductors in the type-III heterojunction, making it ineffective for enhancing electron–hole pair separation under visible light irradiation. Among the heterojunctions mentioned earlier, it's clear that the type-II heterojunction is the most feasible for increasing photocatalytic performance due to its structure, which facilitates the spatial separation of electron–hole pairs.

Metal oxide-based heterojunctions have been extensively researched, with TiO_2 being the first and most thoroughly studied photocatalyst. TiO_2 possesses many benefits, but its wide bandgap energy (3.2 eV *vs.* NHE) limits its absorption of ultraviolet light. It is a primary semiconductor for developing type-II heterojunction photocatalytic systems.[281] In the early 2000s, Bessekhouad *et al.* explored Bi_2S_3/TiO_2 and CdS/TiO_2 heterojunctions for the visible light-induced degradation of Orange II.[282] Because the wide bandgap of TiO_2 prevents excitation by visible light, the prepared composites of TiO_2 significantly improved light utilization. Specifically, CdS/TiO_2 degrades at a pace of 30 minutes, which is significantly faster than pure CdS and TiO_2 rates alone. Mugunthan *et al.* reported on the photocatalytic degradation of diclofenac in wastewater in the presence of composite $ZnO\text{-}WO_3$ semiconductor photocatalyst hydrothermally prepared and activated by visible light.[283] This composite expanded the optical response into the visible range and exhibited improved stability, consistently achieving 80% degradation efficiency.

Leghari *et al.* employed a hydrothermal reaction method to synthesize a WO_3/TiO_2 nanocomposite.[284] Their study revealed that organic compounds degraded according to the Langmuir–Hinshelwood isotherm. Notably, the 5.0% composite demonstrated superior photoactivity compared to pure TiO_2, P-25, and pure WO_3 when degrading MO and 2,4-DCP under both UV and visible light conditions.[284] Similarly, under visible light exposure, $Fe_2O_3\text{-}WO_3$ nano-composite heterostructure demonstrated a significant increase in the photo-degradation of RhB.[285]

8.2.2. p–n heterojunctions. While the type-II heterojunction may efficiently separate electron–hole pairs in space, the resulting enhancement in electron–hole separation is inadequate to overcome the semiconductor's rapid electron–hole recombination. Hence, a concept of p–n heterojunction photocatalyst was introduced to expedite electron–hole migration across the heterojunction, thereby boosting photocatalytic performance with the aid of an additional electric field.[286,287] To create a p–n heterojunction photocatalyst, p-type and n-type semiconductors are combined. The n-type semiconductor's electron close to the p–n interface tends to diffuse into the p-type semiconductor before being exposed to light, generating a positively charged species (Fig. 17).[288–290] At the same time, a negatively charged species is produced with the diffusion of holes from the p-type semiconductor close to the p–n interface into the n-type semiconductor. As long as the system doesn't attain equilibrium at the Fermi level, electron–hole pairs will continue to diffuse. This causes the region around the p–n interface to become charged, forming a "charged" space, or what is commonly referred to as the internal electric field.[291,292] When exposed to light having energy equal to or greater than the respective bandgap values, both the p-type and n-type semiconductors become excited, resulting in electron–hole pairs. These photoinduced electrons and holes in the p-type and n-type semiconductors move under the influence of internal

 © 2025 The Author(s). Published by the Royal Society of Chemistry

Open Access Article. Published on 02 September 2025. Downloaded on 11/10/2025 5:56:01 AM.
This article is licensed under a Creative Commons Attribution-NonCommercial 3.0 Unported Licence.

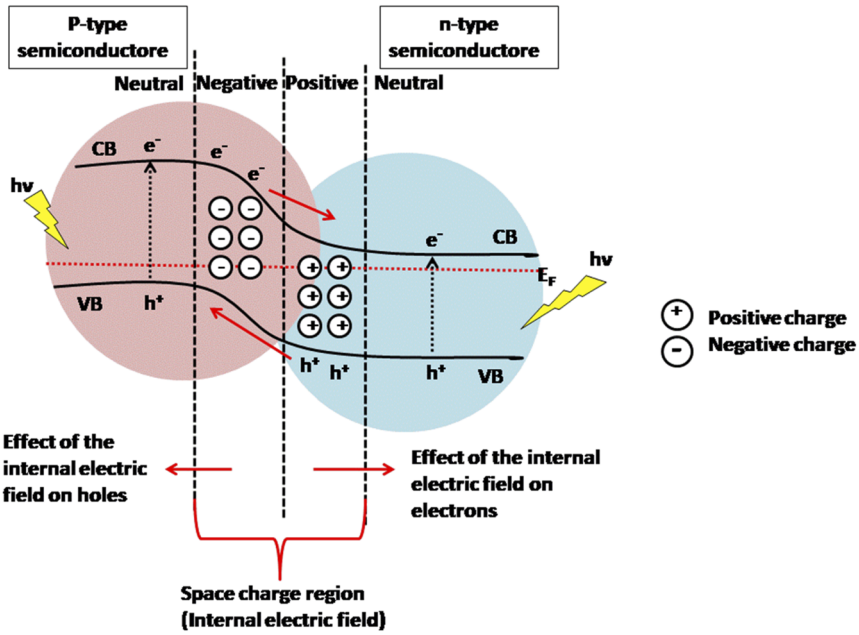

Fig. 17 Diagram showing electron–hole separation under light exposure in a p–n heterojunction photocatalyst.[288]

electric field (IEF) to the CB of the n-type semiconductor and the VB of the p-type semiconductor, respectively, thereby spatially separating the electron–hole pairs. Importantly, this separation procedure is thermodynamically viable because, in a p–n heterojunction photocatalyst, the p-type semiconductor's CB and VB are usually positioned higher than the n-type semiconductor.[293,294] Because of the combined effect of the internal electric field and band alignment synergy, p–n heterojunction photocatalysts have an accelerated electron–hole separation efficiency compared to type-II photocatalysts.[295]

Chen *et al.* synthesized p-type NiO and n-type TiO_2 *via* the incipient wetness impregnation method.[296] They assessed their photocatalytic activity by studying the breakdown of MB. The results indicated that the highest activity was observed with 0.5 wt% NiO/TiO_2 compared to TiO_2 alone. This improvement in photocatalytic performance is ascribed to the synergistic effects of the p–n junction and co-catalyst mechanisms.[296]

Under visible light exposure, the p–n type CuO-TiO_2 semiconductor supported on natural zeolite demonstrated remarkable photocatalytic efficacy in degrading azo dyes. In particular, the semiconductor with zeolite achieved a 90% degradation of MB dye within 60 minutes, exceeding the performance of zeolite alone (79.1%), TiO_2-zeolite (84.1%), and CuO-zeolite (85.2%) under identical conditions.[297] According to Nguyen and Doong, the solvothermal preparation of a binary p–n semiconducting $ZnFe_2O_4/TiO_2$ nanocomposite, which has a $ZnFe_2O_4$ weight ratio of 1%, makes it a very effective photocatalyst for the breakdown of BPA in an aqueous environment when exposed to 465 nm visible-light.[298] Table 8 summarizes the degradation performance of organic pollutants using heterostructured photocatalyst.

8.2.3. Z-scheme heterojunction photocatalysts. Depending on whether a mediator of the electron is present, a Z-scheme photocatalytic system can be classified as direct or indirect. The components of a Z-scheme heterojunction photocatalyst are a reduction semiconductor having a high CB position (SC II), and an oxidation semiconductor with a low VB position (SC I). An electron mediator is occasionally included, resulting in an

Table 8 An overview of the heterostructured photocatalyst-based photocatalytic elimination of pollutants under visible light irradiation

Photocatalysts	Heterojunction type	Synthesis method	Pollutants	Time (min)	Degradation efficiency (%)	Ref.
TiO_2/SnO_2	Type-II	Electrospinning/hydrothermal	RhB	60	100	299
CuO/TiO_2	Type-II	Impregnation technique	BDE-209	7.5	100	300
α-Fe_2O_3/CdS	Type-II	Hydrothermal/wet chemical	MB	120	86.7	301
$ZnTiO_3$/BiOI	p–n	Precipitation–deposition	Rh 6G	180	>80	302
$In_2S_3/InVO_4$	Type-II	*In situ* anion exchange	TC	60	71.4	303
$BiVO_4$/BiOBr	p–n	Hydrothermal	NFX	60	90	304
BiOBr/$FeWO_4$	Type-II	Solvothermal	Doxycycline	60	90.4	305
BiOBr/Fe_3O_4	p–n	Solvothermal	GP	60	97	306

Open Access Article. Published on 02 September 2025. Downloaded on 11/10/2025 5:56:01 AM.
This article is licensed under a Creative Commons Attribution-NonCommercial 3.0 Unported Licence.

indirect Z-scheme photocatalyst. Bard *et al.* introduced the idea of the Z-scheme heterojunction in 1979, inspired by the mechanism of plant photosynthesis.[307] The Z-scheme heterojunction was initially utilized in liquid-phase photocatalytic reactions. The redox mediator in the liquid phase acts as an acceptor–donor pair at the interface between the semiconductors without significant direct contact. As depicted in Fig. 18a,[308] during light exposure, the redox mediator facilitates the transfer of photoinduced electrons from the CB of SC I to the VB of SC II by functions both as an acceptor and a donor.

Consequently, with photoinduced holes accumulating in the VB of SC I and electrons aggregating in the CB of SC II, oxidation and reduction reactions can occur effectively within this heterojunction system.[276] Some commonly used redox electron mediators are Fe^{3+}/Fe^{2+} and IO_3^-/I^- pairs.[309] Nevertheless, this system faces several challenges. For instance, conventional Z-scheme photocatalysts typically operate in the liquid phase, requiring precise pH control of the reaction environment. Moreover, they often exhibit slow charge transfer rates, which hinder their practical application in contaminant degradation. Additionally, many liquid-phase redox mediators are unstable and prone to deactivation, leading to reduced overall photocatalytic efficiency.[309]

Considering the limitations of liquid-phase Z-scheme heterojunction photocatalysts, efforts have been directed toward finding alternatives to enhance the effectiveness of indirect Z-scheme heterojunction systems. In 2006, a novel approach involving an electron solid conductor was proposed to facilitate the transport of photoinduced electrons and holes. This innovative Z-scheme photocatalyst utilized noble metal Au as a electron mediator rather than traditional redox couples and integrated both the semiconductors, CdS and TiO_2. This advancement introduced the idea of all-solid-state (ASS) Z-scheme photocatalysts.[310] In this system, when illuminated with light energy surpassing the bandgaps of the semiconductors, electrons in SC II are excited from the VB to the CB, creating holes in the VB. These electrons are then transported to the VB of SC I *via* conducting materials at the semiconductor interface (Fig. 18b).[308] This mechanism ensures the preservation of redox capability and the effective separation of photogenerated carriers.[311] Numerous studies have identified noble metals as excellent mediators of electrons for constructing ASS Z-scheme photocatalysts. Alternative options, such as graphene, carbon nanotubes, *etc.*, have also been explored.[312] Table 9 represents the overview of notable ASS Z-scheme photocatalysts.

However, ASS Z-scheme semiconductor photocatalysts utilize uncommon and expensive electron mediators, and most result in the shielding effect, which significantly limits their long-term practical application.[281]

Studies on the direct Z-scheme photocatalyst were explored seven years after the ASS Z-scheme heterojunction photocatalyst was proposed.[324] In contrast to traditional liquid-phase and ASS Z-scheme heterostructures, direct Z-scheme photocatalysts feature two closely contacting semiconductors (Fig. 18c),[308] removing the requirement for an electron mediator. Notably, they combine the benefits of indirect Z-scheme heterojunctions, such as efficient electron–hole pair separation and optimum redox potential, while effectively reducing backward reactions and light shielding effects without mediators.[325–327] Moreover, eliminating mediators in direct Z-scheme systems significantly lowers construction expenditure, facilitating large-scale utilization. Additionally, developing an internal electric field at the interfaces of the direct Z-scheme system compensates for the role of mediators. This speeds up the recombination of light-

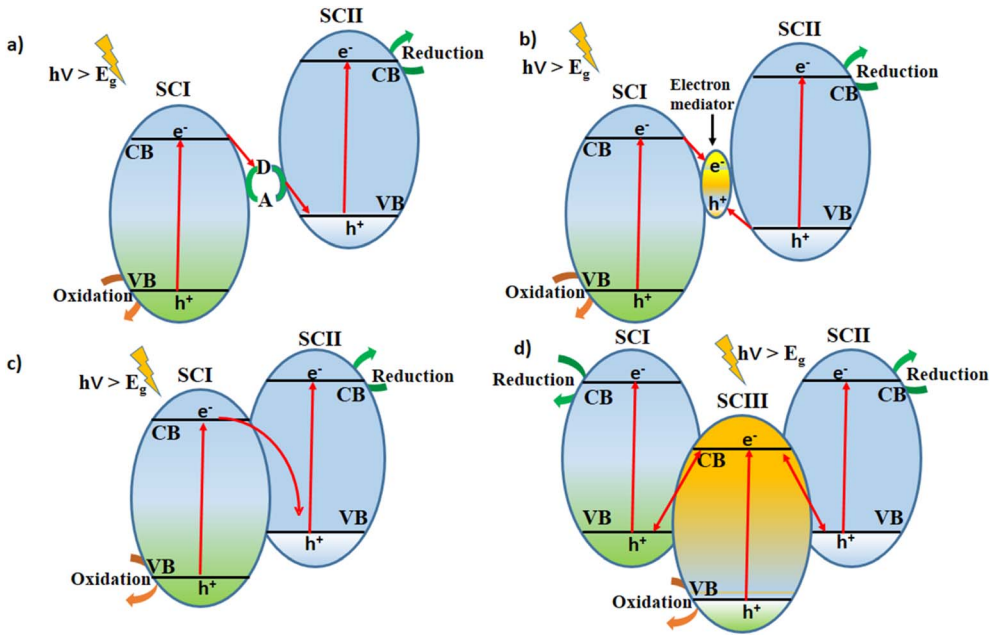

Fig. 18 A schematic overview of charge carrier migration in Z-scheme heterojunction photocatalysts when exposed to visible light: (a) conventional, (b) all-solid-state, (c) direct Z-scheme heterojunction, and (d) dual direct Z-scheme.[308]

 © 2025 The Author(s). Published by the Royal Society of Chemistry

Open Access Article. Published on 02 September 2025. Downloaded on 11/10/2025 5:56:01 AM.
This article is licensed under a Creative Commons Attribution-NonCommercial 3.0 Unported Licence.

Table 9 An overview of notable ASS Z-scheme photocatalysts

Catalyst	Mediator	Procedure for synthesis	Application	Ref.
$BiVO_4$/CDs/CdS	CDs	Deposition- precipitation	H_2 evolution rate: 1.24 μmol h^{-1} O_2 evolution rate: 0.61 μmol h^{-1}	313
$BiVO_4$/N-CQDs/Ag_3PO_4	N-CQDs	Solvothermal-precipitation	88.9% TC photodegradation in 30 min	314
AgBr/GO/Bi_2WO_6	GO	*In situ* deposition	Elimination of tetracycline hydrochloride with 84% photodegradation efficiency	315
g-C_3N_4/RGO/Bi_2WO_6	RGO	Hydrothermal	98% degradation of TCP	316
$BiVO_4$/MoS_2/RGO	RGO	Calcination	Water splitting	317
WO_3/g-C_3N_4/Bi_2O_3	g-C_3N_4	Cocalcination	80.2% degradation of TC	318
ZnO-Au-SnO_2	Au	Precipitation	Water splitting with photoconversion efficiency of 0.55%	319
$BiVO_4$-W-WO_3	W	Calcination	PEC performance: high photocurrent density of 5 mA cm^{-2}	320
Au-$CoFe_2O_4$/MoS_2	Au	Sol–gel and hydrothermal	∼96% MO degradation	321
Ag/Ag_3PO_4/WO_3	Ag	Deposition–precipitation process followed by photoreduction	98.7% RhB degradation	322
CdS/Ag/Bi_2MoO_6	Ag	Deposition–precipitation process	RhB degradation	323

induced charge carriers with weaker redox potentials, thereby preserving those with higher redox capabilities. Typically, the staggered band arrangement of two semiconductors results in an IEF only when both semiconductors have different work functions.[328,329] Specifically, free electrons of the semiconductor with a minor work function tend to move toward the other semiconductor upon contact in order to equalize their Fermi levels. Consequently, the electron-donating side becomes positively charged while the electron-accepting side becomes negatively charged, resulting in the development of IEF. Therefore, for the effective establishment of a direct Z-scheme photocatalyst, one semiconductor (SC II) should have higher CB and VB positions, as well as a reduced work function than the other semiconductor (SC I).[330] Table 10 represents the overview of notable direct Z-scheme photocatalysts.

Recently, dual/double Z-scheme heterojunction photocatalytic systems involving three semiconductors have garnered significant attention. These systems exhibit subtle variations in band alignments, pathways for charge transfer, and positions of redox reaction sites. In a regular double Z-scheme heterojunction configuration, electrons (or holes) from the intermediate semiconductor (SC III) dissipate as charge carriers migrate from nearby semiconductors. This leaves the peripheral semiconductors (SC I and SC II) with photoinduced charge carriers that participate in redox reactions. At the same time, the intermediate semiconductor also contributes to oxidation or reduction reactions (Fig. 18d).[308] In certain scenarios, both electrons and holes on the intermediate semiconductor are depleted, allowing only the photoinduced charge carriers on the peripheral semiconductors to take part in subsequent redox reactions.[340]

Despite the extensive study on heterojunction photocatalysts, achieving high efficiency remains a persistent challenge. Traditional type I/II and p–n heterojunctions face limitations such as inadequate suppression of photoinduced charge carrier recombination and slowly declining redox capabilities, which hinder their broader application. On the other hand, Z-scheme heterostructured photocatalysts attain efficient charge transfer and retain potent redox capabilities. However, due to the redox ion mediators, conventional Z-scheme photocatalysts suffer from reduced light absorption. In the case of ASS Z-scheme photocatalysts, the metal mediator is scarce and may

Table 10 An overview of notable direct Z-scheme photocatalysts

Catalyst	Procedure for synthesis	Application	Ref.
Ag_3PO_4/TiO_2	Hydrothermal and ultrasonic dispersion	100% degradation of RhB	331
CM-*n*-TiO_2	Ultrasonic sol–gel	100% degradation of aroclor	332
MoS_2/TiO_2	Hydrothermal or solvothermal	Photocatalytic degradation, hydrogen evolution, CO_2 reduction	333
TiO_2/(CdS, CdSe, CdSeS)	Chemical vapour deposition	Degradation of water dyes and antibiotics	334
RGO/$FeWO_4$-g-C_3N_4	Hydrothermal and mixing	92.3% degradation of RhB	335
g-C_3N_4/Ag_2WO_4	*In situ* precipitation	95% degradation of MO	308
g-C_3N_4/MnO_2	Wet-chemical	91.3% degradation of RhB	336
$LaFeO_3$/SnS_2	Hydrothermal process	28.8% degradation of tetracycline (TC)	337
ZnO/CeO_2	Wet chemistry process	96% RhB degradation	338
MoS_2/Bi_2O_3	Hydrothermal process	89.6% MBT degradation, 79.3% TC degradation, 90% RhB degradation	339

Open Access Article. Published on 02 September 2025. Downloaded on 11/10/2025 5:56:01 AM.
This article is licensed under a Creative Commons Attribution-NonCommercial 3.0 Unported Licence.

Table 11 Different substrates are used alongside metal oxides in photocatalytic systems

Catalyst	Substrate	Pollutant	Ref.
TiO_2	Quartz tubes	Amoxicillin	351
TiO_2	Cellulose	Phenol	352
TiO_2	Zeolites	Diclofenac (DCF)	353
WO_3	Glass	Benzoic acid	354
TiO_2/SnO_2	PVC, chitosan	1,2-Dichlorobenzene	355

compete for light absorption with semiconductors. Therefore, the most promising heterojunction systems accessible today are direct Z-scheme heterostructured photocatalysts.

8.3. Support materials for photocatalysis

In photocatalysis, a broad spectrum of both opaque and transparent supporting materials are utilized.[341] The photocatalyst support needs to be durable, keep the catalyst active, increase its surface area after immobilization, and effectively adsorb pollutants.[342]

Glass is an ideal medium commonly used as plates and beads for photocatalytic applications. It can endure high temperatures, offers good optical properties, and is cost-effective, making it a preferred choice for research.[343,344] Recent studies reveal that support materials containing carbon, particularly CNTs and rGO, are widely used. CNTs, with their cylindrical nanostructures, effectively lower the recombination rate of photoinduced electron–hole pairs.[345] Like glass, photocatalysts are often immobilized by clays, ceramics, and other silica-containing materials. Due to their large surface areas and chemical stability, they offer a practical and environmentally benign way to separate the catalyst from the reaction mixture and the effluents.[346] Other support materials include zeolites and numerous polymers such as polystyrene and polyaniline.[347–350] Table 11 presents several photocatalysts and their associated immobilization supports as documented in the literature.

9. Applications

9.1. Photodegradation of POPs

Persistent organic pollutants (POPs) are toxic, long-lasting chemicals that resist degradation.[356,357] They include a wide range of substances such as pesticides (OCPs, DDTs, aldrin, *etc.*), industrial chemicals (PCBs, PBDEs, HBCDs, PFASs, PFOS, SCCPs, HCB, HCHs), aromatic hydrocarbons, and by-products (dioxins, furans). They are mainly chlorinated, brominated, or fluorinated, contributing to their persistence and environmental risk.[27,358,359] To address their harmful effects, a variety of techniques-physical, chemical, biological, or hybrid methods have been proposed for their decomposition and mineralization. Among these, photocatalysis stands out as a promising and essential approach because of its high efficiency, energy-saving properties, mild reaction conditions, and minimal secondary pollution.[360]

For instance, in a study by Chen *et al.*,[361] TiO_2 and its Fe- and Cu-doped variants were synthesized *via* photodeposition and tested for PFOA degradation under UV light. The doping significantly enhanced photocatalytic performance, with removal efficiencies of 14% for TiO_2, 69% for Fe/TiO_2, and 91% for Cu/TiO_2. This improvement is attributed to a red shift in absorption, indicating band gap narrowing due to metal-induced localized states. Among them, Cu/TiO_2 showed superior activity, as Cu effectively trapped photo-induced charge carriers, suppressing recombination and boosting degradation efficiency. The detailed degradation and defluorination reactions were also proposed in their work.[361]

$$TiO_2 + h\nu \rightarrow TiO_2(e_{CB}^- + h_{VB}^+) \quad (12)$$

$$TiO_2(h_{VB}^+) + H_2O \rightarrow TiO_2 + {}^{\bullet}OH + H^+ \quad (13)$$

$$C_7F_{15}COOH + {}^{\bullet}OH \rightarrow {}^{\bullet}C_7F_{15}COOH^+ + OH^- \quad (14)$$

$${}^{\bullet}C_7F_{15}COOH^+ \rightarrow {}^{\bullet}C_7F_{15} + CO_2 + H^+ \quad (15)$$

$${}^{\bullet}C_7F_{15} + H_2O \rightarrow C_7F_{15}COH + H^+ \quad (16)$$

$$C_7F_{15}COH \rightarrow C_6F_{13}COF + F^- + H^+ \quad (17)$$

$$C_6F_{13}COF + H_2O \rightarrow C_6F_{13}COOH + F^- + H^+ \quad (18)$$

Similarly, Xu *et al.* prepared Pt/In_2O_3 nanorods *via* photodeposition and studied their photocatalytic performance for PFOA degradation.[362] The removal rate increased from 62% to 98% as Pt loading rose to 3%, which was found to be optimal. However, at 5% loading, performance declined due to Pt particles acting as recombination centers and aggregating, which hindered the photocatalytic process. At 3%, Pt facilitated better electron–hole pair separation, enhancing the overall activity. Fig. 19 shows the photocatalytic mechanism, where Pt enhances activity by facilitating charge transfer and reducing electron–hole recombination.[362] It also extends the light absorption range, improving light utilization. However, excessive Pt can block active sites on In_2O_3 and act as a recombination center, hindering PFOA degradation.

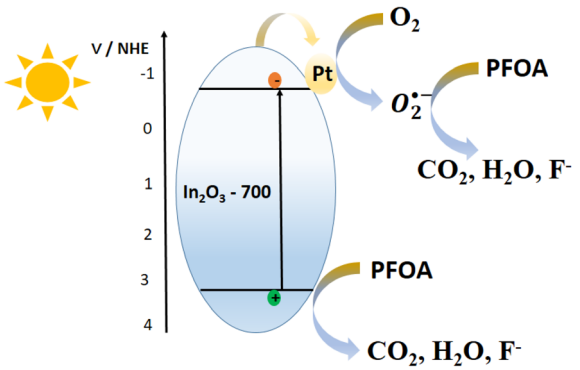

Fig. 19 Mechanisms highlight the photodegradation of PFOA.[362] "Reproduced from ref. 362 with permission from [Elsevier], copyright [2017]."

 © 2025 The Author(s). Published by the Royal Society of Chemistry

Open Access Article. Published on 02 September 2025. Downloaded on 11/10/2025 5:56:01 AM.
This article is licensed under a Creative Commons Attribution-NonCommercial 3.0 Unported Licence.

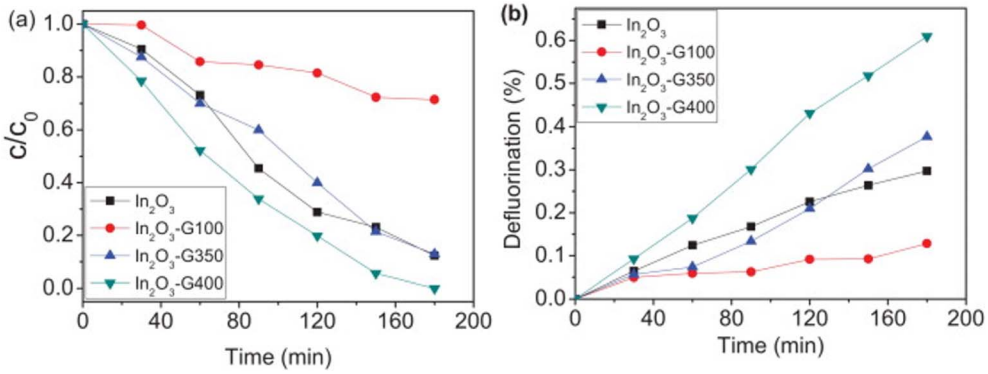

Fig. 20 (a) Photocatalytic decomposition and (b) defluorination of PFOA.[363] "Reproduced from ref. 363 with permission from [Elsevier], copyright [2013]."

In 2013, Li *et al.* synthesized an In_2O_3-graphene composite *via* sonochemical method and calcination at different temperatures to study its photocatalytic activity for PFOA degradation.[363] As shown in Fig. 20a,[363] In_2O_3-G400 completely decomposed PFOA within 3 hours, while In_2O_3 nanoparticles achieved 87% decomposition. In_2O_3-G350 showed similar results (87.6%), while In_2O_3-G100 was less effective, decomposing only 29% of PFOA. When In_2O_3 was calcined at 400 °C, it was partially enwrapped by graphene, which improved its photocatalytic activity by enhancing charge transfer and increasing its efficiency in breaking down PFOA.[363] The process of PFOA degradation is reported to occur in a stepwise manner, with one CF_2 unit removed at a time.[364,365] As shown in Fig. 20b,[363] the defluorination ratios for In_2O_3-G400, In_2O_3-G350, In_2O_3-G100, and In_2O_3 nanoparticles were 60.9%, 37.7%, 12.9%, and 29.7%, respectively, in 3 h.[363]

In 2019, wang *et al.* prepared g-C_3N_4/Fe_3O_4 composites through a two-step process and tested their photocatalytic performance for degrading phenanthrene in soil.[366] With Fe_3O_4 loadings of 16.32%, 23.96%, and 53.90%, the composites were effective under visible light. As shown in Fig. 21a,[366] up to 92.26% of phenanthrene was degraded within 120 minutes under visible light, while minimal degradation occurred in the dark, confirming that g-C_3N_4/Fe_3O_4 is activated by visible light. To evaluate the influence of Fe_3O_4 content, the photocatalytic activities of Fe_3O_4, pure g-C_3N_4, and g-C_3N_4/Fe_3O_4 with different loadings were compared (Fig. 21b).[366] Pure g-C_3N_4 showed weak activity, while loading with Fe_3O_4 enhanced performance, reaching a maximum at 23.96 wt% loading. This improvement is due to better visible light absorption and more efficient charge separation provided by the optimal Fe_3O_4 loading. Fig. 21c presents the DRS spectra of g-C_3N_4/Fe_3O_4 composites with different Fe_3O_4 loadings.[366] Pure g-C_3N_4 has a visible light absorption edge at 460 nm, corresponding to a band gap of 2.7 eV. Upon loading with Fe_3O_4, the visible light absorption ability of g-C_3N_4 significantly increases. This enhancement is due to the loading of Fe_3O_4, which broadens the light absorption range, and the absorption intensity increases proportionally with the Fe_3O_4 loading amount. Fig. 21d shows the PL spectra of Fe_3O_4, pure g-C_3N_4, and g-C_3N_4/Fe_3O_4 composites under 325 nm excitation.[366] Pure g-C_3N_4 shows a prominent emission peak around 460 nm, while the emission intensity of g-C_3N_4/Fe_3O_4 composites decreases as the Fe_3O_4 loading increases. This reduction indicates that Fe_3O_4 effectively suppresses the recombination of photo-induced electron–hole pairs, attributed to its good electrical conductivity. Combining DRS and PL results, the enhanced photocatalytic activity of g-C_3N_4/Fe_3O_4 is due to improved light absorption and efficient electron–hole pair separation, which is further validated by photocurrent measurements.[366] As is well known, higher photocurrent indicates better charge carrier separation and improved photocatalytic activity.[367] The photocurrent–time curves based on six cycles of visible light irradiation on-off mode is shown in Fig. 22a.[366] As shown in Fig. 22a,[366] g-C_3N_4/Fe_3O_4 exhibits a significantly higher photocurrent response than pure g-C_3N_4 under visible light, indicating enhanced charge separation and photocatalytic performance. This enhanced separation promotes the formation of radicals such as $^{\bullet}OH$ and $O_2^{\bullet-}$. To identify the dominant species, ESR measurements were performed using DMPO under visible light. As shown in Fig. 22b,[366] no ESR signals were seen in the dark except DMPO oxidation peaks,[368] while visible light produced a weak DMPO-$^{\bullet}OH$ signal (1 : 2 : 2 : 1 quartet) and a strong DMPO-$O_2^{\bullet-}$ signal, indicating that $O_2^{\bullet-}$ is the primary reactive species involved in the photocatalytic process, along with some contribution from $^{\bullet}OH$ radicals.[368–370] Based on these experimental results, Wang *et al.* illustrated a possible photocatalytic mechanism for g-C_3N_4/Fe_3O_4 in Fig. 23.[366] The enhanced activity is attributed to Fe_3O_4 loading, which extends visible light absorption and suppresses electron–hole recombination. Under visible light, g-C_3N_4 generates electrons and holes (reaction (1)), and the electrons transfer to Fe_3O_4 due to its lower CB and good conductivity, reducing recombination (reaction (2)). The electrons in Fe_3O_4's CB reduce surface O_2 to $O_2^{\bullet-}$ (reaction (3)), which can form $^{\bullet}OH$ on reacting with H_2O (reaction (4)). Due to the lower CB of g-C_3N_4 (+1.4 eV) than that of $^{\bullet}OH$ (+1.99 eV), it is difficult for the holes of g-C_3N_4 to generate $^{\bullet}OH$, explaining the weak ESR signal. Phenanthrene is then oxidized by $O_2^{\bullet-}$, $^{\bullet}OH$, and h^+ (reactions (5)–(7)).[366]

Open Access Article. Published on 02 September 2025. Downloaded on 11/10/2025 5:56:01 AM.
This article is licensed under a Creative Commons Attribution-NonCommercial 3.0 Unported Licence.

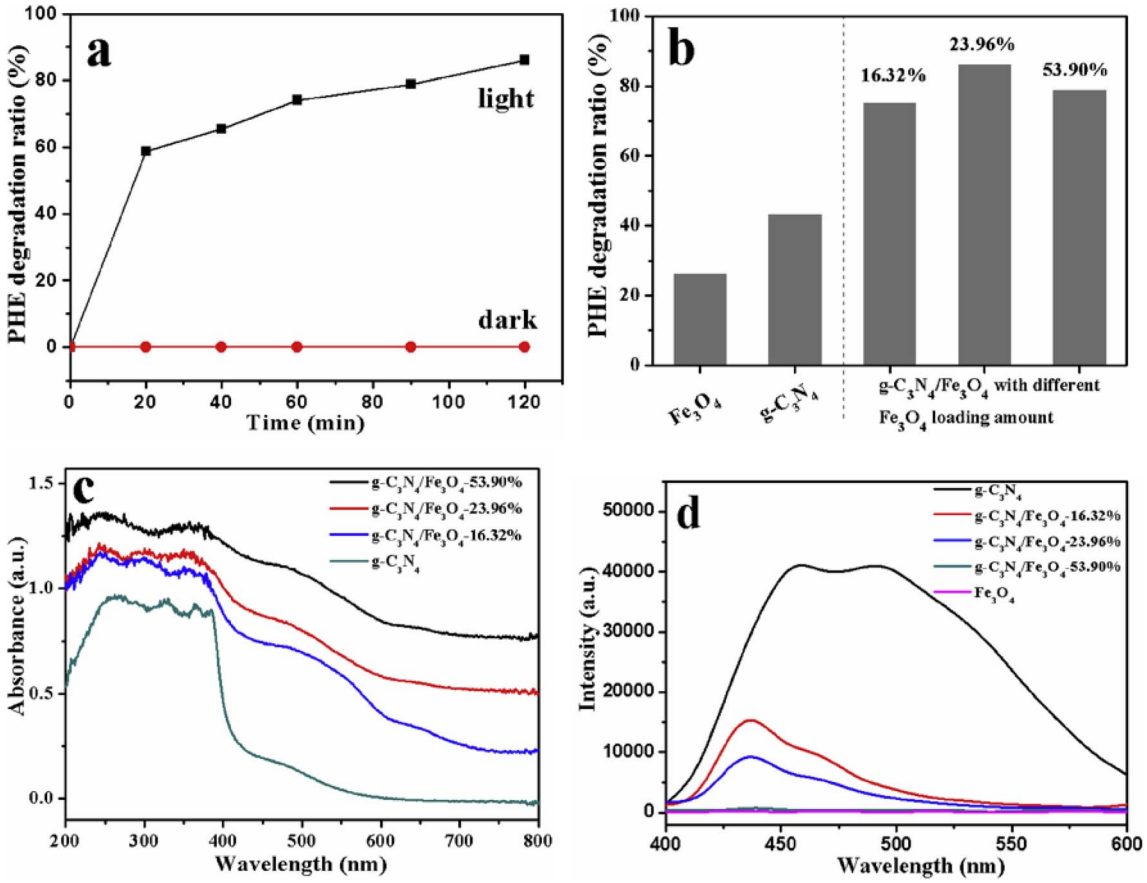

Fig. 21 (a) Phenanthrene photodegradation under visible light and dark conditions using g-C_3N_4/Fe_3O_4; (b) comparison of phenanthrene degradation rates for Fe_3O_4, pure g-C_3N_4, and g-C_3N_4/Fe_3O_4 with different Fe_3O_4 loadings (16.32 wt%, 23.96 wt%, and 53.90 wt%); (c) DRS spectra of bare g-C_3N_4 and g-C_3N_4/Fe_3O_4 composites with varying Fe_3O_4 concentrations; (d) PL spectra of Fe_3O_4 nanoparticles, bare g-C_3N_4, and g-C_3N_4/Fe_3O_4 at different Fe_3O_4 loadings.[366] "Reproduced from ref. 366 with permission from [Elsevier], copyright [2019]."

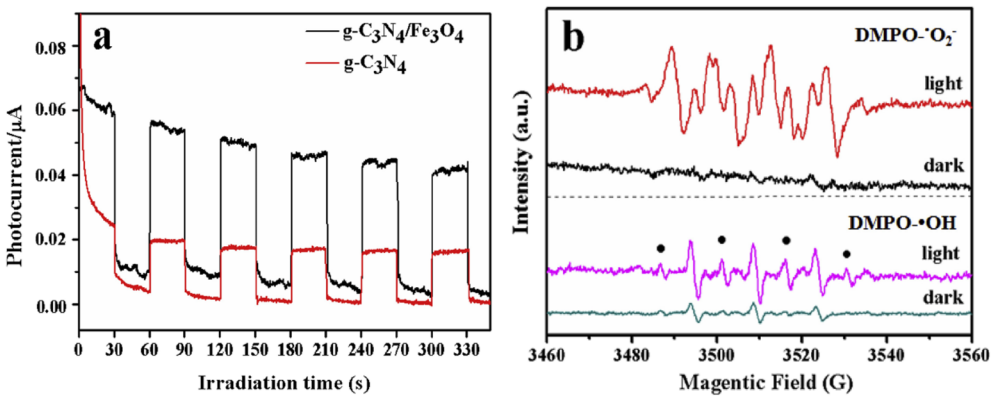

Fig. 22 (a) Photocurrent response comparison between pure g-C_3N_4 and g-C_3N_4/Fe_3O_4 under visible light, indicating improved charge separation in the composite; (b) ESR spectra of DMPO-$O_2^{\bullet-}$ and DMPO-$^{\bullet}$OH spin adducts for g-C_3N_4/Fe_3O_4 under visible light, confirming the generation of reactive oxygen species.[366] "Reproduced from ref. 366 with permission from [Elsevier], copyright [2019]."

Recently in 2024, Brindhadevi *et al.* synthesized NiO nanoparticles *via* co-precipitation and calcination at 900 °C for 3 h.[371] The photocatalytic activity was evaluated against PAHs, showing 79% degradation of pyrene (2 μg mL^{-1} anthracene) within 60 min (Fig. 24a).[371] Furthermore, maximum anthracene degradation (57%) was achieved at a NiO concentration of 10 μg mL^{-1} after 5 h of treatment (Fig. 24b).[371] Fig. 24c shows that anthracene degradation by NiO nanoparticles peaked at 72% under acidic conditions (pH 5) after 300 min.[371] Higher pH levels reduced degradation due to increased repulsive

 © 2025 The Author(s). Published by the Royal Society of Chemistry

Open Access Article. Published on 02 September 2025. Downloaded on 11/10/2025 5:56:01 AM.
This article is licensed under a Creative Commons Attribution-NonCommercial 3.0 Unported Licence.

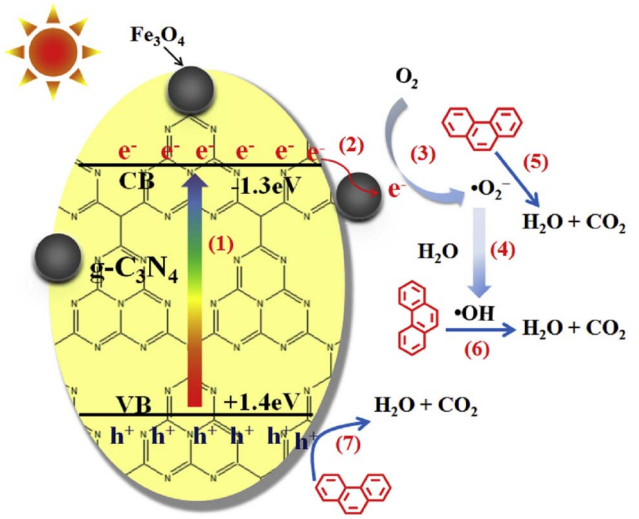

Fig. 23 Proposed schematic mechanism illustrating the transfer and separation of photoinduced charge carriers in the g-C_3N_4/Fe_3O_4 composite under visible light irradiation, highlighting the generation of reactive species responsible for enhanced photocatalytic activity.[366] "Reproduced from ref. 366 with permission from [Elsevier], copyright [2019]."

interactions between NiO nanoparticles and PAH molecules. They further investigated the influence of light sources on anthracene degradation (Fig. 24d).[371] With 2 μg mL^{-1} PAH and 10 μg mL^{-1} NiO nanoparticles over 300 min, they achieved 70% degradation under UV light and 64% under sunlight. The improved performance under UV was attributed to efficient generation of reactive radicals and electron–hole pairs, which enhances the photocatalytic activity of NiO.[371] Table 12 shows the photodegradation of some POPs using various metal oxide photocatalyst and their composites:

9.2. Photodegradation of dyes

The textile industry, especially in countries like India, Pakistan, Sri Lanka, and China, generates significant wastewater during processes like dyeing, printing, and finishing. These stages consume large amounts of water (120–280 L) and synthetic dyes made from coal and petroleum. About 11–15% of the dyes are washed out as effluent, leading to increased COD and BOD in water bodies.[390,391] Reactive dyes released into water can cause severe harm to both humans and aquatic organisms, including cancer risks and reproductive issues.[392] To combat this, photocatalytic degradation, particularly using metal oxide nanoparticles, offers a sustainable solution. These nanoparticles stand out for their high surface area, strong catalytic efficiency, and ability to produce reactive species that effectively break down a wide range of dyes in water.[393] Their excellent catalytic and adsorption properties, along with the ability to produce reactive species under certain conditions, offer an effective and versatile method for degrading various industrial dyes.[394] For instance, Torane *et al.* synthesized TiO_2 using a simple sol–gel method and tested its photocatalytic ability to degrade MB under sunlight.[395] The degradation results, shown in Fig. 25,[395]

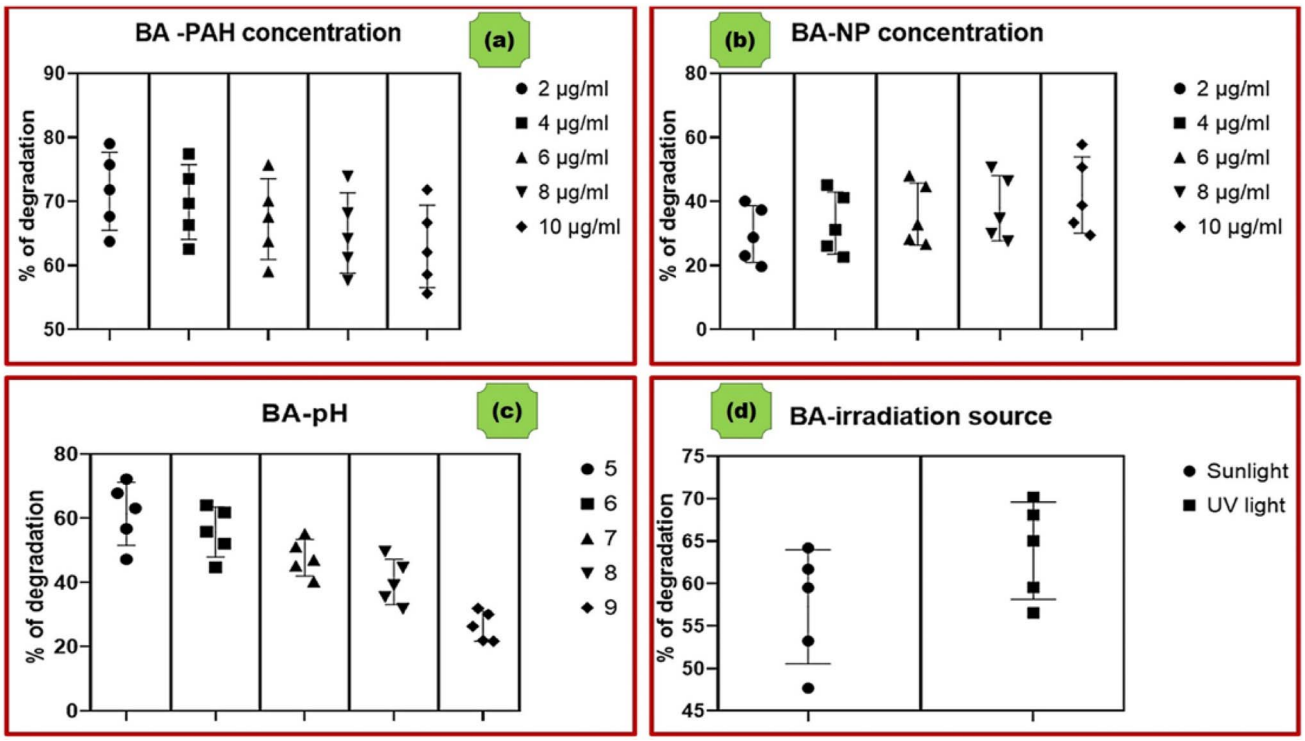

Fig. 24 Evaluation of the photocatalytic efficiency of NiO nanoparticles under different parameters: (a) variation with PAH concentration, (b) effect of NiO nanoparticle dosage, (c) influence of pH on degradation performance, and (d) comparison of photocatalytic activity under UV and sunlight exposure.[371] "Reproduced from ref. 371 with permission from [Elsevier], copyright [2024]."

Open Access Article. Published on 02 September 2025. Downloaded on 11/10/2025 5:56:01 AM.
This article is licensed under a Creative Commons Attribution-NonCommercial 3.0 Unported Licence.

Table 12 Photodegradation of POPs using metal oxides and their composites

Photocatalyst	E_g/eV	Light	Target pollutant	Decomposition	Ref.
TiO_2	3.14	16 W, 254 nm, UV	PFOA	86.0%	364
			PFDA	99.0%	
			PFNA	99.0%	
TiO_2	3.14	185 nm, VUV	PFOA	98.3%	372
TiO_2	3.2	UVA	PAH	93%	373
		UVC		92%	
Pt/TiO_2	2.92	125 W, 365 nm UV	PFOA	100%	374
Pd/TiO_2				94.2%	
Ag/TiO_2				57.7%	
Fe/TiO_2	3.32	400 W, 254 nm UV	PFOA	69.0%	375
Cu/TiO_2	3.29			91.0%	
TiO_2-rGO	2.94	150 W, UV	PFOA	86.0%	376
Sb_2O_3/TiO_2	3.12	4 W, UV	PFOA	81.7%	377
β-Ga_2O_3	4.80	15 W, 254 nm UV	PFOA	36.0%	378
Needle-like β-Ga_2O_3	4.68	14 W, 254 nm UV	PFOA	100%	379
In-Ga_2O_3	4.16	200 W, UV	PFOA	100%	380
In_2O_3 microspheres	2.68	15 W, 254 nm UV	PFOA	100%	381
In_2O_3 nanoplates	2.76			100%	
In_2O_3 nanocubes	2.72			100%	
Pt-In_2O_3	2.81	500 W, UV	PFOA	98.0%	362
CeO_2/In_2O_3	2.89/2.80	500 W, 254 nm UV	PFOA	100%	382
$BiPO_4$/BiOCl	4.20/3.38	254 nm UV	PFOA	100%	383
rGO/BiOCl	3.02	500 W, UV	PFOA	90.1%	384
ZnO	3.20	28 W, 254 nm UV	PFOA	70.5%	385
ZnO	3.37	Natural sunlight	PAH	98%	386
ZnO/rGO	3.11	Solar irradiation	PFOA	90.9%	387
ZnHCF@ZnO	2.2	Sunlight	Benz[*a*]anthracene (BaA)	93%	388
			Benzo[*a*]pyrene (BaP)	90%	
$CrFe_2O_4$	1.9	LED	Phenanthrene	99%	389
			Anthracene	90%	
			Naphthalene	86%	

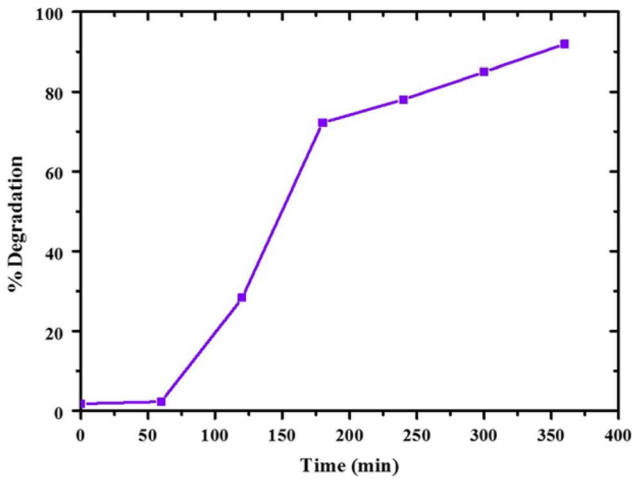

Fig. 25 Percentage degradation of MB dye over time with TiO_2 material.[395] "Reproduced from ref. 395 with permission from [Elsevier], copyright [2021]."

revealed a gradual reduction in MB concentration over time. In the absence of TiO_2, there was minimal degradation even after 360 minutes. However, when TiO_2 was introduced, the degradation rate was initially slow during the first 60 minutes, likely due to the time required for the catalyst to activate. After this period, the degradation rate increased significantly, and after 360 minutes, around 92% of the MB dye was degraded. This illustrates that TiO_2 effectively accelerates the degradation of MB.[395]

Recently, Faryad *et al.* prepared g-C_3N_4/TiO_2 composites through a straightforward hydrothermal method.[396] To improve their photocatalytic performance, boron nanoparticles were synthesized using a green process and incorporated into the composites *via* a two-stage wet-chemical co-precipitation method. The photocatalytic performance of the resulting composites was then evaluated against MB dye. They observed that the addition of a co-catalyst reduced the bandgap (E_g) of the host material from 2.7783 eV to 1.5678 eV, which promoted the generation of more photo-induced charge carriers in the B-doped g-C_3N_4/TiO_2 composites under visible light, as shown in Fig. 26a.[396] The incorporation of boron into the composite significantly enhanced its photocatalytic activity compared to the pure material, leading to a higher degradation rate of MB. This improvement was further evident as the proportion of the co-catalyst increased, as shown in Fig. 26b.[396]

In 2022, Selvaraj *et al.* synthesized ZnO doped with Sm *via* a co-precipitation method followed by calcination at 500 °C for 2 hours and assessed its photocatalytic efficiency against methylene blue (MB) under sunlight.[397] The photocatalytic activity of both pure ZnO and Sm-ZnO nanoflowers is presented

 © 2025 The Author(s). Published by the Royal Society of Chemistry

Open Access Article. Published on 02 September 2025. Downloaded on 11/10/2025 5:56:01 AM.
This article is licensed under a Creative Commons Attribution-NonCommercial 3.0 Unported Licence.

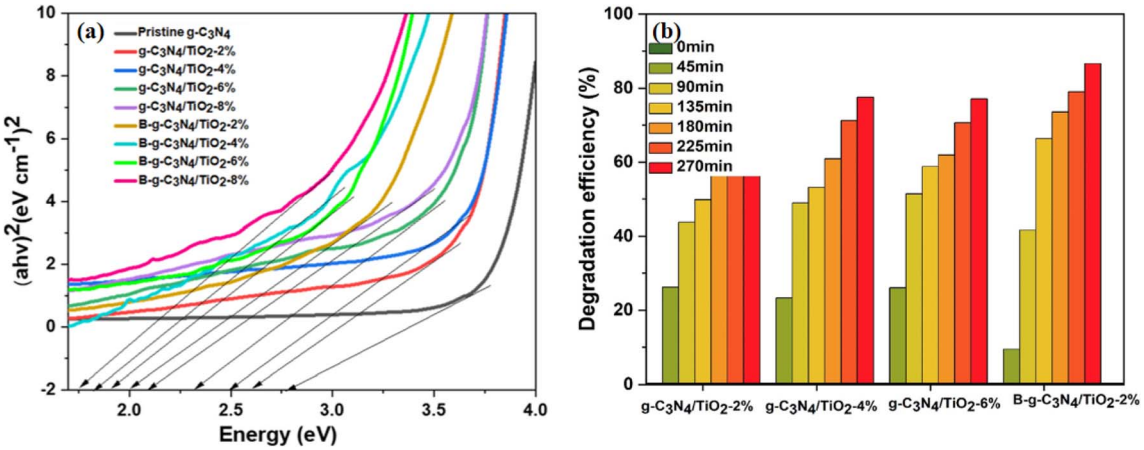

Fig. 26 (a) Bandgap analysis of g-C_3N_4, CNT-2%, CNT-4%, CNT-6%, CNT-8%, and BCNT-x composites; (b) evaluation of the photocatalytic degradation efficiency of g-C_3N_4/TiO_2-X (X = 2%, 4%, 6%) compared to B-doped g-C_3N_4/TiO_2-2%.[396] "Reproduced from ref. 396 with permission from [Elsevier], copyright [2023]."

in Fig. 27.[397] As shown in Fig. 27a,[397] MB degradation was monitored at different time intervals under sunlight exposure. In the absence of any catalyst, only 10% of MB degraded, indicating its high stability. However, introducing ZnO catalysts markedly enhanced degradation, with pristine ZnO achieving 57% efficiency, as depicted in Fig. 27c.[397] As the dopant concentration increased, the degradation efficiency improved. This was due to the presence of Sm^{3+} ions, which functioned as electron traps on the surface of ZnO nanoflowers. The captured electrons reacted with oxygen species, facilitating the degradation of organic pollutants. The highest degradation efficiency, around 96%, was achieved with 5% Sm-doped ZnO after 90 minutes of sunlight exposure. Fig. 27d displays the optical absorption spectra of the MB solution with 25 mg of the 5% Sm-ZnO catalyst under solar light exposure.[397] As the irradiation time increased, a decrease in the absorption peak intensity indicated the breakdown of MB molecules by the catalyst. The addition of Sm^{3+} ions into the ZnO structure shifted the conduction band maximum, created new energy states, and narrowed the bandgap due to their larger ionic

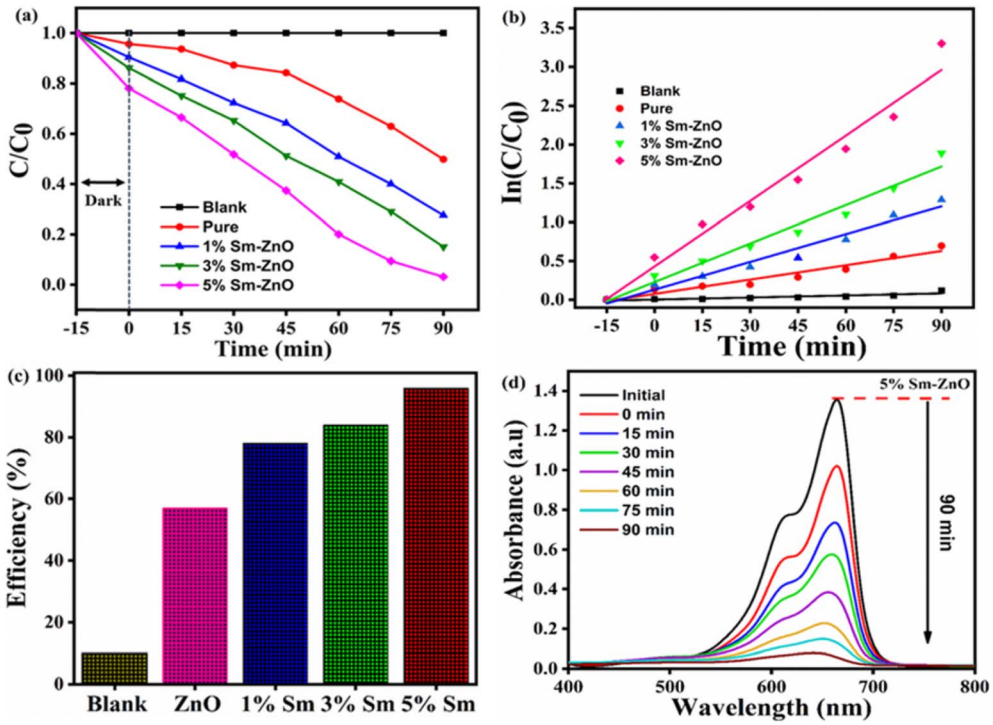

Fig. 27 (a) Variation in MB dye concentration with time, (b) kinetic plot of ln(C/C_0), (c) efficiency of MB degradation by the catalyst, and (d) UV-vis absorption spectra of MB after treatment with 5% Sm-ZnO.[397] "Reproduced from ref. 397 with permission from [Elsevier], copyright [2022]."

Open Access Article. Published on 02 September 2025. Downloaded on 11/10/2025 5:56:01 AM.
This article is licensed under a Creative Commons Attribution-NonCommercial 3.0 Unported Licence.

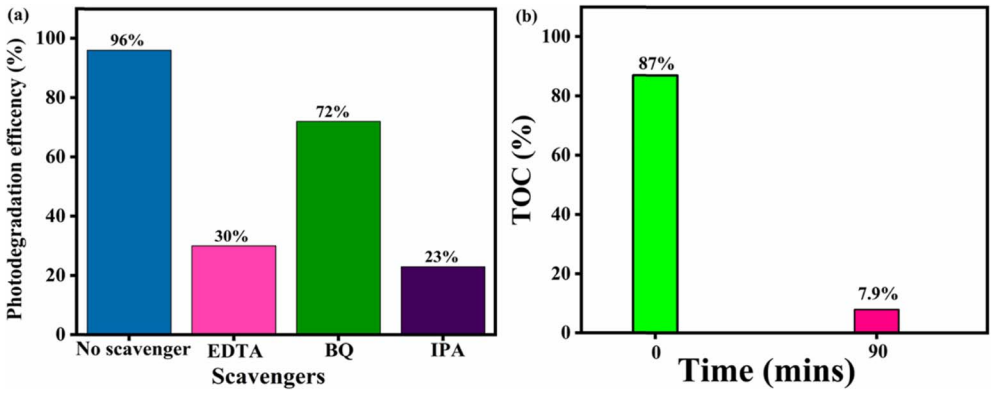

Fig. 28 (a) Reactive species trapping analysis and (b) TOC measurement results for 5% Sm-doped ZnO.[397] "Reproduced from ref. 397 with permission from [Elsevier], copyright [2022]."

radius. UV-Vis analysis confirmed the reduction in the bandgap with Sm^{3+} incorporation. The calculated values of ECB and EVB for 5% Sm-doped ZnO were −0.25 eV and 2.84 eV, respectively. The bandgap energy was reduced to around 3.09 eV, and the Sm^{3+} ions acted as effective electron scavenger. The trapping of electrons slowed down the recombination of electron–hole pairs, thereby significantly enhanced the photocatalytic degradation of MB. To pinpoint the primary reactive species responsible for this degradation, a series of scavenger experiments were conducted using 5% Sm-ZnO nanoparticles under optimized conditions. Different scavengers were employed to target specific active species: benzoquinone (BQ) for superoxide ions (O_2^-), isopropanol (IPA) for hydroxyl radicals ($^{\bullet}OH$), and EDTA for photogenerated holes (h^+), helping to clarify their individual roles in the reaction mechanism. Fig. 28a presents the photocatalytic performance of 5% Sm-ZnO nanoflowers for MB degradation in the presence of various scavenger agents.[397] Without any scavengers, the catalyst achieved approximately 96% degradation efficiency. However, when benzoquinone (BQ) was introduced to quench superoxide radicals, the efficiency dropped to about 72%. The use of isopropanol (IPA), which targets hydroxyl radicals, resulted in a significant decrease to 23%, indicating their major role. Similarly, adding EDTA to suppress photogenerated holes reduced the efficiency to around 30%, confirming the involvement of multiple reactive species in the degradation pathway. The results clearly indicate that hydroxyl radicals ($^{\bullet}OH$) and photogenerated holes (h^+) are the primary reactive species involved in the degradation process. The lowest degradation efficiency was observed with isopropanol (IPA), highlighting the crucial role of $^{\bullet}OH$ radicals, while the presence of EDTA showed a slightly higher degradation rate, suggesting that h^+ also plays a significant role. Although benzoquinone (BQ) suppressed the activity of superoxide radicals (O_2^-), its impact was less severe compared to IPA, confirming that $^{\bullet}OH$ and h^+ are the dominant species responsible for the effective photocatalytic breakdown of MB dye. They further carried out TOC analysis to further verify the mineralization capability of the 5% Sm-ZnO photocatalyst. As illustrated in Fig. 28b,[397] the carbon content was reduced by 87% from the initial concentration of methylene blue, with only 7.9% of the original carbon remaining after 90 minutes. This result indicates that the photocatalyst was able to effectively mineralize the methylene blue dye, converting it into environmentally benign products like CO_2 and H_2O, rather than simply decolorizing the solution.

In 2021, a study was conducted where Bi_2O_3 was doped with varying amounts of Ag (5%, 10%, and 15%) to examine its photocatalytic activity against crystal violet under visible light.[398] The photocatalytic performance of both pure Bi_2O_3 and Ag-doped Bi_2O_3 was compared by performing the photodegradation of crystal violet dye under visible light irradiation at 40 °C. The experiments were carried out using 50 mL of a 100 mg L^{-1} crystal violet solution and 0.05 g of each catalyst, with the degradation process monitored under visible light exposure. The data shown in Fig. 29 reveals the change in the concentration of crystal violet dye over time and the effect of varying Ag content.[398] Without light irradiation, there was little to no alteration in the dye concentration. However, the incorporation of Ag into Bi_2O_3 significantly enhanced its photocatalytic ability to degrade crystal violet. The degradation efficiency of a 100 mg L^{-1} crystal violet solution increased from 52% to 92%, 76%, and 57% with the addition of 5%, 10%, and

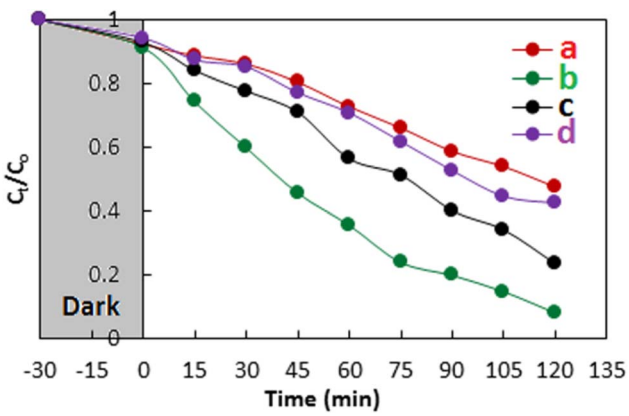

Fig. 29 Photocatalytic degradation of crystal violet dye (50 mL, 100 mg L^{-1}) at 40 °C with 0.05 g of catalyst: (a) Bi_2O_3, (b) 5% Ag-Bi_2O_3, (c) 10% Ag-Bi_2O_3, and (d) 15% Ag-Bi_2O_3.[398]

 © 2025 The Author(s). Published by the Royal Society of Chemistry

Open Access Article. Published on 02 September 2025. Downloaded on 11/10/2025 5:56:01 AM.
This article is licensed under a Creative Commons Attribution-NonCommercial 3.0 Unported Licence.

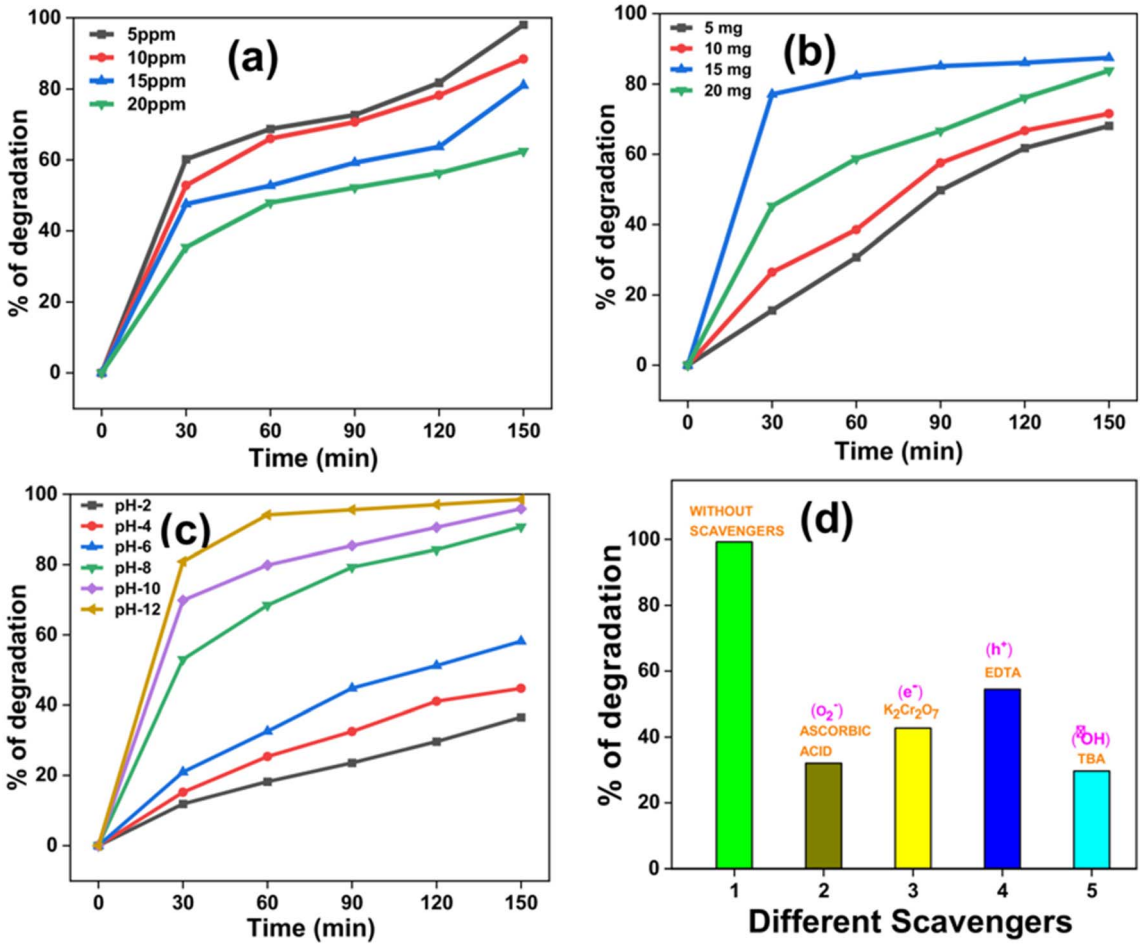

Fig. 30 Influence of (a) dye concentration, (b) catalyst dosage, (c) pH of the solution, and (d) role of various scavengers during MB degradation using CuO-NiO nanocomposite.[399] "Reproduced from ref. 399 with permission from [Elsevier], copyright [2023]."

15% Ag to Bi_2O_3, respectively. The Ag-doped Bi_2O_3 samples displayed improved photocatalytic performance compared to pure Bi_2O_3, with the 5% Ag-Bi_2O_3 demonstrating the most rapid degradation of crystal violet over 120 minutes. As the Ag content increased, it covered the active sites of Bi_2O_3, limiting the interaction between the catalyst and dye molecules, which resulted in lower photocatalytic activity. Moreover, excessive Ag loading introduced oxygen vacancies and defects in Bi_2O_3, which facilitated electron–hole recombination, further decreasing the overall catalytic efficiency.[398]

Sathisha *et al.* fabricated CuO-NiO nanocomposite *via* facile combustion synthesis and investigated its photocatalytic efficiency against MB under UV light irradiation.[399] Fig. 30 summarizes the optimized parameters influencing degradation performance.[399] As illustrated in Fig. 30a,[399] the highest degradation of MB was achieved at a dye concentration of 5 ppm. Fig. 30b reveals that a catalyst dosage of 15 mg yielded maximum photocatalytic activity.[399] The impact of pH, shown in Fig. 30c,[399] was explored across a range from pH 2 to 12. Notably, acidic conditions resulted in lower degradation rates, while an alkaline environment significantly enhanced the photocatalytic performance. Fig. 30d illustrates the impact of various scavengers on the photocatalytic degradation process.[399] The addition of *tert*-butyl alcohol (TBA) significantly suppressed the degradation efficiency, indicating that $^{\bullet}OH$ play a dominant role as the primary reactive species. In contrast, the presence of EDTA showed minimal influence on the degradation rate, suggesting minor contribution of the photogenerated h^+ to the overall photocatalytic mechanism.[399] Hossain *et al.* fabricated CuO/CdS composite using an ultrasound-assisted wet impregnation technique and assessed its photocatalytic activity under visible light irradiation against RhB, MB, and MO dyes.[400] The composite demonstrated impressive degradation efficiencies of approximately 93% for RhB, 83% for MB, and 80% for MO, highlighting its broad spectrum photocatalytic capability.[400] Table 13 shows the photodegradation of dyes using various metal oxide based photocatalysts along with their composites.

9.3. Photodegradation of pharmaceutical pollutants

It is estimated that roughly four-fifths of wastewater worldwide is released into the environment untreated, presenting significant threats to human well-being, aquatic ecosystems, and environmental stability.[419] Industrial discharges, particularly those containing synthetic dyes and pesticides, are major

Open Access Article. Published on 02 September 2025. Downloaded on 11/10/2025 5:56:01 AM.
This article is licensed under a Creative Commons Attribution-NonCommercial 3.0 Unported Licence.

Table 13 Photodegradation of dyes using various metal oxide based photocatalysts along with their composites

Photocatalyst	E_g/eV	Light	Target pollutant	Degradation	Ref.
Zn/TiO_2	3.0–3.2	Direct sunlight	MB	99%	401
Ni/TiO_2	2.86	UV	MO	51%	402
Fe/TiO_2	1.45	Visible light	MB	99.50%	403
CuO	1.66	Solar light	MB	75%	404
Cu_2O/PA/rGO	2.14	UV lamp	MO	95%	405
CuO	1.29	UV lamp	MB MO	95.63%	406
ZnO/CN	2.1	Visible light	MB	98%	407
ZnO/GO	3.25	UV lamp	Basic fuchsin	95%	408
$LaFeO_3$/rGO	1.86	300 W Xenon arc lamp	Methylene blue (MB), rhodamine B dye (RhB)	MB-98%, RhB-73%	409
Fe_2O_3/rGO	2.2	300 W Dy lamp with a 420 nm cutoff filter	Rhodamine B (RhB)	99%	410
$BiFeO_3$/rGO	1.8	Mercury Xenon lamp	RhB	87%	411
MgO	2.9	UV lamp	Methylene blue	75%	412
GO-MgO	4.8	Solar simulator	Methyl blue	45%	413
Co_3O_4	1.29 and 3.3	Mercury lamp	Methylene blue	93.80%	414
Cr : Co_3O_4	2.4	Fluorescent lamp (9 W)	MB	99%	415
Co_3O_4/RP composite	1.77	Xe lamp (300 W) with a cutoff filter (λ > 400 nm)	Malachite green (MG)	94.50%	416
CeO_2	3.34	UV light	MO MB	70% 77%	417
SnO_2	3.32	UV light	MO MB	78% 83%	417
WO_3	2.8	Visible light	MB	75%	418

sources of this pollution. Additionally, the frequent use of pharmaceutical products has introduced new classes of pollutants into water bodies, which are increasingly recognized for their detrimental effects on both ecological systems and human health.[420] Contamination from these pharmaceutical compounds in water sources has been associated with numerous health risks, such as cancer, hemorrhaging, organ impairment, hormonal disruptions, and toxic effects of varying severity in the human population worldwide.[421] With the growing concern of antibiotic resistance emerging in aquatic ecosystems, there is an urgent need to establish affordable, sustainable, and efficient treatment methods to eliminate these persistent contaminants from wastewater. Tailoring the surface and interfacial properties of photocatalyst significantly boosts their functionality by facilitating improved charge separation and active site availability. Consequently, heterogeneous photocatalysis has gained momentum as a practical, affordable, and highly efficient technique for eliminating pharmaceutical residues from contaminated water sources.[422,423] In this regard, Sood *et al.* fabricated Bi_2O_3/TiO_2 by the hydrothermal method and employed it for the photocatalytic breakdown of the antibiotic ofloxacin under sunlight at neutral pH.[424] The characteristic absorbance of ofloxacin at 287 nm gradually disappeared during the reaction with 10% BT catalyst, achieving nearly 92% degradation within 120 minutes (Fig. 31a).[424] Minimal change was observed without the catalyst, while limited degradation occurred in the absence of light, highlighting the synergistic role of the photocatalyst and solar light in the degradation process. As illustrated in Fig. 31b,[424] photolysis alone showed negligible effectiveness in degrading the drug molecule, while adsorption led to only partial removal. To evaluate the influence of Bi_2O_3 content on photocatalytic efficiency, composites with varying Bi/Ti molar ratios-1%, 5%, and 10%-were tested alongside pure TiO_2 and Bi_2O_3 under identical conditions. The results demonstrated that increasing the Bi_2O_3 content enhanced the photocatalytic performance, with 10% Bi_2O_3/TiO_2 exhibiting the highest degradation rate for ofloxacin, as reflected in Fig. 32a.[424] The degradation rates for the solar light-induced degradation of ofloxacin solution (25 mg L^{-1}, pH 7, 0.5 g L^{-1} catalyst dose) were 32.5%, 75.0%, 50.9%, 60%, and 92.4% for bare TiO_2, Bi_2O_3, 1% BT, 5% BT, and 10% BT catalysts, respectively. The enhanced catalytic activity of the 10% BT composite can be attributed to its increased visible light absorption, smaller particle size, and larger surface area. Comparative studies with commercially available TiO_2 derivatives such as P25, PC 50, and PC 500 also showed that the 10% BT catalyst outperformed these products, demonstrating superior degradation efficiency, as shown in Fig. 32b.[424]

Similarly, Rostami *et al.* synthesized $ZnFe_2O_4$-x wt% graphene (x = 1–4) nanohybrids *via* the sol–gel method and investigated their photocatalytic activity for the degradation of paracetamol under visible light irradiation.[425] As illustrated in Fig. 33a,[425] the nanocomposites exhibit significantly lower photoluminescence (PL) intensity compared to pure $ZnFe_2O_4$, suggesting a suppressed recombination rate of photogenerated electron–hole pairs. Fig. 33b further demonstrates that pure $ZnFe_2O_4$ shows negligible photocatalytic activity under visible light, while the incorporation of graphene markedly enhances

 © 2025 The Author(s). Published by the Royal Society of Chemistry

Open Access Article. Published on 02 September 2025. Downloaded on 11/10/2025 5:56:01 AM.
This article is licensed under a Creative Commons Attribution-NonCommercial 3.0 Unported Licence.

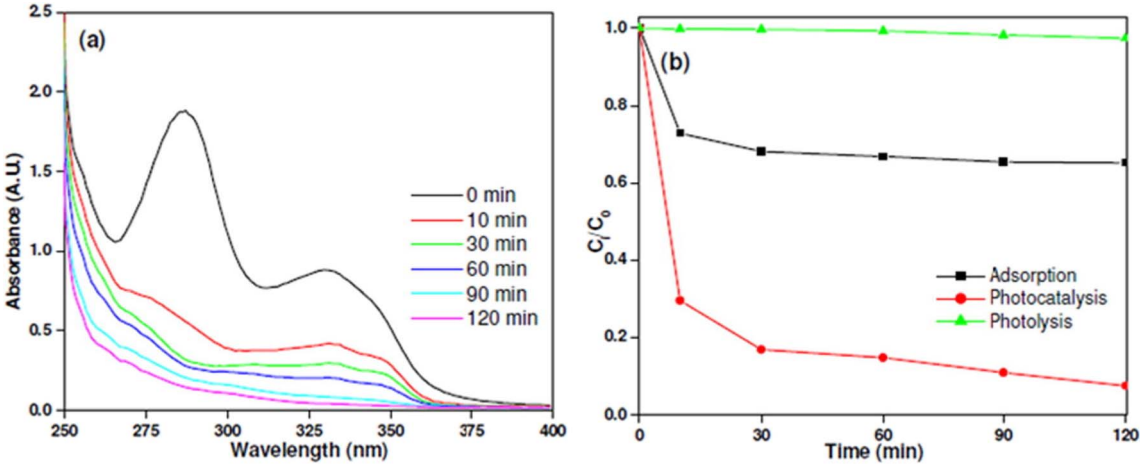

Fig. 31 (a) Absorbance spectra of ofloxacin (25 mg L^{-1}, pH 7) as a function of time using 0.5 g L^{-1} catalyst dose; (b) comparative analysis of ofloxacin removal *via* photocatalysis, photolysis (solar light only), and adsorption (in dark conditions).[424] "Reproduced from ref. 424 with permission from [Elsevier], copyright [2016]."

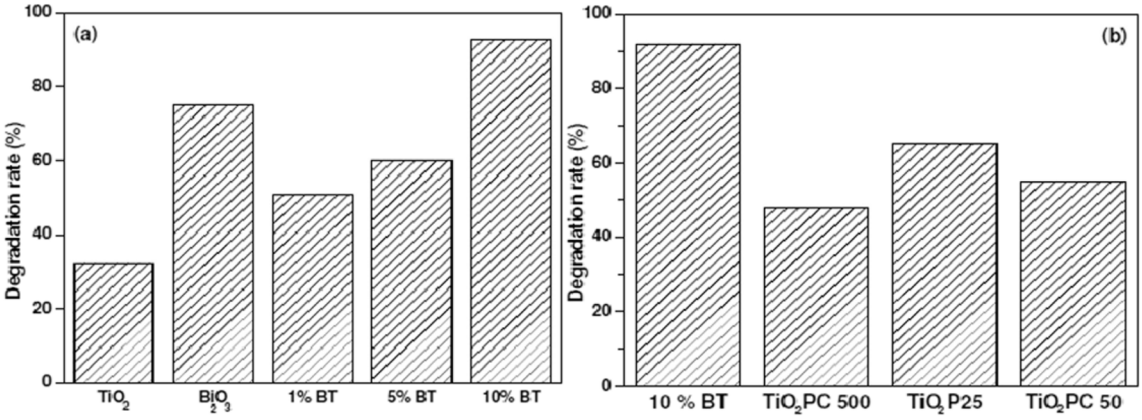

Fig. 32 (a) Assessment of photocatalytic degradation of ofloxacin using synthesized photocatalysts including TiO_2, Bi_2O_3, and varying Bi_2O_3-loaded TiO_2 composites (*x*% BT) under solar light (25 mg L^{-1}, pH 7, 0.5 g L^{-1} catalyst, 120 min reaction time); (b) comparative evaluation of 10% Bi_2O_3-TiO_2 composite with commercially available TiO_2 photocatalysts under the same experimental setup.[424] "Reproduced from ref. 424 with permission from [Elsevier], copyright [2016]."

the degradation efficiency.[425] This enhancement is primarily attributed to the improved charge separation and transfer facilitated by the graphene sheets, which serve as electron conductors. Overall, the $ZnFe_2O_4$-graphene nanohybrids exhibit superior photocatalytic performance for paracetamol degradation under visible light, highlighting the synergistic effect of graphene in boosting the activity of zinc ferrite. Among the synthesized composites, the $ZnFe_2O_4$-4 wt% graphene nanohybrids exhibited the highest photocatalytic performance, achieving approximately 97.4% degradation of paracetamol within 180 minutes. The proposed photocatalytic mechanism is illustrated in Fig. 33c.[425] Under visible light irradiation, electrons in $ZnFe_2O_4$ are excited from the valence band (h^+) to the conduction band (e^-). These excited electrons are rapidly transferred to the graphene nanosheets, where they are captured by adsorbed oxygen molecules to generate reactive superoxide radicals ($O_2^{\bullet-}$). Meanwhile, the photogenerated holes contribute to the formation of hydroxyl radicals. These reactive species, including holes, superoxide anion radicals, and hydroxyl radicals, subsequently oxidize paracetamol molecules adsorbed on the $ZnFe_2O_4$-graphene surface *via* π–π interactions and/or electrostatic attraction. Thus, graphene plays multiple crucial roles; acting as an electron acceptor, promoting charge separation, enhancing adsorption, and serving as a photosensitizer, collectively contributing to the enhanced photocatalytic degradation of paracetamol.[425]

Recently, Hunge *et al.* synthesized MoS_2/ZnO heterostructures through a hydrothermal process and assessed their photocatalytic behavior against the antibiotic ciprofloxacin.[426] As illustrated in Fig. 34a,[426] pristine ZnO possessed a wide band gap of 3.17 eV, whereas MoS_2 displayed a much narrower gap of 1.51 eV. Upon increasing the MoS_2 proportion in the composite, the band gap gradually decreased from 3.06 eV in MZ-10 to 2.81 eV in MZ-50. This shift towards lower energy is linked to

Open Access Article. Published on 02 September 2025. Downloaded on 11/10/2025 5:56:01 AM.
This article is licensed under a Creative Commons Attribution-NonCommercial 3.0 Unported Licence.

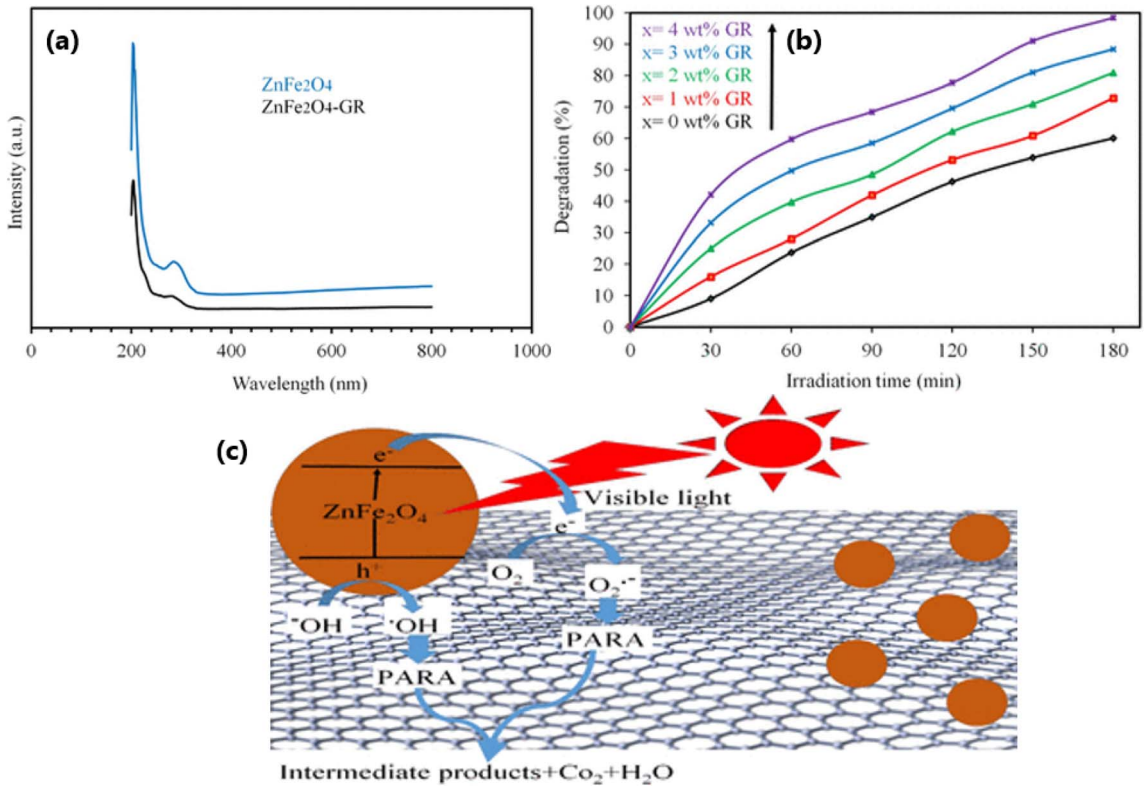

Fig. 33 (a) PL spectra of the pure and hybrid material, (b) photodegradation of paracetamol under visible light, and (c) mechanism of photodegradation of paracetamol using the composite.[425]

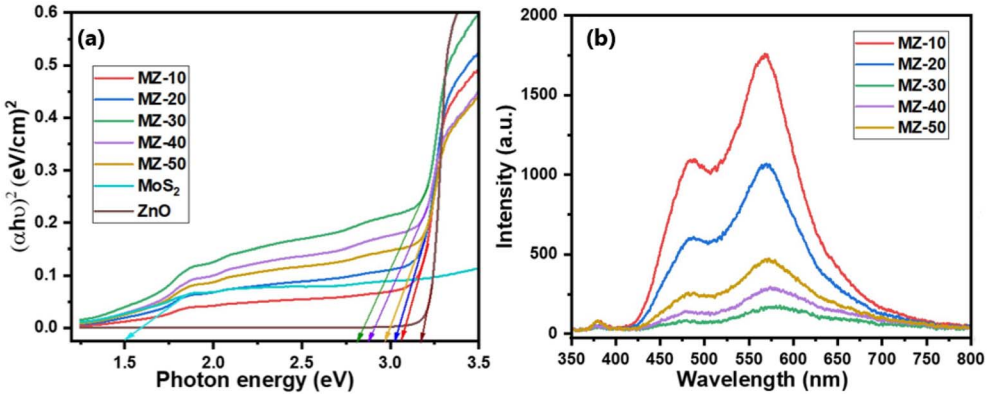

Fig. 34 (a) Bandgap plots of pure ZnO, MoS_2 and ZnO/MoS_2 hybrid, (b) PL spectra of ZnO/MoS_2 hybrid.[426] "Reproduced from ref. 426 with permission from [Elsevier], copyright [2023]."

a rise in carrier density in the conduction and valence bands, along with the development of trap states in the conduction band, which collectively lead to a downward shift in the conduction band edge and a narrower band gap. Fig. 34 presents the photoluminescence (PL) spectra of MoS_2/ZnO composites, highlighting emission features in both the near-ultraviolet and visible regions.[426] A gradual reduction in PL intensity was observed with increasing MoS_2 content, reaching a minimum at 30% loading (MZ-30). A distinct peak at 381 nm in the UV region corresponds to exciton–exciton recombination. The observed PL intensity followed the sequence: MZ-10 > MZ-20 > MZ-50 > MZ-40 > MZ-30. The significantly suppressed PL signal in the MZ-30 sample indicates minimized electron–hole recombination, thereby reflecting superior charge separation efficiency, an essential characteristic for improved photocatalytic performance. Fig. 35a presents the extinction spectra of ciprofloxacin (CIP) degradation under visible light using the MZ-30 photocatalyst.[426] The extinction profile of CIP revealed a primary peak at approximately 270 nm, with two additional smaller peaks at 320 and 330 nm. Over time, the intensity of

 © 2025 The Author(s). Published by the Royal Society of Chemistry

Open Access Article. Published on 02 September 2025. Downloaded on 11/10/2025 5:56:01 AM.
This article is licensed under a Creative Commons Attribution-NonCommercial 3.0 Unported Licence.

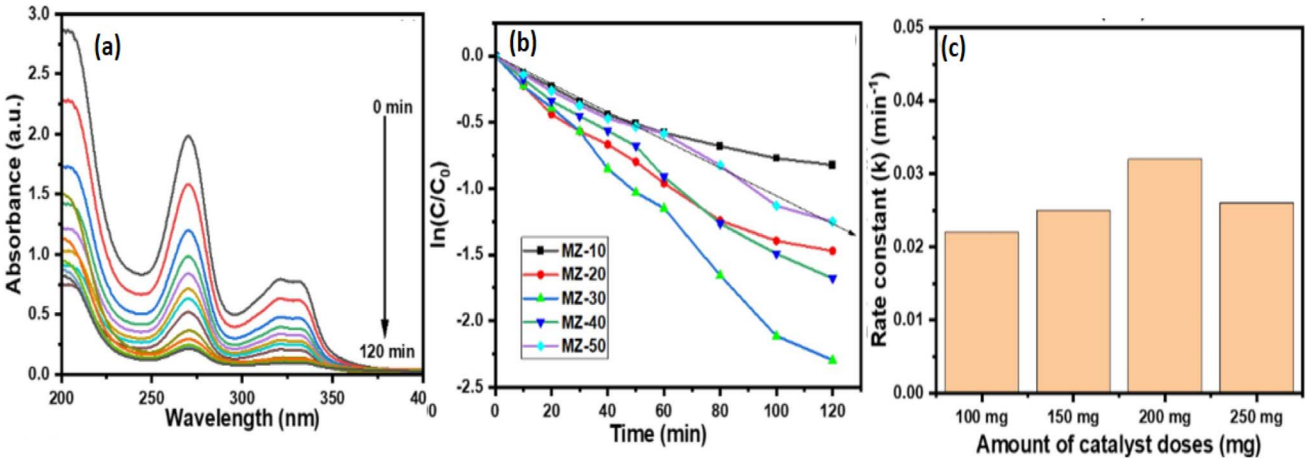

Fig. 35 (a) Excitation spectra of ciprofloxacin antibiotic using 30%-MoS_2/ZnO sample, (b) plot of ln(C/C_0) *vs.* time, and (c) rate constant values for varying amounts of catalyst dosage.[426] "Reproduced from ref. 426 with permission from [Elsevier], copyright [2023]."

Table 14 Photodegradation of some pharmaceutical pollutants by metal oxides and their various composites

Photocatalyst	Band gap	Light	Target pollutant	Degradation	Ref.
TiO_2	3.07	UV lamp, 30 mW cm^{-2}	TC	90%	427
Zn-doped TiO_2	3.02	Xenon lamp, 500 W	TC	85.27	428
TiO_2/g-C_3N_4 (TCN)	3.19	Xenon lamp, 300 W	TC	82.5%	429
Bi_2O_3	2.8	300 W Xe	TC	80%	430
$NiFe_2O_4/Bi_2O_3$	1.67	150 W Xe	TC	90.78%	431
Zn-doped Cu_2O	2.024	Visible light	Ciprofloxacin	94.6%	432
CeO_2@WO_3	2.72	Visible light	Cephalexin	96.26%	433
WO_3	2.79	Visible light	Cephalexin	57.06	433
Ag-CeO_2@SnO_2	2.2 eV	Sunlight	TC	96%	434
			MNZ	94%	
CeO_2	2.86	Visible light	SMR	24%	435
La-CeO_2	2.70			81%	
CdO	2.4–3.5	Solar light	Levofloxacin	80%	436
			Nizatidine	70%	

these peaks gradually decreased, confirming the progressive degradation of CIP under the combined influence of the catalyst and light. This process is attributed to the efficient charge transfer between MoS_2 and ZnO, as well as the robust redox reactions taking place on the catalyst surface. Among the different composites, the MZ-30 sample demonstrated the highest photocatalytic efficiency, which can be explained by its optimized band structure and composition. The degradation of CIP using the MZ-30 catalyst reached 89% within 120 minutes of visible light exposure. In contrast, other composites showed lower degradation efficiencies: 57% for MZ-10, 76% for MZ-20, 81% for MZ-40, and 72% for MZ-50. The superior performance of the MZ-30 composite is attributed to its favorable band alignment and enhanced light absorption capabilities, which outperform the pure ZnO catalyst. Fig. 35b presents the graph of ln(C/C_0) *versus* time for the different MZ composites, showing a consistent pattern of decreasing ciprofloxacin (CIP) concentration over time, signaling effective degradation.[426] To assess the impact of catalyst dosage, experiments were conducted using the MZ-30 catalyst while keeping the concentration of CIP and solution volume constant. The catalyst dose was varied from 100 to 250 mg in 50 mg increments. The degradation efficiencies observed for these doses were 91.12%, 94.06%, 96.18%, and 92.10%, respectively (Fig. 35c).[426] The observed increase in degradation efficiency with higher catalyst dosages is due to the greater surface area available for redox reactions, leading to more charge carrier generation. However, beyond a dosage of 200 mg, the reaction rate and degradation efficiency began to decrease. This can be attributed to increased solution turbidity, which results in particle aggregation and a light screening effect, diminishing the catalyst's ability to absorb light and reducing the overall reaction rate.[426] Table 14 shows the photodegradation of some pharmaceutical pollutants by metal oxides and their various composites.

10. Conclusion

The increasing levels of synthetic dyes, pharmaceutical residues, and persistent organic pollutants (POPs) in many environmental compartments have become a major worldwide problem. They are especially dangerous to aquatic ecosystems and human health because of their chemical stability, resistance to

Open Access Article. Published on 02 September 2025. Downloaded on 11/10/2025 5:56:01 AM.
This article is licensed under a Creative Commons Attribution-NonCommercial 3.0 Unported Licence.

biodegradation, potential for bioaccumulation, and long-range transport characteristics. Since these pollutants have been connected to neurotoxicity, carcinogenicity, endocrine disruption, and antibiotic resistance, immediate and efficient cleanup measures are required. Their extensive presence in water, soil, and air is a serious hazard to both ecological systems and public health. Through extensive classification, structural analysis, and source identification, supported by real-world examples; this review has showed how these pollutants originate, disperse, and accumulate across environmental matrices.

To address their complicated and resistant nature, the review looked at the principles and mechanisms of heterogeneous photocatalysis. It emphasises how light energy and semiconductor materials can be used to completely degrade these contaminants. Metal oxide-based photocatalysts, such as TiO_2, ZnO, WO_3, CuO, Cu_2O, *etc.* were given particular attention because of their strong oxidative capabilities, environmental compatibility, and structural stability. The photocatalytic mechanism, involving light absorption, electron–hole pair generation, and formation of reactive oxygen species, was discussed in detail to establish a foundational understanding of pollutant breakdown processes. However, despite their potential benefits, these photocatalysts exhibit several significant limitations. Many metal oxides primarily absorb UV light and possess wide band gaps, which lead to the rapid recombination of charge carriers, thereby reducing their photodegradation efficiency. To overcome these challenges, material innovations that improve photocatalytic performance were covered extensively in the review. These included metal and non-metal elemental doping, heterojunction formation (*e.g.*, p–n junctions and Z-scheme systems), and support material integration to increase surface area and electron mobility. The effects of each modification strategy on degradation efficiency, light absorption, charge carrier separation, band gap tuning, and overall performance were considered. Of these, Z-scheme heterojunctions were noted for their ability to preserve strong redox potential while facilitating effective charge separation-an ideal balance for treating persistent and toxic pollutants. The practical applicability of these fabricated materials was confirmed by a comprehensive collection of studies describing the degradation of POPs, dyes, and pharmaceutical residues under UV and visible light.

Nevertheless, a major challenge remains: after water treatment, it is still difficult to separate the catalyst particles from the solution, which hinders the scalability of the process for real-world applications. In conclusion, this review highlights the growing problem of environmental pollution and how advanced metal oxide-based photocatalysts offer a smart and effective solution. By combining knowledge of pollutants and modern technologies, it shows a clear path toward a cleaner and healthier future.

11. Challenges and future outlook

Even though metal oxide photocatalysts have great potential for degrading POPs, dyes, and pharmaceutical pollutants, there are still a number of significant obstacle that prevent their widespread use. These contaminant are extremely resistant to traditional degrading techniques due to their complex chemical structures and stable molecular bonds, which is one of the primary causes of their difficulties in being broken down.

Although photocatalytic degradation methods are extremely effective under controlled settings, they frequently have major limits when applied to stable contaminants. Most of the research on metal oxide photocatalysts, such as TiO_2 and ZnO, focuses on material that primarily absorb in the UV region, which accounts for just a small fraction of total solar light. This drastically reduces their efficiency under real-world settings. Furthermore, the quick recombination of photogenerated electron–hole pairs lowers photocatalytic performance. Although tactics such as doping, morphological tuning, and heterojunction generation (*e.g.*, type-II and p–n systems) have been used, they are still limited by weak redox potentials and poor charge separation. In contrast, Z-scheme photocatalysts offer improved charge separation and redox capabilities; however, they also face challenges such as limited light-harvesting ability and dependence on expensive rare-earth materials. Another practical challenge is the difficulty in recovering and reusing photocatalysts after treatment, which complicates large-scale application and raises concerns about secondary contamination.

Therefore, future studies must concentrate on designing photocatalysts with strong and stable redox characteristics, high visible light activity, and easy recovery or immobilisation for reuse in order to close these gaps. Designing multifunctional composites materials that are affordable, safe for the environment, and able to target many contaminants at once is obviously necessary. In addition, long-term operational stability studies and real-world testing in complicated wastewater matrices are necessary to advance beyond lab-scale viability. To turn these developments into workable environmental solutions, photocatalysis must be integrated with complementing treatment technologies, and scalable synthesis pathways must be developed. Additionally, the use of computational tools such as DFT and machine learning (ML) is essential for predicting the performance of photocatalysts, tuning their electronic structure, and guiding the rational fabrication of novel materials. Artificial Intelligence (AI) and machine learning (ML) are revolutionizing this process by offering insight into nanomaterial toxicity, enhancing life cycle assessments, and ensuring environmental safety. In tackling complex environmental remediation problems, the integration of principles of green chemistry with computational modeling and AI-driven frameworks will enables the fabrication of advanced photocatalysts that are not only highly efficient but also sustainable, scalable, and economically feasible.

Conflicts of interest

The authors declare that they have no competing interests.

Data availability

No primary research results, software or code have been included and no new data were generated or analysed as part of this review

 © 2025 The Author(s). Published by the Royal Society of Chemistry

Open Access Article. Published on 02 September 2025. Downloaded on 11/10/2025 5:56:01 AM.
This article is licensed under a Creative Commons Attribution-NonCommercial 3.0 Unported Licence.

References

1 O. M. L. Alharbi, A. A. Basheer, R. A. Khattab and I. Ali, *J. Mol. Liq.*, 2018, **263**, 442–453.
2 L. Ritter, *Int. Program. Chem. Saf. Within Framew. Inter-organization Program. Sound Manag. Chem. (IOMC)*, 1998.
3 V. K. Gupta and I. Ali, *Environmental water: advances in treatment, remediation and recycling*, 2012.
4 X. Duan, Y. Huang, C. Shen, P. Jones and X. Deng, *Indoor Air*, 2025, **2025**, 1071778.
5 A. Pariatamby and Y. L. Kee, *Procedia Environ. Sci.*, 2016, **31**, 842–848.
6 M. Porta, E. Puigdomènech, F. Ballester, J. Selva, N. Ribas-Fitó, S. Llop and T. López, *Environ. Int.*, 2008, **34**, 546–561.
7 P. O. Darnerud, S. Lignell, A. Glynn, M. Aune, A. Törnkvist and M. Stridsberg, *Environ. Int.*, 2010, **36**, 180–187.
8 Y. M. Lee, K. S. Kim, D. R. Jacobs and D. H. Lee, *Obes. Rev.*, 2017, **18**, 129–139.
9 V. H. Nguyen, S. M. Smith, K. Wantala and P. Kajitvichyanukul, *Arabian J. Chem.*, 2020, **13**, 8309–8337.
10 M. M. Bratu, S. Birghila, C. Birghila, D. A. Danilov, V. Coatu, E. Ristea and N. A. Damir, *Int. J. Environ. Res.*, 2025, **19**, 1–12.
11 C. E. Talsness, *Environ. Res.*, 2008, **108**, 158–167.
12 K. C. Jones and P. De Voogt, *Environ. Pollut.*, 1999, **100**, 209–221.
13 D. A. Ratcliffe, *Nature*, 1967, **215**, 208–210.
14 J. J. Hickey and D. W. Anderson, *Science*, 1968, **162**, 271–273.
15 M. A. Haegele and R. H. Hudson, *Arch. Environ. Contam. Toxicol.*, 1974, **2**, 356–363.
16 B. Sun, Q. Li, M. Zheng, G. Su, S. Lin, M. Wu, C. Li, Q. Wang, Y. Tao, L. Dai, Y. Qin and B. Meng, *Environ. Pollut.*, 2020, **265**, 114908.
17 L. Zhang, R. G. Nichols, J. Correll, I. A. Murray, N. Tanaka, P. B. Smith, T. D. Hubbard, A. Sebastian, I. Albert, E. Hatzakis, F. J. Gonzalez, G. H. Perdew and A. D. Patterson, *Environ. Health Perspect.*, 2015, **123**, 679–688.
18 L. Ritter, K. R. Solomon, J. Forget, M. Stemeroff and C. O'leary, *Int. Program. Chem. Saf. (IPCS)*, PCS/95.39, Geneva World Heal. Organ., 1995, vol. 65, p. 66.
19 C. J. Vörösmarty, P. B. McIntyre, M. O. Gessner, D. Dudgeon, A. Prusevich, P. Green, S. Glidden, S. E. Bunn, C. A. Sullivan, C. R. Liermann and P. M. Davies, *Nature*, 2010, **467**, 555–561.
20 R. P. Schwarzenbach, B. I. Escher, K. Fenner, T. B. Hofstetter, C. A. Johnson, U. Von Gunten and B. Wehrli, *Science*, 2006, **313**, 1072–1077.
21 H. Zeghioud, N. Khellaf, A. Amrane, H. Djelal, M. Bouhelassa, A. A. Assadi and S. Rtimi, *Environ. Sci. Pollut. Res.*, 2021, **28**, 12490–12499.
22 M. Saeed, M. Usman, M. Ibrahim, A. Ul Haq, I. Khan, H. Ijaz and F. Akram, *Int. J. Chem. React. Eng.*, 2020, **18**, DOI: **10.1515/IJCRE-2020-0004/MACHINEREADABLECITATION/RIS**.
23 Z. Shen, Y. Zhou, Y. Guo, J. Zhao, J. Song, Y. Xie, Y. Ling and W. Zhang, *Chin. Chem. Lett.*, 2021, **32**, 2524–2528.
24 A. Di Mauro, M. M. Natile, A. Landström, I. Concina, M. Ferroni, V. Privitera, G. Impellizzeri and M. Epifani, *J. Photochem. Photobiol., A*, 2021, **413**, 113258.
25 F. Mansouri, K. Chouchene, N. Roche and M. Ksibi, *Appl. Sci.*, 2021, **11**, 6659.
26 D. Sud and P. Kaur, *Crit. Rev. Environ. Sci. Technol.*, 2012, **42**, 2365–2407.
27 J. O. Ighalo, P. S. Yap, K. O. Iwuozor, C. O. Aniagor, T. Liu, K. Dulta, F. U. Iwuchukwu and S. Rangabhashiyam, *Environ. Res.*, 2022, **212**, 113123.
28 Ü. Ündeğer and N. Başaran, *Arch. Toxicol.*, 2005, **79**, 169–176.
29 N. M. Islam, M. Chatterjee, Y. Ikushima, T. Yokoyama and H. Kawanami, *Int. J. Mol. Sci.*, 2010, **11**, 164–172.
30 S. H. Khan and B. Pathak, *Environ. Nanotechnol., Monit. Manage.*, 2020, **13**, 100290.
31 H. X. Guo, K. L. Lin, Z. S. Zheng, F. Bin Xiao and S. X. Li, *Dyes Pigm.*, 2012, **92**, 1278–1284.
32 H. Dong, G. Zeng, L. Tang, C. Fan, C. Zhang, X. He and Y. He, *Water Res.*, 2015, **79**, 128–146.
33 S. Zhang, B. Li, X. Wang, G. Zhao, B. Hu, Z. Lu, T. Wen, J. Chen and X. Wang, *Chem. Eng. J.*, 2020, **390**, 124642.
34 R. Ma, S. Zhang, T. Wen, P. Gu, L. Li, G. Zhao, F. Niu, Q. Huang, Z. Tang and X. Wang, *Catal. Today*, 2019, **335**, 20–30.
35 H. Du, A. Zhang, Q. Zhang, Y. Sun, H. Zhu, H. Wang, Z. Tan, X. Zhang and G. Chen, *Sep. Purif. Technol.*, 2025, **359**, 130597.
36 Q. Han, L. Wang, J. Li, Y. Dong, Y. Ma, J. Zhang and S. Yu, *Chem. Eng. J.*, 2025, **519**, 165290.
37 M. A. Ashraf, *Environ. Sci. Pollut. Res.*, 2017, **24**, 4223–4227.
38 M. S. El-Shahawi, A. Hamza, A. S. Bashammakh and W. T. Al-Saggaf, *Talanta*, 2010, **80**, 1587–1597.
39 H. Fiedler, *Persistent Organic Pollutants*, Springer Science & Business Media, 2002, vol. 3.
40 J. Aravind kumar, T. Krithiga, S. Sathish, A. A. Renita, D. Prabu, S. Lokesh, R. Geetha, S. K. R. Namasivayam and M. Sillanpaa, *Sci. Total Environ.*, 2022, **831**, 154808.
41 T. Harner, K. Pozo, T. Gouin, A. M. Macdonald, H. Hung, J. Cainey and A. Peters, *Environ. Pollut.*, 2006, **144**, 445–452.
42 W. R. Kelce, C. R. Stone, S. C. Laws, L. E. Gray, J. A. Kemppainen and E. M. Wilson, *Nature*, 1995, **375**, 581–585.
43 H. Gupta, S. Dhiman, A. Kumar, S. K. Paliwal, G. Khan, H. Singh, A. Mishra and A. K. Mishra, *Sep. Purif. Rev.*, 2025, **54**, 3–16.
44 S. M. Yun, J. Ki Yoon, J. I. Kim, I. J. Kim, H. K. Kim, H. M. Chung, D. J. Kim and H. J. Noh, *Environ. Sci. Pollut. Res.*, 2022, **29**, 46003–46017.
45 U. Arisekar, R. J. Shakila, R. Shalini, G. Jeyasekaran and P. Padmavathy, *Chemosphere*, 2022, **297**, 134075.
46 F. Aydın and M. Albay, *Environ. Monit. Assess.*, 2022, **194**, 1–17.
47 U. Al-Mulali, I. Ozturk and H. H. Lean, *Nat. Hazards Res.*, 2015, **79**, 621–644.

Open Access Article. Published on 02 September 2025. Downloaded on 11/10/2025 5:56:01 AM.
This article is licensed under a Creative Commons Attribution-NonCommercial 3.0 Unported Licence.

48 T. Bakirtas and A. G. Akpolat, *Energy*, 2018, **147**, 110–121.
49 B. Liu, W. Niu, X. Hu, F. Liu, J. Jiang, H. Wang and S. Wang, *Chem. Eng. J.*, 2022, **434**, 134631.
50 Z. Pilková, E. Hiller, L. Filová and Ľ. Jurkovič, *Environ. Geochem. Health*, 2022, **44**, 3473–3492.
51 *PAH Analysis|Overview of Requirements in the EU|Measurlabs*, https://measurlabs.com/blog/pah-analysis/, accessed 15 April 2025.
52 B. Bukowska, K. Mokra and J. Michałowicz, *Int. J. Mol. Sci.*, 2022, **23**, 6348.
53 *Fact sheet: Benzo anthracene—Guidance and Orientation for the Selection of Technologies—Contaminated sites—Pollution and waste management—Environment and natural resources—Canada.ca*, https://gost.tpsgc-pwgsc.gc.ca/Contfs.aspx?ID=32&lang=eng, accessed 1 May 2025.
54 *ICSC 0720 – BENZO(b)fluoranthene*, https://www.inchem.org/documents/icsc/icsc/eics0720.htm, accessed 1 May 2025.
55 E. Stogiannidis and R. Laane, *Rev. Environ. Contam. Toxicol.*, 2015, **234**, 49–133.
56 National Centre for Biotechnology Information (NCBI), *Benzo[e]pyrene*, PuChem Compound Summery, 2021.
57 V. Garg, *Acta Cienc. Indica*, 2017, 75–81.
58 C. Fortin and D. Caldbick, *Organohalogen Compd.*, 1997, **32**, 417–429.
59 R. E. Alcock, R. Gemmill and K. C. Jones, *Chemosphere*, 1999, **38**, 759–770.
60 H. Fiedler, *Organohalogen Compd*, 1993, **11**, 221–228.
61 A. Haleem, M. Ullah, S. ur Rehman, A. Shah, M. Farooq, T. Saeed, I. Ullah and H. Li, *Water*, 2024, **16**, 1588.
62 A. P. Periyasamy, *Sustainability*, 2024, **16**, 495.
63 Y. Xing, Y. Lu, R. W. Dawson, Y. Shi, H. Zhang, T. Wang, W. Liu and H. Ren, *Chemosphere*, 2005, **60**, 731–739.
64 T. Wenzl, R. Simon, E. Anklam and J. Kleiner, *TrAC, Trends Anal. Chem.*, 2006, **25**, 716–725.
65 P. Kumari, N. Bahadur and L. F. Dumée, *Sep. Purif. Technol.*, 2020, **230**, 115878.
66 A. Raj, A. Kumar and J. F. Dames, *Front. Microbiol.*, 2021, **12**, 791723.
67 B. B. Gaitonde, *Insectic. Act.*, 1968, 157–179.
68 P. I. Devi, J. Thomas and R. K. Raju, *Agric. Econ. Res. Rev.*, 2017, **30**, 163.
69 A. Gulati, S. Jain and N. Satija, *J. Land Rural Stud.*, 2014, **2**, 261–286.
70 D. Santillo, R. L. Stringer and P. A. Johnston, Greenpeace Research Laboratories, Department of Biological University of Exeter, Reino Unido, 2000.
71 H. Bouwman, *Persistent Org. Pollut.*, 2003, 297–320.
72 M. H. Wong and B. H. T. Poon, *Persistent Org. Pollut.*, 2003, 355–369.
73 K. Czaja, J. K. Ludwicki, K. Góralczyk and P. Struciński, *Bull. Environ. Contam. Toxicol.*, 1997, **59**, 407–413.
74 S. Benkhaya, S. M'rabet and A. El Harfi, *Inorg. Chem. Commun.*, 2020, **115**, 107891.
75 D. A. Yaseen and M. Scholz, *Int. J. Environ. Sci. Technol.*, 2019, **16**, 1193–1226.
76 S. Dutta, B. Gupta, S. K. Srivastava and A. K. Gupta, *Mater. Adv.*, 2021, **2**, 4497–4531.
77 A. Kumar, B. S. Bisht, V. D. Joshi, A. K. Singh and A. Talwar, *J. Hum. Ecol.*, 2010, **32**, 169–173.
78 D. G. J. Larsson, C. de Pedro and N. Paxeus, *J. Hazard. Mater.*, 2007, **148**, 751–755.
79 L. Ritter, K. R. Solomon, J. Forget, M. Stemeroff and C. O'leary, *International Programme on Chemical Safety (IPCS), PCS/95.39*, World Health Organization, Geneva, 1995.
80 J. Buccini, *Persistent Org. Pollut.*, 2003, 13–30.
81 G. Zhao, Y. Xu, G. Han and B. Ling, *Environ. Geochem. Health*, 2006, **28**, 341–351.
82 P. Fernández and J. O. Grimalt, *Chimia*, 2003, **57**, 514.
83 P. Fernández and J. O. Grimalt, *Chimia*, 2003, **57**, 514.
84 P. Fernández and J. O. Grimalt, *Chimia*, 2003, **57**, 514.
85 R. Sadler and D. Connell, in *Organic Pollutants Ten Years after the stockholm convention—environmental and Analytical Update*, InpTech, 2012, pp. 191–216.
86 S. L. Simonich and R. A. Hites, *Science*, 1995, **269**, 1851–1854.
87 D. Calamari, E. Bacci, S. Focardi, C. Gaggi, M. Morosini and M. Vighl, *Environ. Sci. Technol.*, 1991, **25**, 1489–1495.
88 C. Agrell, L. Okla, P. Larsson, C. Backe and F. Wania, *Environ. Sci. Technol.*, 1999, **33**, 1149–1156.
89 D. C. G. Muir, A. Omelchenko, N. P. Grift, D. A. Savoie, W. L. Lockhart, P. Wilkinson and G. J. Brunskill, *Environ. Sci. Technol.*, 1996, **30**, 3609–3617.
90 H. Iwata, S. Tanabe, N. Sakai, A. Nishimura and R. Tatsukawa, *Environ. Pollut.*, 1994, **85**, 15–33.
91 S. N. Meijer, E. Steinnes, W. A. Ockenden and K. C. Jones, *Environ. Sci. Technol.*, 2002, **36**, 2146–2153.
92 S. N. Meijer, W. A. Ockenden, A. Sweetman, K. Breivik, J. O. Grimalt and K. C. Jones, *Environ. Sci. Technol.*, 2003, **37**, 667–672.
93 M. G. Ikonomou, S. Rayne and R. F. Addison, *Environ. Sci. Technol.*, 2002, **36**, 1886–1892.
94 F. Wania and D. MacKay, *Environ. Sci. Technol.*, 2011, **30**, 390A–396A.
95 M. Scheringer, *Environ. Toxicol. Chem.*, 2009, **28**, 677–690.
96 A. J. Sweetman, M. D. Valle, K. Prevedouros and K. C. Jones, *Chemosphere*, 2005, **60**, 959–972.
97 S. Guillotin and N. Delcourt, *Int. J. Mol. Sci.*, 2022, **23**, 14271.
98 A. Katsoyiannis and C. Samara, *Environ. Res.*, 2005, **97**, 245–257.
99 A. Pauwels, A. Covaci, J. Weyler, L. Delbeke, M. Dhont, P. De Sutter, T. D'Hooghe and P. J. C. Schepens, *Arch. Environ. Contam. Toxicol.*, 2000, **39**, 265–270.
100 O. Roots, V. Zitko and A. Roose, *Chemosphere*, 2005, **60**, 914–921.
101 T. Damstra, S. W. Page, J. L. Herrman and T. Meredith, *Br. J. Prev. Soc. Med.*, 2002, **56**, 824–825.
102 J. A. McLachlan and S. F. Arnold, *Am. Sci.*, 1996, **84**, 452–461.
103 J. L. Jacobson, S. W. Jacobson and H. E. B. Humphrey, *J. Pediatr.*, 1990, **116**, 38–45.

 © 2025 The Author(s). Published by the Royal Society of Chemistry

Open Access Article. Published on 02 September 2025. Downloaded on 11/10/2025 5:56:01 AM.
This article is licensed under a Creative Commons Attribution-NonCommercial 3.0 Unported Licence.

104 J. L. Jacobson, S. W. Jacobson and H. E. B. Humphrey, *Neurotoxicol. Teratol.*, 1990, **12**, 319–326.
105 P. Langer, A. Kočan, M. Tajtaková, J. Petrík, J. Chovancová, B. Drobná, S. Jursa, Ž. Rádiková, J. Koška, L. Kšinantová, M. Hučková, R. Imrich, S. Wimmerová, D. Gašperíková, Y. Shishiba, T. Trnovec, E. Šeböková and I. Klimeš, *Chemosphere*, 2007, **67**, S379–S385.
106 M. Gao and N. xiang Wu, *Zhonghua Nankexue*, 2011, **17**, 448–452.
107 E. Vizcaino, J. O. Grimalt, A. Fernández-Somoano and A. Tardon, *Environ. Int.*, 2014, **65**, 107–115.
108 L. Kvist, A. Giwercman, P. Weihe, T. Kold Jensen, P. Grandjean, J. Halling, M. Skaalum Petersen and Y. Lundberg Giwercman, *Environ. Int.*, 2014, **73**, 359–364.
109 I. Ali, W. A. Wani and K. Saleem, *Cancer Ther.*, 2011, **8**, 56–70.
110 S. A. Ljunggren, I. Helmfrid, S. Salihovic, B. van Bavel, G. Wingren, M. Lindahl and H. Karlsson, *Environ. Int.*, 2014, **65**, 93–99.
111 R. Barouki, *Annee Endocrinol.*, 2013, **74**, 154–155.
112 S. O. Fredslund and E. C. Bonefeld-Jørgensen, *Int. J. Circumpolar Health*, 2012, **71**, 19155.
113 C. Hiremath, D. Bayliss and S. Bayard, *Chemosphere*, 1986, **15**, 1815–1823.
114 H. Y. Yu, Y. Guo and E. Y. Zeng, *Environ. Toxicol. Chem.*, 2010, **29**, 2135–2142.
115 J. P. Arrebola, M. F. Fernández, P. Martín-Olmedo, J. M. Molina-Molina, M. J. Sánchez-Pérez, E. Sánchez-Cantalejo, E. Molina-Portillo, J. Expósito, J. P. Bonde and N. Olea, *Sci. Total Environ.*, 2014, **500–501**, 243–249.
116 J. P. Arrebola, R. Ocaña-Riola, A. L. Arrebola-Moreno, M. Fernández-Rodríguez, P. Martin-Olmedo, M. F. Fernández and N. Olea, *Environ. Pollut.*, 2014, **195**, 9–15.
117 V. Mathur, P. Bhatnagar, R. G. Sharma, V. Acharya and R. Sexana, *Environ. Int.*, 2002, **28**, 331–336.
118 S. Goldstein, *Cardiovasc. Drugs Ther.*, 1997, **11**, 219–225.
119 D. H. Lee, P. M. Lind, D. R. Jacobs, S. Salihovic, B. Van Bavel and L. Lind, *Diabetes Care*, 2011, **34**, 1778–1784.
120 B. Valera, M. E. Jørgensen, C. Jeppesen and P. Bjerregaard, *Environ. Res.*, 2013, **122**, 65–73.
121 D. Pelclová, P. Urban, J. Preiss, E. Lukáš, Z. Fenclová, T. Navrátil, Z. Dubská and Z. Šenholdova, *Rev. Environ. Health*, 2006, **21**, 119–138.
122 T. Damstra, *J. Toxicol., Clin. Toxicol.*, 2002, **40**, 457–465.
123 M. Camacho, O. P. Luzardo, L. D. Boada, L. F. López Jurado, M. Medina, M. Zumbado and J. Orós, *Sci. Total Environ.*, 2013, **458–460**, 283–289.
124 L. M. Schell, K. K. Burnitz and P. W. Lathrop, *Ann. Hum. Biol.*, 2010, **37**, 347–366.
125 L. M. Schell, *Am. J. Phys. Anthropol.*, 1991, **34**, 157–188.
126 D. O. Carpenter, *Rev. Environ. Health*, 2011, **26**, 61–69.
127 S. A. DiVall, *Curr. Opin. Endocrinol., Diabetes Obes.*, 2013, **20**, 50–55.
128 J. Falandysz, A. Fernandes, E. Gregoraszczuk and M. Rose, *J. Environ. Sci. Health, Part C*, 2014, **32**, 239–272.
129 Q. Q. Li, A. Loganath, Y. S. Chong, J. Tan and J. P. Obbard, *J. Toxicol. Environ. Health, Part A*, 2006, **69**, 1987–2005.
130 M. Montaño, A. C. Gutleb and A. J. Murk, *Environ. Sci. Technol.*, 2013, **47**, 6071–6081.
131 A. Pawełczyk, *Environ. Monit. Assess.*, 2013, **185**, 497–508.
132 K. E. Pedersen, B. Styrishave, C. Sonne, R. Dietz and B. M. Jenssen, *Sci. Total Environ.*, 2015, **502**, 510–516.
133 J. Ruzzin, *BMC Public Health*, 2012, **12**, 1–8.
134 H. Tounsadi, Y. Metarfi, M. Taleb, K. El Rhazi and Z. Rais, *Ecotoxicol. Environ. Saf.*, 2020, **197**, 110594.
135 R. Al-Tohamy, S. S. Ali, F. Li, K. M. Okasha, Y. A. G. Mahmoud, T. Elsamahy, H. Jiao, Y. Fu and J. Sun, *Ecotoxicol. Environ. Saf.*, 2022, **231**, 113160.
136 L. Wu, Y. Xu, X. Lv, X. Chang, X. Ma, X. Tian, X. Shi, X. Li and X. Kong, *Ecotoxicol. Environ. Saf.*, 2021, **223**, 112551.
137 S. Lacombe and N. Keller, *Environ. Sci. Pollut. Res.*, 2012, **19**, 3651–3654.
138 D. Beydoun, R. Amal, G. Low and S. McEvoy, *J. Nanopart. Res.*, 1999, **1**, 439–458.
139 M. Han, S. Zhu, S. Lu, Y. Song, T. Feng, S. Tao, J. Liu and B. Yang, *Nano Today*, 2018, **19**, 201–218.
140 M. M. Haque, D. Bahnemann and M. Muneer, in *Organic Pollutants Ten Years after the Stockholm Convention–Environmental and Analytical Update*, IntechOpen, London, UK, 2012, vol. 293.
141 J. M. Poyatos, M. M. Muñio, M. C. Almecija, J. C. Torres, E. Hontoria and F. Osorio, *Water, Air, Soil Pollut.*, 2010, **205**, 187–204.
142 S. M. Rodríguez, *Innovative Processes and Practices for Wastewater Treatment and Re-use*, Ankara University, Turkey, 2007.
143 J. Schneider, D. Bahnemann, J. Ye, G. L. Puma and D. D. Dionysiou, *Photocatalysis: Fundamentals and Perspectives*, The Royal Society of Chemistry, 2016, vol. 14.
144 D. K. Mohammad Reza, M. S. Shafeeyan, A. R. Abdul Aziz and A. W. D. Wan Mohd, *J. Environ. Manage.*, 2017, **198**, 78–94.
145 A. O. Ibhadon and P. Fitzpatrick, *Catalysts*, 2013, **3**, 189–218.
146 A. Fujishima, X. Zhang and D. A. Tryk, *Int. J. Hydrogen Energy*, 2007, **32**, 2664–2672.
147 C. S. Turchi and D. F. Ollis, *J. Catal.*, 1990, **122**, 178–192.
148 M. Grätzel, *Heterog. Photochem. Electron Transf.*, 2018, 1–159.
149 M. M. Haque and M. Muneer, *J. Environ. Manage.*, 2003, **69**, 169–176.
150 J. Hupka, A. Zaleska, M. Janczarek, E. Kowalska, P. Górska and R. Aranowski, *Soil Water Pollut. Monit. Prot. Remediat.*, 2006, 351–367.
151 S. Baruah, M. A. Mahmood, M. T. Z. Myint, T. Bora and J. Dutta, *Beilstein J. Nanotechnol.*, 2010, **1**, 14–20.
152 M. Schiavello, *Photoelectrochemistry, Photocatalysis and Photoreactors Fundamentals and Developments*, Springer Science & Business Media, 2013, vol. 146.
153 D. Durgalakshmi, R. Ajay Rakkesh, S. Rajendran and M. Naushad, *Green Photocatalysts*, Springer International Publishing, 2019, pp. 1–18.

Open Access Article. Published on 02 September 2025. Downloaded on 11/10/2025 5:56:01 AM.
This article is licensed under a Creative Commons Attribution-NonCommercial 3.0 Unported Licence.

154 D. Chatterjee and S. Dasgupta, *J. Photochem. Photobiol., C*, 2005, **6**, 186–205.
155 J. M. Herrmann, *Catal. Today*, 1999, **53**, 115–129.
156 S. Ahmed, M. G. Rasul, R. Brown and M. A. Hashib, *J. Environ. Manage.*, 2011, **92**, 311–330.
157 U. I. Gaya and A. H. Abdullah, *J. Photochem. Photobiol., C*, 2008, **9**, 1–12.
158 U. G. Akpan and B. H. Hameed, *J. Hazard. Mater.*, 2009, **170**, 520–529.
159 J. Schneider, M. Matsuoka, M. Takeuchi, J. Zhang, Y. Horiuchi, M. Anpo and D. W. Bahnemann, *Chem. Rev.*, 2014, **114**, 9919–9986.
160 Z. You, D. Lu, K. K. Kondamareddy, W. Gu, Y. Su, J. Pan, J. Yang, P. Cheng and W. Ho, *Sep. Purif. Technol.*, 2025, **361**, 131293.
161 C. M. Teh and A. R. Mohamed, *J. Alloys Compd.*, 2011, **509**, 1648–1660.
162 A. R. Khataee and M. B. Kasiri, *J. Mol. Catal. A:Chem.*, 2010, **328**, 8–26.
163 T. Aarthi, P. Narahari and G. Madras, *J. Hazard. Mater.*, 2007, **149**, 725–734.
164 E. R. Bandala, S. Gelover, M. T. Leal, C. Arancibia-Bulnes, A. Jimenez and C. A. Estrada, *Catal. Today*, 2002, **76**, 189–199.
165 B. Yu, J. Zeng, L. Gong, X. Yang, L. Zhang and X. Chen, *Chin. Sci. Bull.*, 2008, **53**, 27–32.
166 J. Thomas, K. P. Kumar and K. R. Chitra, *Adv. Sci. Lett.*, 2011, **4**, 108–114.
167 H. S. Kim, J. W. Lee, N. Yantara, P. P. Boix, S. A. Kulkarni, S. Mhaisalkar, M. Grätzel and N. G. Park, *Nano Lett.*, 2013, **13**, 2412–2417.
168 K. M. Lee, C. W. Lai, K. S. Ngai and J. C. Juan, *Water Res.*, 2016, **88**, 428–448.
169 S. Roy, S. R. Mishra, V. Gadore and M. Ahmaruzzaman, *Int. J. Environ. Anal. Chem.*, 2024, 1–13.
170 S. Maiti, S. Pal and K. K. Chattopadhyay, *CrystEngComm*, 2015, **17**, 9264–9295.
171 N. Daneshvar, D. Salari and A. R. Khataee, *J. Photochem. Photobiol., A*, 2004, **162**, 317–322.
172 C. Hariharan, *Appl. Catal., A*, 2006, **304**, 55–61.
173 N. Sasikala Reddy, N. Lokeswara Reddy, S. Monica Nissy, G. Pallavi and M. Vangalapati, *Mater. Today: Proc.*, 2020, **26**, 1694–1700.
174 M. M. Ba-Abbad, A. A. H. Kadhum, A. B. Mohamad, M. S. Takriff and K. Sopian, *Chemosphere*, 2013, **91**, 1604–1611.
175 F. T. Geldasa, M. A. Kebede, M. W. Shura and F. G. Hone, *RSC Adv.*, 2023, **13**, 18404–18442.
176 Y. Lu, Y. Lin, D. Wang, L. Wang, T. Xie and T. Jiang, *Nano Res.*, 2011, **4**, 1144–1152.
177 I. Ahmad, M. Aslam, U. Jabeen, M. N. Zafar, M. N. K. Malghani, N. Alwadai, F. H. Alshammari, A. S. Almuslem and Z. Ullah, *Inorg. Chim. Acta*, 2022, **543**, 121167.
178 S. P. Kim, M. Y. Choi and H. C. Choi, *Mater. Res. Bull.*, 2016, **74**, 85–89.
179 S. R. Mishra and M. Ahmaruzzaman, *Nanoscale*, 2022, **14**, 1566–1605.
180 J. Fang, X. Xu, Y. Yang, Z. Han, Z. Zuo, W. Han and B. Lin, *J. Therm. Anal. Calorim.*, 2025, **150**, 7335–7347.
181 Y. Li, Q. Yang, Z. Wang, G. Wang, B. Zhang, Q. Zhang and D. Yang, *Inorg. Chem. Front.*, 2018, **5**, 3005–3014.
182 S. K. Tammina and B. K. Mandal, *J. Mol. Liq.*, 2016, **221**, 415–421.
183 S. Wu, H. Cao, S. Yin, X. Liu and X. Zhang, *J. Phys. Chem. C*, 2009, **113**, 17893–17898.
184 G. Sangami and N. Dharmaraj, *Spectrochim. Acta, Part A*, 2012, **97**, 847–852.
185 A. Diallo, E. Manikandan, V. Rajendran and M. Maaza, *J. Alloys Compd.*, 2016, **681**, 561–570.
186 E. Haritha, S. M. Roopan, G. Madhavi, G. Elango, N. A. Al-Dhabi and M. V. Arasu, *J. Photochem. Photobiol., B*, 2016, **162**, 441–447.
187 G. Yadav, S. R. Mishra, V. Gadore, N. Yadav and M. Ahmaruzzaman, *Sci. Rep.*, 2023, **13**, 1–21.
188 O. Akhavan and R. Azimirad, *Appl. Catal., A*, 2009, **369**, 77–82.
189 W. Feng, D. Nansheng and H. Helin, *Chemosphere*, 2000, **41**, 1233–1238.
190 M. H. Khedr, K. S. Abdel Halim and N. K. Soliman, *Mater. Lett.*, 2009, **63**, 598–601.
191 A. R. A. Giwa, I. A. Bello, A. B. Olabintan, O. S. Bello and T. A. Saleh, *Heliyon*, 2020, **6**, e04454.
192 M. Haris, A. Zavabeti, M. W. Khan, B. J. Murdoch, J. Paz-Ferreiro, N. Mahmood and N. Eshtiaghi, *J. Environ. Chem. Eng.*, 2022, **10**, 108968.
193 N. Li, Y. Jiang, Y. long He, L. Gao, Z. zhou Yi, F. rui Zhai and K. Chattopadhyay, *J. Mater. Res. Technol.*, 2021, **15**, 810–820.
194 A. W. Jansons, K. M. Koskela, B. M. Crockett and J. E. Hutchison, *Chem. Mater.*, 2017, **29**, 8167–8176.
195 V. Subramanian, E. Wolf and P. V. Kamat, *J. Phys. Chem. B*, 2001, **105**, 11439–11446.
196 A. Hezam, K. Namratha, D. Ponnamma, Q. A. Drmosh, A. M. N. Saeed, K. K. Sadasivuni and K. Byrappa, *ACS Omega*, 2019, **4**, 20595–20605.
197 R. Satheesh, K. Vignesh, A. Suganthi and M. Rajarajan, *J. Environ. Chem. Eng.*, 2014, **2**, 1956–1968.
198 A. N. Cheema, I. Muneer, Maham, F. Yasmeen and D. Ali, *Mater. Sci. Eng., B*, 2025, **312**, 117878.
199 M. A. Butler, R. D. Nasby and R. K. Quinn, *Solid State Commun.*, 1976, **19**, 1011–1014.
200 M. S. S. Danish, L. L. Estrella, I. M. A. Alemaida, A. Lisin, N. Moiseev, M. Ahmadi, M. Nazari, M. Wali, H. Zaheb and T. Senjyu, *Metals*, 2021, **11**, 80.
201 C. Wang, X. Li, C. Feng, Y. Sun and G. Lu, *Sens. Actuators, B*, 2015, **210**, 75–81.
202 J. Theerthagiri, S. Chandrasekaran, S. Salla, V. Elakkiya, R. A. Senthil, P. Nithyadharseni, T. Maiyalagan, K. Micheal, A. Ayeshamariam, M. V. Arasu, N. A. Al-Dhabi and H. S. Kim, *J. Solid State Chem.*, 2018, **267**, 35–52.
203 M. B. Tahir, G. Nabi, M. Rafique and N. R. Khalid, *Int. J. Environ. Sci. Technol.*, 2017, **14**, 2519–2542.

 © 2025 The Author(s). Published by the Royal Society of Chemistry

Open Access Article. Published on 02 September 2025. Downloaded on 11/10/2025 5:56:01 AM.
This article is licensed under a Creative Commons Attribution-NonCommercial 3.0 Unported Licence.

204 V. Gokila, S. Ayyappan, P. Muthukrishnan, T. Brindha and J. J. David, *Res. Chem. Intermed.*, 2025, 1–23.
205 M. Muthukumaran, G. Gnanamoorthy, P. Varun Prasath, M. Abinaya, G. Dhinagaran, S. Sagadevan, F. Mohammad, W. C. Oh and K. Venkatachalam, *Mater. Res. Express*, 2020, **7**, 015038.
206 S. O. Adewuyi, D. Malomo, S. M. Nelana, M. J. Klink and O. S. Ayanda, *Water Conserv. Manag.*, 2024, **8**, 274–283.
207 N. T. Khan and N. Jameel, *Acta Sci. Pharm. Sci.*, 2018, **2**, 41–43.
208 V. K. Mrunal, A. K. Vishnu, N. Momin and J. Manjanna, *Environ. Nanotechnol., Monit. Manage.*, 2019, **12**, 100265.
209 A. Kerour, S. Boudjadar, R. Bourzami and B. Allouche, *J. Solid State Chem.*, 2018, **263**, 79–83.
210 A. M. Mohammed, S. S. Mohtar, F. Aziz, S. A. Mhamad and M. Aziz, *J. Environ. Chem. Eng.*, 2021, **9**, 105138.
211 S. Sukumar, A. Rudrasenan and D. Padmanabhan Nambiar, *ACS Omega*, 2020, **5**, 1040–1051.
212 S. R. Mishra and M. Ahmaruzzaman, *Sustainable Mater. Technol.*, 2022, **33**, e00463.
213 R. Gusain, K. Gupta, P. Joshi and O. P. Khatri, *Adv. Colloid Interface Sci.*, 2019, **272**, 102009.
214 F. T. Geldasa, M. A. Kebede, M. W. Shura and F. G. Hone, *RSC Adv.*, 2023, **13**, 18404–18442.
215 R. Banu, N. Salvi, S. Gupta, C. Ameta, R. Ameta and P. B. Punjabi, *Arabian J. Sci. Eng.*, 2022, **47**, 365–378.
216 A. A. M. Sakib, S. M. Masum, J. Hoinkis, R. Islam and M. A. I. Molla, *J. Compos. Sci.*, 2019, **3**, 91.
217 D. Malwal and P. Gopinath, *Catal. Sci. Technol.*, 2016, **6**, 4458–4472.
218 A. George, D. Magimai Antoni Raj, X. Venci, A. Dhayal Raj, A. Albert Irudayaraj, R. L. Josephine, S. John Sundaram, A. M. Al-Mohaimeed, D. A. Al Farraj, T. W. Chen and K. Kaviyarasu, *Environ. Res.*, 2022, **203**, 111880.
219 A. H. Zahid and Q. Han, *Nanoscale*, 2021, **13**, 17687–17724.
220 T. Li, S. Quan, X. Shi, L. Yang and C. Liu, *Catal. Lett.*, 2020, **150**, 640–651.
221 D. Guin, B. Baruwati and S. V. Manorama, *J. Mol. Catal. A:Chem.*, 2005, **242**, 26–31.
222 L. Zhenmin, L. Xiaoyong, W. Hong, M. Dan, X. Chaojian and W. Dan, *J. Phys. Chem. C*, 2009, **113**, 2792–2797.
223 N. Zhang, B. Wang, P. Hu, Z. Gao and H. Wang, *J. Environ. Chem. Eng.*, 2025, **13**, 115800.
224 R. Dom, R. Subasri, K. Radha and P. H. Borse, *Solid State Commun.*, 2011, **151**, 470–473.
225 E. Casbeer, V. K. Sharma and X. Z. Li, *Sep. Purif. Technol.*, 2012, **87**, 1–14.
226 Z. Liu, Z. G. Zhao and M. Miyauchi, *J. Phys. Chem. C*, 2009, **113**, 17132–17137.
227 Y. Ao, J. Xu, D. Fu, X. Shen and C. Yuan, *Sep. Purif. Technol.*, 2008, **61**, 436–441.
228 J. Asokan, P. Kumar, G. Arjunan and M. G. Shalini, *J. Cluster Sci.*, 2025, **36**, 1–42.
229 X. Cao, L. Gu, X. Lan, C. Zhao, D. Yao and W. Sheng, *Mater. Chem. Phys.*, 2007, **106**, 175–180.
230 H. Anwer, A. Mahmood, J. Lee, K. H. Kim, J. W. Park and A. C. K. Yip, *Nano Res.*, 2019, **12**, 955–972.
231 I. Ahmad, Y. Zou, J. Yan, Y. Liu, S. Shukrullah, M. Y. Naz, H. Hussain, W. Q. Khan and N. R. Khalid, *Adv. Colloid Interface Sci.*, 2023, **311**, 102830.
232 F. Huang, A. Yan and H. Zhao, *Semicond. Photocatal.:Mater., Mech. Appl.*, 2016, 31–80.
233 C. Han, V. Likodimos, J. A. Khan, M. N. Nadagouda, J. Andersen, P. Falaras, P. Rosales-Lombardi and D. D. Dionysiou, *Environ. Sci. Pollut. Res.*, 2014, **21**, 11781–11793.
234 Q. Fang, Q. Sun, R. Zhong, H. Wang and J. Qi, *Mater. Today Chem.*, 2025, **46**, 102770.
235 A. Zaleska, *Recent Pat. Eng.*, 2008, **2**, 157–164.
236 M. Mangayayam, J. Kiwi, S. Giannakis, C. Pulgarin, I. Zivkovic, A. Magrez and S. Rtimi, *Appl. Catal., B*, 2017, **202**, 438–445.
237 D. Chen, Z. Jiang, J. Geng, Q. Wang and D. Yang, *Ind. Eng. Chem. Res.*, 2007, **46**, 2741–2746.
238 N. Sakaguchi Miyamoto, R. Miyamoto, E. Giamello, T. Kurisaki and H. Wakita, *Res. Chem. Intermed.*, 2018, **44**, 4577–4594.
239 V. O. Ndabankulu, S. Maddila and S. B. Jonnalagadda, *Can. J. Chem.*, 2019, **97**, 672–681.
240 S. Sood, A. Umar, S. K. Mehta and S. K. Kansal, *J. Colloid Interface Sci.*, 2015, **450**, 213–223.
241 V. Likodimos, C. Han, M. Pelaez, A. G. Kontos, G. Liu, D. Zhu, S. Liao, A. A. De La Cruz, K. O'Shea, P. S. M. Dunlop, J. A. Byrne, D. D. Dionysiou and P. Falaras, *Ind. Eng. Chem. Res.*, 2013, **52**, 13957–13964.
242 Y. Cong, J. Zhang, F. Chen and M. Anpo, *J. Phys. Chem. C*, 2007, **111**, 6976–6982.
243 J. Senthilnathan and L. Philip, *Chem. Eng. J.*, 2010, **161**, 83–92.
244 D. Zhang, G. Li and J. C. Yu, *J. Mater. Chem.*, 2010, **20**, 4529–4536.
245 Y. Luan, P. F. Fu and X. G. Dai, *Solid State Phenom.*, 2007, **121–123**, 239–242.
246 S. Ramandi, M. H. Entezari and N. Ghows, *Ultrason. Sonochem.*, 2017, **38**, 234–245.
247 G. Dong, Y. Wang, H. Lei, G. Tian, S. Qi and D. Wu, *J. Cleaner Prod.*, 2020, **253**, 120021.
248 T. Suwannaruang, J. P. Hildebrand, D. H. Taffa, M. Wark, K. Kamonsuangkasem, P. Chirawatkul and K. Wantala, *J. Photochem. Photobiol., A*, 2020, **391**, 112371.
249 L. Li, W. Chang, Y. Wang, H. Ji, C. Chen, W. Ma and J. Zhao, *Chem.–Eur. J.*, 2014, **20**, 11163–11170.
250 M. Lei, N. Wang, L. Zhu and H. Tang, *Chemosphere*, 2016, **150**, 536–544.
251 R. Wang, T. Tang, Y. Wei, D. Dang, K. Huang, X. Chen, H. Yin, X. Tao, Z. Lin, Z. Dang and G. Lu, *Environ. Int.*, 2019, **127**, 5–12.
252 W. Xie, R. Li and Q. Xu, *Sci. Rep.*, 2018, **81**(8), 1–10.
253 P. Karuppasamy, N. Ramzan Nilofar Nisha, A. Pugazhendhi, S. Kandasamy and S. Pitchaimuthu, *J. Environ. Chem. Eng.*, 2021, **9**, 105254.
254 A. Khlyustova, N. Sirotkin, T. Kusova, A. Kraev, V. Titov and A. Agafonov, *Mater. Adv.*, 2020, **1**, 1193–1201.

Open Access Article. Published on 02 September 2025. Downloaded on 11/10/2025 5:56:01 AM. This article is licensed under a Creative Commons Attribution-NonCommercial 3.0 Unported Licence.

255 S. Saroj, L. Singh and S. V. Singh, *J. Photochem. Photobiol., A*, 2020, **396**, 112532.
256 Z. Ji, Z. Luo, J. Li and P. Li, *Phys. Status Solidi A*, 2019, **216**, 1800947.
257 U. Alam, A. Khan, D. Ali, D. Bahnemann and M. Muneer, *RSC Adv.*, 2018, **8**, 17582–17594.
258 Z. Mirzaeifard, Z. Shariatinia, M. Jourshabani and S. M. Rezaei Darvishi, *Ind. Eng. Chem. Res.*, 2020, **59**, 15894–15911.
259 M. C. Uribe-López, M. C. Hidalgo-López, R. López-González, D. M. Frías-Márquez, G. Núñez-Nogueira, D. Hernández-Castillo and M. A. Alvarez-Lemus, *J. Photochem. Photobiol., A*, 2021, **404**, 112866.
260 K. Qi, X. Xing, A. Zada, M. Li, Q. Wang, S. yuan Liu, H. Lin and G. Wang, *Ceram. Int.*, 2020, **46**, 1494–1502.
261 S. Ramkumar and G. Rajarajan, *Appl. Phys. A: Mater. Sci. Process.*, 2017, **123**, 1–8.
262 M. Desseigne, V. Madigou, M. V. Coulet, O. Heintz, V. Chevallier and M. Arab, *J. Photochem. Photobiol., A*, 2023, **437**, 114427.
263 F. Han, H. Li, L. Fu, J. Yang and Z. Liu, *Chem. Phys. Lett.*, 2016, **651**, 183–187.
264 M. Qamar, Z. H. Yamani, M. A. Gondal and K. Alhooshani, *Solid State Sci.*, 2011, **13**, 1748–1754.
265 I. Firdaus, A. Purwanto and H. Widiyandari, *Adv. Mater. Res.*, 2015, **1112**, 188–193.
266 R. Sasikala, K. Karthikeyan, D. Easwaramoorthy, I. M. Bilal and S. K. Rani, *Environ. Nanotechnol., Monit. Manage.*, 2016, **6**, 45–53.
267 S. J. Singh and P. Chinnamuthu, *Colloids Surf., A*, 2021, **625**, 126864.
268 L. Vimala Devi, S. Sellaiyan, T. Selvalakshmi, H. J. Zhang, A. Uedono, K. Sivaji and S. Sankar, *Adv. Powder Technol.*, 2017, **28**, 3026–3038.
269 D. Masekela, L. K. Kganyakgo, K. D. Modibane, T. L. Yusuf, S. A. Balogun, W. M. Seleka and E. Makhado, *Results Chem.*, 2025, **13**, 101971.
270 T. Jiang, J. Kong, Y. Wang, D. Meng, D. Wang and M. Yu, *Cryst. Res. Technol.*, 2016, **51**, 58–64.
271 R. Arunadevi, B. Kavitha, M. Rajarajan, A. Suganthi and A. Jeyamurugan, *Surf. Interfaces*, 2018, **10**, 32–44.
272 K. Vinodgopal and P. V. Kamat, *Environ. Sci. Technol.*, 1995, **29**, 841–845.
273 K. T. Ranjit and B. Viswanathan, *J. Photochem. Photobiol., A*, 1997, **108**, 79–84.
274 K. Prakruthi, M. P. Ujwal, S. R. Yashas, B. Mahesh, N. Kumara Swamy and H. P. Shivaraju, *Environ. Sci. Pollut. Res.*, 2021, **29**, 4930–4957.
275 H. Zhou, Y. Qu, T. Zeid and X. Duan, *Energy Environ. Sci.*, 2012, **5**, 6732–6743.
276 J. Low, J. Yu, M. Jaroniec, S. Wageh and A. A. Al-Ghamdi, *Adv. Mater.*, 2017, **29**, 1601694.
277 R. Marschall, *Adv. Funct. Mater.*, 2014, **24**, 2421–2440.
278 S. J. A. Moniz, S. A. Shevlin, D. J. Martin, Z. X. Guo and J. Tang, *Energy Environ. Sci.*, 2015, **8**, 731–759.
279 J. K. Hyun, S. Zhang and L. J. Lauhon, *Annu. Rev. Mater. Res.*, 2013, **43**, 451–479.
280 W. Shi and N. Chopra, *Nanomater. Energy*, 2013, **2**, 158–178.
281 L. Xie, T. Du, J. Wang, Y. Ma, Y. Ni, Z. Liu, L. Zhang, C. Yang and J. Wang, *Chem. Eng. J.*, 2021, **426**, 130617.
282 Y. Bessekhouad, D. Robert and J. V. Weber, *J. Photochem. Photobiol., A*, 2004, **163**, 569–580.
283 E. Mugunthan, M. B. Saidutta and P. E. Jagadeeshbabu, *J. Photochem. Photobiol., A*, 2019, **383**, 111993.
284 S. A. K. Leghari, S. Sajjad, F. Chen and J. Zhang, *Chem. Eng. J.*, 2011, **166**, 906–915.
285 S. Bai, K. Zhang, J. Sun, R. Luo, D. Li and A. Chen, *CrystEngComm*, 2014, **16**, 3289–3295.
286 Y. P. Yuan, L. W. Ruan, J. Barber, S. C. Joachim Loo and C. Xue, *Energy Environ. Sci.*, 2014, **7**, 3934–3951.
287 L. Li, P. A. Salvador and G. S. Rohrer, *Nanoscale*, 2013, **6**, 24–42.
288 X. He, T. Kai and P. Ding, *Environ. Chem. Lett.*, 2021, **196**(19), 4563–4601.
289 L. Ye, J. Liu, L. Tian, T. Peng and L. Zan, *Appl. Catal., B*, 2013, **134–135**, 60–65.
290 Z. He, Y. Shi, C. Gao, L. Wen, J. Chen and S. Song, *J. Phys. Chem. C*, 2014, **118**, 389–398.
291 J. Cao, X. Li, H. Lin, S. Chen and X. Fu, *J. Hazard. Mater.*, 2012, **239–240**, 316–324.
292 J. Lin, J. Shen, R. Wang, J. Cui, W. Zhou, P. Hu, D. Liu, H. Liu, J. Wang, R. I. Boughton and Y. Yue, *J. Mater. Chem.*, 2011, **21**, 5106–5113.
293 C. Chen, W. Cai, M. Long, B. Zhou, Y. Wu, D. Wu and Y. Feng, *ACS Nano*, 2010, **4**, 6425–6432.
294 Z. Zhang, C. Shao, X. Li, C. Wang, M. Zhang and Y. Liu, *ACS Appl. Mater. Interfaces*, 2010, **2**, 2915–2923.
295 G. Dai, J. Yu and G. Liu, *J. Phys. Chem. C*, 2011, **115**, 7339–7346.
296 C. J. Chen, C. H. Liao, K. C. Hsu, Y. T. Wu and J. C. S. Wu, *Catal. Commun.*, 2011, **12**, 1307–1310.
297 L. Zhao, T. Cui, Y. Li, B. Wang, J. Han, L. Han and Z. Liu, *RSC Adv.*, 2015, **5**, 64495–64502.
298 T. B. Nguyen and R. A. Doong, *RSC Adv.*, 2017, **7**, 50006–50016.
299 C. Wang, C. Shao, X. Zhang and Y. Liu, *Inorg. Chem.*, 2009, **48**, 7261–7268.
300 M. Lei, N. Wang, L. Zhu, Q. Zhou, G. Nie and H. Tang, *Appl. Catal., B*, 2016, **182**, 414–423.
301 Y. Shi, H. Li, L. Wang, W. Shen and H. Chen, *ACS Appl. Mater. Interfaces*, 2012, **4**, 4800–4806.
302 K. H. Reddy, S. Martha and K. M. Parida, *Inorg. Chem.*, 2013, **52**, 6390–6401.
303 X. Yuan, L. Jiang, J. Liang, Y. Pan, J. Zhang, H. Wang, L. Leng, Z. Wu, R. Guan and G. Zeng, *Chem. Eng. J.*, 2019, **356**, 371–381.
304 Y. Zhang, W. Li, Z. Sun, Q. Zhang, L. Wang and Z. Chen, *J. Alloys Compd.*, 2017, **713**, 78–86.
305 J. Gao, Y. Gao, Z. Sui, Z. Dong, S. Wang and D. Zou, *J. Alloys Compd.*, 2018, **732**, 43–51.
306 L. Cao, D. Ma, Z. Zhou, C. Xu, C. Cao, P. Zhao and Q. Huang, *Chem. Eng. J.*, 2019, **368**, 212–222.
307 A. J. Bard, *J. Photochem.*, 1979, **10**, 59–75.

 © 2025 The Author(s). Published by the Royal Society of Chemistry

Open Access Article. Published on 02 September 2025. Downloaded on 11/10/2025 5:56:01 AM.
This article is licensed under a Creative Commons Attribution-NonCommercial 3.0 Unported Licence.

308 B. Zhu, P. Xia, Y. Li, W. Ho and J. Yu, *Appl. Surf. Sci.*, 2017, **391**, 175–183.
309 K. Maeda, *ACS Catal.*, 2013, **3**, 1486–1503.
310 H. Tada, T. Mitsui, T. Kiyonaga, T. Akita and K. Tanaka, *Nat. Mater.*, 2006, **510**(5), 782–786.
311 W. Zhang, A. R. Mohamed and W. J. Ong, *Angew. Chem., Int. Ed.*, 2020, **59**, 22894–22915.
312 X. Li, X. Yan, X. Lu, S. Zuo, Z. Li, C. Yao and C. Ni, *J. Catal.*, 2018, **357**, 59–68.
313 X. Wu, J. Zhao, L. Wang, M. Han, M. Zhang, H. Wang, H. Huang, Y. Liu and Z. Kang, *Appl. Catal., B*, 2017, **206**, 501–509.
314 J. Zhang, M. Yan, X. Yuan, M. Si, L. Jiang, Z. Wu, H. Wang and G. Zeng, *J. Colloid Interface Sci.*, 2018, **529**, 11–22.
315 Z. Guan, X. Li, Y. Wu, Z. Chen, X. Huang, D. Wang, Q. Yang, J. Liu, S. Tian, X. Chen and H. Zhao, *Chem. Eng. J.*, 2021, **410**, 128283.
316 D. Ma, J. Wu, M. Gao, Y. Xin, T. Ma and Y. Sun, *Chem. Eng. J.*, 2016, **290**, 136–146.
317 J. Li, Q. Wang, Y. Zhang, Y. Liu, X. Liu and Z. Jiao, *Solid State Sci.*, 2020, **104**, 106200.
318 L. Jiang, X. Yuan, G. Zeng, J. Liang, X. Chen, H. Yu, H. Wang, Z. Wu, J. Zhang and T. Xiong, *Appl. Catal., B*, 2018, **227**, 376–385.
319 J. M. Li, H. Y. Cheng, Y. H. Chiu and Y. J. Hsu, *Nanoscale*, 2016, **8**, 15720–15729.
320 R. Wang, T. Xie, T. Zhang, T. Pu, Y. Bu and J. P. Ao, *J. Mater. Chem. A*, 2018, **6**, 12956–12961.
321 Y. Jia, H. Ma and C. Liu, *Appl. Surf. Sci.*, 2019, **463**, 854–862.
322 Q. Li, F. Wang, Y. Hua, Y. Luo, X. Liu, G. Duan and X. Yang, *J. Colloid Interface Sci.*, 2017, **506**, 207–216.
323 D. Wang, H. Shen, L. Guo, F. Fu and Y. Liang, *New J. Chem.*, 2016, **40**, 8614–8624.
324 J. Yu, S. Wang, J. Low and W. Xiao, *Phys. Chem. Chem. Phys.*, 2013, **15**, 16883–16890.
325 P. Zhou, J. Yu and M. Jaroniec, *Adv. Mater.*, 2014, **26**, 4920–4935.
326 H. Li, W. Tu, Y. Zhou and Z. Zou, *Adv. Sci.*, 2016, **3**, 1500389.
327 J. Low, C. Jiang, B. Cheng, S. Wageh, A. A. Al-Ghamdi and J. Yu, *Small Methods*, 2017, **1**, 1700080.
328 S. Bai, J. Jiang, Q. Zhang and Y. Xiong, *Chem. Soc. Rev.*, 2015, **44**, 2893–2939.
329 J. Liu, B. Cheng and J. Yu, *Phys. Chem. Chem. Phys.*, 2016, **18**, 31175–31183.
330 Q. Xu, L. Zhang, J. Yu, S. Wageh, A. A. Al-Ghamdi and M. Jaroniec, *Mater. Today*, 2018, **21**, 1042–1063.
331 W. Liu, D. Liu, K. Wang, X. Yang, S. Hu and L. Hu, *Nanoscale Res. Lett.*, 2019, **14**, 1–8.
332 Y. A. Shaban, M. A. El Sayed, A. A. El Maradny, R. K. Al Farawati, M. I. Al Zobidi and S. U. M. Khan, *Appl. Surf. Sci.*, 2016, **365**, 108–113.
333 B. Chen, Y. Meng, J. Sha, C. Zhong, W. Hu and N. Zhao, *Nanoscale*, 2017, **10**, 34–68.
334 J. Luo, L. Ma, T. He, C. F. Ng, S. Wang, H. Sun and H. J. Fan, *J. Phys. Chem. C*, 2012, **116**, 11956–11963.
335 C. Wang, G. Wang, X. Zhang, X. Dong, C. Ma, X. Zhang, H. Ma and M. Xue, *RSC Adv.*, 2018, **8**, 18419–18426.
336 P. Xia, B. Zhu, B. Cheng, J. Yu and J. Xu, *ACS Sustain. Chem. Eng.*, 2018, **6**, 965–973.
337 J. Luo, R. Li, Y. Chen, X. Zhou, X. Ning, L. Zhan, L. Ma, X. Xu, L. Xu and L. Zhang, *Sep. Purif. Technol.*, 2019, **210**, 417–430.
338 L. Zhu, H. Li, P. Xia, Z. Liu and D. Xiong, *ACS Appl. Mater. Interfaces*, 2018, **10**, 39679–39687.
339 R. Ji, C. Ma, W. Ma, Y. Liu, Z. Zhu and Y. Yan, *New J. Chem.*, 2019, **43**, 11876–11886.
340 X. Li, H. Sun, Y. Xie, Y. Liang, X. Gong, P. Qin, L. Jiang, J. Guo, C. Liu and Z. Wu, *Coord. Chem. Rev.*, 2022, **467**, 214596.
341 J. Zhang, Y. Wu, M. Xing, S. A. K. Leghari and S. Sajjad, *Energy Environ. Sci.*, 2010, **3**, 715–726.
342 B. Srikanth, R. Goutham, R. Badri Narayan, A. Ramprasath, K. P. Gopinath and A. R. Sankaranarayanan, *J. Environ. Manage.*, 2017, **200**, 60–78.
343 H. S. Kushwaha, G. Parmesh, R. Vaish and K. B. R. Varma, *J. Non-Cryst. Solids*, 2015, **408**, 13–17.
344 A. Manassero, M. L. Satuf and O. M. Alfano, *Environ. Sci. Pollut. Res.*, 2017, **24**, 6031–6039.
345 S. Chowdhury and R. Balasubramanian, *Appl. Catal., B*, 2014, **160–161**, 307–324.
346 Y. Guan, H. Qian, J. Q. Guo, S. Yang, X. Wang, S. Wang and Y. Fu, *Appl. Clay Sci.*, 2015, **114**, 124–132.
347 M. Huang, C. Xu, Z. Wu, Y. Huang, J. Lin and J. Wu, *Dyes Pigm.*, 2008, **77**, 327–334.
348 S. Singh, H. Mahalingam and P. K. Singh, *Appl. Catal., A*, 2013, **462–463**, 178–195.
349 J. Shang, M. Chai and Y. Zhu, *J. Solid State Chem.*, 2003, **174**, 104–110.
350 B. Haspulat, A. Gülce and H. Gülce, *J. Hazard. Mater.*, 2013, **260**, 518–526.
351 Z. M. Shaykhi and A. A. L. Zinatizadeh, *J. Taiwan Inst. Chem. Eng.*, 2014, **45**, 1717–1726.
352 J. Zeng, S. Liu, J. Cai and L. Zhang, *J. Phys. Chem. C*, 2010, **114**, 7806–7811.
353 M. Kovacic, S. Salaeh, H. Kusic, A. Suligoj, M. Kete, M. Fanetti, U. L. Stangar, D. D. Dionysiou and A. L. Bozic, *Environ. Sci. Pollut. Res.*, 2016, **23**, 17982–17994.
354 S. V. Mohite, V. V. Ganbavle, V. V. Patil and K. Y. Rajpure, *Mater. Chem. Phys.*, 2016, **183**, 439–446.
355 R. Nadarajan, W. A. Wan Abu Bakar, R. Ali and R. Ismail, *Arabian J. Chem.*, 2018, **11**, 34–47.
356 Q. Zhao, X. Zhao and J. Cao, *Adv. Nanomater. Pollut. Sens. Environ. Catal.*, 2020, 249–305.
357 L. Qiang, M. Chen, L. Zhu, W. Wu and Q. Wang, *Environ. Sci. Technol.*, 2016, **50**, 11627–11636.
358 S. O. Akinnawo, *Desalin. Water Treat.*, 2024, **319**, 100437.
359 C. S. Cao, J. Wang, L. Yang, J. Wang, Y. Zhang and L. Zhu, *Sci. Total Environ.*, 2024, **946**, 174137.
360 S. Verma, B. Mezgebe, C. A. Hejase, E. Sahle-Demessie and M. N. Nadagouda, *Next Mater.*, 2024, **2**, 100077.
361 M. J. Chen, S. L. Lo, Y. C. Lee and C. C. Huang, *J. Hazard. Mater.*, 2015, **288**, 168–175.
362 C. Xu, P. Qiu, H. Chen and F. Jiang, *J. Taiwan Inst. Chem. Eng.*, 2017, **80**, 761–768.

Open Access Article. Published on 02 September 2025. Downloaded on 11/10/2025 5:56:01 AM.
This article is licensed under a Creative Commons Attribution-NonCommercial 3.0 Unported Licence.

363 Z. Li, P. Zhang, J. Li, T. Shao and L. Jin, *J. Photochem. Photobiol., A*, 2013, **271**, 111–116.
364 S. C. Panchangam, A. Y. C. Lin, K. L. Shaik and C. F. Lin, *Chemosphere*, 2009, **77**, 242–248.
365 X. Li, P. Zhang, L. Jin, T. Shao, Z. Li and J. Cao, *Environ. Sci. Technol.*, 2012, **46**, 5528–5534.
366 J. Wang, Z. Luo, Y. Song, X. Zheng, L. Qu, J. Qian, Y. Wu, X. Wu and Z. Wu, *Chemosphere*, 2019, **221**, 554–562.
367 D. Xu, W. Shi, C. Song, M. Chen, S. Yang, W. Fan and B. Chen, *Appl. Catal., B*, 2016, **191**, 228–234.
368 J. C. Wang, J. Ren, H. C. Yao, L. Zhang, J. S. Wang, S. Q. Zang, L. F. Han and Z. J. Li, *J. Hazard. Mater.*, 2016, **311**, 11–19.
369 J. Liu, R. Li, Y. Wang, Y. Wang, X. Zhang and C. Fan, *J. Alloys Compd.*, 2017, **693**, 543–549.
370 Q. Zhang, Y. Huang, S. Peng, Y. Zhang, Z. Shen, J. ji Cao, W. Ho, S. C. Lee and D. Y. H. Pui, *Appl. Catal., B*, 2017, **204**, 346–357.
371 K. Brindhadevi, T. P. Kim, S. A. Alharbi, M. D. Ramesh, J. Lee and D. Bharathi, *Environ. Res.*, 2024, **252**, 118454.
372 I. H. Cho, *Toxicol. Environ. Chem.*, 2011, **93**, 925–940.
373 G. Eker and M. Hatipoglu, *Environ. Technol.*, 2019, **40**, 3793–3803.
374 M. Li, Z. Yu, Q. Liu, L. Sun and W. Huang, *Chem. Eng. J.*, 2016, **286**, 232–238.
375 M. J. Chen, S. L. Lo, Y. C. Lee and C. C. Huang, *J. Hazard. Mater.*, 2015, **288**, 168–175.
376 M. J. Rivero, P. Ribao, B. Gomez-Ruiz, A. Urtiaga and I. Ortiz, *Sep. Purif. Technol.*, 2020, **240**, 116637.
377 X. Yao, J. Zuo, Y. J. Wang, N. N. Song, H. H. Li and K. Qiu, *Front. Chem.*, 2021, **9**, 690520.
378 B. Zhao and P. Zhang, *Catal. Commun.*, 2009, **10**, 1184–1187.
379 T. Shao, P. Zhang, Z. Li and L. Jin, *Chin. J. Catal.*, 2013, **34**, 1551–1559.
380 X. Tan, G. Chen, D. Xing, W. Ding, H. Liu, T. Li and Y. Huang, *Environ. Sci.:Nano*, 2020, **7**, 2229–2239.
381 Z. Li, P. Zhang, T. Shao, J. Wang, L. Jin and X. Li, *J. Hazard. Mater.*, 2013, **260**, 40–46.
382 F. Jiang, H. Zhao, H. Chen, C. Xu and J. Chen, *RSC Adv.*, 2016, **6**, 72015–72021.
383 A. U. R. Bacha, I. Nabi, Z. Fu, K. Li, H. Cheng and L. Zhang, *Chin. Chem. Lett.*, 2019, **30**, 2225–2230.
384 B. Wang, C. Yang, J. Zhong, J. Li, Y. Zhu and J. Miao, *Solid State Sci.*, 2023, **138**, 107155.
385 D. Wu, X. Li, Y. Tang, P. Lu, W. Chen, X. Xu and L. Li, *Chemosphere*, 2017, **180**, 247–252.
386 N. Vela, M. Martínez-Menchón, G. Navarro, G. Pérez-Lucas and S. Navarro, *J. Photochem. Photobiol., A*, 2012, **232**, 32–40.
387 C. B. Ong, A. W. Mohammad, L. Y. Ng, E. Mahmoudi, S. Azizkhani and N. H. Hayati Hairom, *Process Saf. Environ. Prot.*, 2017, **112**, 298–307.
388 K. Rachna, M. Rani and U. Shanker, *J. Photochem. Photobiol., A*, 2019, **381**, 111861.
389 A. Al-Hunaiti, A. M. Ghazzy and N. T. Mahmoud, *Chem. Eng. J. Adv.*, 2024, **19**, 100631.
390 M. A. Al-Ghouti, M. A. M. Khraisheh, S. J. Allen and M. N. Ahmad, *J. Environ. Manage.*, 2003, **69**, 229–238.
391 A. Alinsafi, M. Khemis, M. N. Pons, J. P. Leclerc, A. Yaacoubi, A. Benhammou and A. Nejmeddine, *Chem. Eng. Process.*, 2005, **44**, 461–470.
392 M. A. D. Flores Alarcón, C. Revilla Pacheco, K. Garcia Bustos, K. Tejada Meza, F. Terán-Hilares, D. A. Pacheco Tanaka, G. J. Colina Andrade and R. Terán-Hilares, *Water*, 2022, **14**, 4104.
393 N. A. A. Suhaimi, C. P. Y. Kong, N. N. M. Shahri, M. Nur, J. Hobley and A. Usman, *Catalysts*, 2022, **12**, 1254.
394 M. A. Rather and M. Mandal, *Microb. Pathog.*, 2023, **185**, 106433.
395 A. P. Torane, A. B. Ubale, K. G. Kanade and P. K. Pagare, *Mater. Today: Proc.*, 2021, **43**, 2738–2741.
396 S. Faryad, U. Azhar, M. B. Tahir, W. Ali, M. Arif and M. Sagir, *Chemosphere*, 2023, **320**, 138002.
397 S. Selvaraj, S. Patrick, G. A. Vangari, M. K. Mohan, S. Ponnusamy and C. Muthamizhchelvan, *Ceram. Int.*, 2022, **48**, 29049–29058.
398 M. Saeed, A. U. Haq, M. Muneer, A. Ahmad, T. H. Bokhari and Q. Sadiq, *Phys. Scr.*, 2021, **96**, 125707.
399 H. C. Sathisha, S. Anitha, G. Krishnamurthy, M. Pari, T. L. Soundarya and G. Nagaraju, *Chem. Data Collect.*, 2023, **48**, 101081.
400 S. S. Hossain, M. Tarek, T. D. Munusamy, K. M. Rezaul Karim, S. M. Roopan, S. M. Sarkar, C. K. Cheng and M. M. Rahman Khan, *Environ. Res.*, 2020, **188**, 109803.
401 T. Rajaramanan, S. Shanmugaratnam, V. Gurunanthanan, S. Yohi, D. Velauthapillai, P. Ravirajan and M. Senthilnanthanan, *Catalysts*, 2021, **11**, 690.
402 S. D. Sharma, D. Singh, K. K. Saini, C. Kant, V. Sharma, S. C. Jain and C. P. Sharma, *Appl. Catal., A*, 2006, **314**, 40–46.
403 D. I. Anwar and D. Mulyadi, *Procedia Chem.*, 2015, **17**, 49–54.
404 A. Arshad, J. Iqbal, M. Siddiq, M. U. Ali, A. Ali, H. Shabbir, U. Bin Nazeer and M. S. Saleem, *Ceram. Int.*, 2017, **43**, 10654–10660.
405 M. Wang, J. Huang, Z. Tong, W. Li and J. Chen, *J. Alloys Compd.*, 2013, **568**, 26–35.
406 K. Mageshwari, D. Nataraj, T. Pal, R. Sathyamoorthy and J. Park, *J. Alloys Compd.*, 2015, **625**, 362–370.
407 M. M. Mohamed, M. A. Ghanem, M. Khairy, E. Naguib and N. H. Alotaibi, *Appl. Surf. Sci.*, 2019, **487**, 539–549.
408 Z. Durmus, B. Z. Kurt and A. Durmus, *ChemistrySelect*, 2019, **4**, 271–278.
409 X. Ren, H. Yang, S. Gen, J. Zhou, T. Yang, X. Zhang, Z. Cheng and S. Sun, *Nanoscale*, 2015, **8**, 752–756.
410 S. Guo, G. Zhang, Y. Guo and J. C. Yu, *Carbon*, 2013, **60**, 437–444.
411 M. A. Basith, R. Ahsan, I. Zarin and M. A. Jalil, *Sci. Rep.*, 2018, **8**, 1–11.
412 G. Balakrishnan, R. Velavan, K. Mujasam Batoo and E. H. Raslan, *Results Phys.*, 2020, **16**, 103013.
413 M. Ikram, T. Inayat, A. Haider, A. Ul-Hamid, J. Haider, W. Nabgan, A. Saeed, A. Shahbaz, S. Hayat, K. Ul-Ain and A. R. Butt, *Nanoscale Res. Lett.*, 2021, **16**, 1–11.

 © 2025 The Author(s). Published by the Royal Society of Chemistry

Open Access Article. Published on 02 September 2025. Downloaded on 11/10/2025 5:56:01 AM.
This article is licensed under a Creative Commons Attribution-NonCommercial 3.0 Unported Licence.

414 A. B. Vennela, D. Mangalaraj, N. Muthukumarasamy, S. Agilan and K. V. Hemalatha, *Int. J. Electrochem. Sci.*, 2019, **14**, 3535–3552.
415 G. Hitkari, S. Sandhya, P. Gajanan, M. K. Shrivash and K. Deepak, *J. Mater. Sci. Eng.*, 2018, **7**, 2169–2222.
416 J. Tao, M. Zhang, X. Gao, H. Zhao, Z. Ren, D. Li, J. Li, R. Zhang, Y. Liu and Y. Zhai, *Mater. Chem. Phys.*, 2020, **240**, 122185.
417 L. Gnanasekaran, R. Hemamalini, R. Saravanan, K. Ravichandran, F. Gracia, S. Agarwal and V. K. Gupta, *J. Photochem. Photobiol., B*, 2017, **173**, 43–49.
418 R. Abazari, A. R. Mahjoub, L. A. Saghatforoush and S. Sanati, *Mater. Lett.*, 2014, **133**, 208–211.
419 K. Azoulay, I. Bencheikh and J. Mabrouki, *Stud. Syst. Decis. Control*, 2024, **527**, 79–94.
420 S. Kumar Srivastava, *RSC Appl Interfaces*, 2024, **1**, 340–429.
421 K. Samal, S. Mahapatra and M. Hibzur Ali, *Energy Nexus*, 2022, **6**, 100076.
422 V. Vinayagam, S. Murugan, R. Kumaresan, M. Narayanan, M. Sillanpää, D. Viet N Vo, O. S. Kushwaha, P. Jenis, P. Potdar and S. Gadiya, *Chemosphere*, 2022, **300**, 134597.
423 T. Velempini, E. Prabakaran and K. Pillay, *Mater. Today Chem.*, 2021, **19**, 100380.
424 S. Sood, S. K. Mehta, A. S. K. Sinha and S. K. Kansal, *Chem. Eng. J.*, 2016, **290**, 45–52.
425 M. Rostami, R. M. Zamani, K. M. Aghajanzadeh and H. Danafar, *J. Pharm. Invest.*, 2018, **48**, 657–664.
426 Y. M. Hunge, A. A. Yadav, S. W. Kang, S. Jun Lim and H. Kim, *J. Photochem. Photobiol., A*, 2023, **434**, 114250.
427 L. Rimoldi, D. Meroni, G. Cappelletti and S. Ardizzone, *Catal. Today*, 2017, **281**, 38–44.
428 S. Pang, J. guo Huang, Y. Su, B. Geng, S. yuan Lei, Y. ting Huang, C. Lyu and X. juan Liu, *Photochem. Photobiol.*, 2016, **92**, 651–657.
429 W. Wang, J. Fang, S. Shao, M. Lai and C. Lu, *Appl. Catal., B*, 2017, **217**, 57–64.
430 G. Zhang, X. Zhang, Y. Wu, W. Shi and W. Guan, *Micro Nano Lett.*, 2013, **8**, 177–180.
431 A. Ren, C. Liu, Y. Hong, W. Shi, S. Lin and P. Li, *Chem. Eng. J.*, 2014, **258**, 301–308.
432 X. Yu, J. Zhang, J. Zhang, J. Niu, J. Zhao, Y. Wei and B. Yao, *Chem. Eng. J.*, 2019, **374**, 316–327.
433 S. Wang, J. Liu, I. Albaijan, A. Shawabkeh, H. Lin, I. Ahmad, S. O. Rab and M. Y. Alshahrani, *J. Ind. Eng. Chem.*, 2024, **135**, 213–231.
434 M. Rani, S. Choudhary, G. Shukla and U. Shanker, *Environ. Nanotechnol., Monit. Manage.*, 2024, **21**, 100935.
435 S. H. Cao, J. R. Qu, Y. Q. Zhao, Y. T. Sun, W. T. Gao, B. Han and Y. Lu, *Rare Met.*, 2024, **43**, 3134–3145.
436 O. Ali Al Hattali, F. Al Marzouqi, S. Al Mamari, A. T. Kuvarega and R. Selvaraj, *Inorg. Chem. Commun.*, 2022, **146**, 110071.